C. Cameron
6215—

TECHNICAL REPORT BRL-TR-3215

BRL

OPTICAL STUDIES OF THE FLOW START-UP PROCESSES IN FOUR CONVERGENT-DIVERGENT NOZZLES

KLAUS O. OPALKA

MARCH 1991

U.S. ARMY LABORATORY COMMAND

BALLISTIC RESEARCH LABORATORY
ABERDEEN PROVING GROUND, MARYLAND

NOTICES

Destroy this report when it is no longer needed. DO NOT return it to the originator.

Additional copies of this report may be obtained from the National Technical Information Service, U.S. Department of Commerce, 5285 Port Royal Road, Springfield, VA 22161.

The findings of this report are not to be construed as an official Department of the Army position, unless so designated by other authorized documents.

The use of trade names or manufacturers' names in this report does not constitute indorsement of any commercial product.

REPORT DOCUMENT PAGE

Form Approved
OMB No. 0704-0188

1. AGENCY USE ONLY *(Leave blank)*	2. REPORT DATE	3. REPORT TYPE AND DATES COVERED
	March 1991	FINAL, June 89 - Sep 90

4. TITLE AND SUBTITLE
Optical Studies of the Flow Start-Up Processes in Four Convergent-Divergent Nozzles

5. FUNDING NUMBERS
PR: 1L162120AH25

6. AUTHOR(S)
Klaus O. Opalka

7. PERFORMING ORGANIZATION NAME(S) AND ADDRESS(ES)
Director
U.S. Army Ballistic Research Laboratory
ATTN: SLCBR-TB-B
Aberdeen Proving Ground, MD 21005-5066

8. PERFORMING ORGANIZATION REPORT NUMBER

9. SPONSORING/MONITORING AGENCY NAMES(S) AND ADDRESS(ES)
U.S. Army Ballistic Research Laboratory
ATTN: SLCBR-DD-T
Aberdeen Proving Ground, MD 21005-5066

10.SPONSORING/MONITORING AGENCY REPORT NUMBER
BRL-TR-3215

11. SUPPLEMENTARY NOTES
This work was performed under the auspices of the U.S. Army Harry Diamond Laboratories, ATTN: SLCHD-NW-P, 2800 Powder Mill Road, Adelphi, MD 20783-1197

12a. DISTRIBUTION/AVAILABILITY STATEMENT
Approved for public release; distribution is unlimited.

12b. DISTRIBUTION CODE

13. ABSTRACT *(Maximum 200 words)*

In the context of design studies for the U.S. Large Blast/Thermal Simulator (LB/TS), the U.S. Army Ballistic Research Laboratory (BRL) has sponsored optical studies of the flow start-up in convergent-divergent nozzles which have the flow-initiating diaphragm located in the nozzle throat. The experiments were performed in the 200-mm shock tube at the Ernst-Mach-Institute in Freiburg (Breisgau), West-Germany. The scope of the studies included divergent nozzles with half-cone angles of 6°, 16°, 45° and 90° tested at seven diaphragm pressure ratios ranging from four to 188 and resulting in shock strengths ranging from 1.4 to 4.4. The results were summarized in graphs of significant parameters, e.g., shock formation time, flow start-up period, flow expansion angle and shock strength versus the driver pressure ratio and further compared with numerical results obtained with the BRL-Q1D hydrocode. The numerical-experimental comparison shows qualitative agreement. The flow phenomena are generally reproduced by the computations as long as they are not strongly dependent on viscous effects. The study shows that a pressure loss of 10 percent is connected to the presence of a large area discontinuity at the exit plane of the nozzle throat when no divergent nozzle is attached. The results suggest that a 45° divergent nozzle may present an acceptable compromise for minimizing these pressure losses by reducing the associated area discontinuities.

14. SUBJECT TERMS			15. NUMBER OF PAGES
Experimental Data	Gas Dynamics	Shock Tubes	111
Schlieren Photography	Unsteady Flow	Nozzle Gas Flow	16. PRICE CODE
Large Blast Simulator	Convergent Divergent Nozzles	Nozzle Closures	
	Computational Fluid Dynamics	Shock Waves	

17. SECURITY CLASSIFICATION OF REPORT	18. SECURITY CLASSIFICATION OF THIS PAGE	19. SECURITY CLASSIFICATION OF ABSTRACT	20. LIMITATION OF ABSTRACT
UNCLASSIFIED	UNCLASSIFIED	UNCLASSIFIED	UL

NSN 7540-01-280-5500
Standard Form 298 (Rev. 2-89)
Prescribed by ANSI Std. 239-18 298-102

(intentionally left blank)

TABLE OF CONTENTS

(intentionally left blank)

LIST OF ILLUSTRATIONS

LIST OF ILLUSTRATIONS (continued)

Acknowledgement

The Author wishes to thank Dr. Heinz Reichenbach of the Ernst-Mach-Institut, Freiburg im Breisgau, Federal Republic of Germany for his guidance and assistance in providing the experimental data. Thanks are extended to Dipl.-Ing. Schaetzle and Mr. Gehri for executing the test program in an expert manner and to Mrs. Geppert for her careful photographic work. The experiments were performed at the Ernst-Mach-Institut under research contract No. DAJR 45-89-C-0019.

(intentionally left blank)

1. INTRODUCTION

It is known that the gas behind a shock travelling down a shock tunnel can be expanded to high flow Mach numbers by passing it through convergent-divergent (DeLaval) nozzles. Such nozzles have been extensively investigated, both in theory and experiment, and a summary of these efforts has been presented by Amann (1968). However, in all of these studies the diaphragm which separates the high-pressure region from the low-pressure region was located upstream of the nozzle under investigation so that a well-formed shock entered the nozzle from the upstream side. No efforts were undertaken to study the shock formation in nozzles immediately after flow initialization.

Large Blast/Thermal Simulators (LB/TS) are specialized shock tunnels for simulating blast and thermal effects associated with decaying blast waves such as are generated by nuclear explosions. LB/TS's are postulated to employ convergent-divergent nozzles at the driver exit to retard the outflow of the high-pressure driver gas thus generating long flow durations (Cadet and Monzac 1981; Mark, Opalka, et. al. 1983; Pearson, Opalka and Hisley 1985; Opalka and Pearson 1988, 1989). The nozzle design for an LB/TS differs from the nozzle design used in the previously mentioned studies in that it has the flow-initiating diaphragm mounted in the throat of the nozzle itself. When the diaphragm is ruptured, a shock forms travelling downstream into the divergent section, while a rarefaction fan travels upstream into the convergent section. No previous experimental research is known for this problem.

The U. S. Army Ballistic Research Laboratory (BRL), in cooperation with the Ernst-Mach Institut (EMI), Freiburg im Breisgau, Germany, therefore, initiated an optical study of the flow start-up process in four convergent-divergent nozzles which had the diaphragm separating the high-pressure and low-pressure sections of the shock tube mounted in the throat of the nozzles. Under the auspices of a bi-lateral data exchange agreement between the governments of the U. S. A. and the Federal Republic of Germany (FRG), the experiments were performed in the 200 mm shock tube at EMI. The diaphragm was located at the upstream edge of the viewing window of high-quality optical glass through which shadow and schlieren photographs could be taken. The optical measurements were supplemented by measurements of the static pressure at three locations downstream from the nozzles.

The objectives of this investigation were to (a) obtain optical records of the shock formation in the convergent-divergent nozzle immediately after rupturing the diaphragm, (b) study the shock formation and flow start-up processes in the divergent nozzles, (c) determine the influence of the cone angle and length of a divergent nozzle on the pressure signature in the expansion region behind the nozzle and (d) facilitate comparisons with one- and two-dimensional hydrocode computations. The test setup and the results of this experimental study are presented in this report and the significant findings are discussed.

2. BACKGROUND

The U.S. Army has proposed the construction of a test facility for simulating ideal blast waves and large enough to test full-sized military equipment in order to meet its growing need for blast and thermal survivability testing. The BRL was assigned the lead role in the research and development phase of this project. Subsequently, the BRL developed a concept of such a facility, referred to as LB/TS, over the past nine years. In 1988, the Defense Nuclear Agency (DNA) assumed responsibility for the construction of such a facility to be located on the White Sands Missile Range (WSMR), New Mexico (Figure 1). The proposed U.S. LB/TS is suitable to simulate both thermal and blast effects of nuclear explosions over a wide variety of shock overpressures and weapon yields without generating nuclear radiation effects (Figure 2). The LB/TS will be used to conduct blast and thermal survivability testing on full-scale military equipment, like trucks and helicopters, and to perform research into nuclear blast phenomenology.

2.1 LB/TS Concept. An LB/TS is basically a shock tunnel whose cross-sectional area varies along its length. Constant area (i.e., straight) shock tubes do not produce the flow durations which are observed in decaying blast waves. To obtain long flow durations comparable to those of decaying blast waves, the outflow of the driver gas has to be retarded. This is effected by converging the flow area at the exit of the driver, so that the driver takes the shape of a bottle. Furthermore, a single driver is technically impractical because of the size of the facility and the required supply pressures in the driver. A number of smaller drivers has to be employed to accomodate the necessary initial test conditions. The BRL LB/TS concept is described in detail by Pearson (1987) and Opalka (1987, 1989) and illustrated in Figure 3.

Blast waves will be simulated by releasing compressed gas from several high-pressure steel driver tubes into a large expansion tunnel constructed of prestressed concrete. The gas exits the drivers through convergent nozzles. Fast-acting valves were to be mounted in the throats of these nozzles; but DNA abandoned the use of valves for flow initiation in favor of the proven diaphragm technique. The divergent nozzles were eliminated for cost efficiency. The expansion tunnel has a semicircular cross section with a 10m radius. This size is deemed necessary to avoid blocking of the flow about the largest target. The test section for the targets is centered at about seven hydraulic diameters (14.94m) downstream from the exit of the driver nozzles in the expansion tunnel. The thermal simulation will be effected through aluminum/oxygen combustion near the target. An active reflection-wave eliminator (RWE) at the open end of the expansion tunnel prevents reflected shocks or rarefaction waves from travelling back into the test section and disfiguring the shape of the simulated blast wave.

2.2 LB/TS Design Studies. The BRL-Q1D code (Opalka and Mark 1986) was used to perform computational studies for determining the design parameters of the projected facility. Parametric studies (Opalka 1987, 1989) were initiated to answer questions about the necessary size and the expected performance of such a facility

for simulating the required range of blast waves. The scope of the computational studies encompassed pressure ratios from 4 to 200 across the diaphragm for unheated driver gas with stagnation temperature T_4 = 288.15 K and ratio of specific heats γ = 1.4 in association with the operating envelope for the planned U.S. LB/TS (Figure 2). Standard atmospheric conditions were assumed as ambient in the expansion tunnel for all computational simulations. Table I presents the test conditions which were selected for the parametric BRL-Q1D computations. The shock strength, the positive-phase duration, and the static and dynamic impulses of the simulated blast wave in the test section of the LB/TS were defined from the initial test conditions, i.e., the driver volume, V_4, the driver pressure ratio, P_4/P_1, and the driver temperature ratio, T_4/T_1, where subscript 1 refers to driven (i.e., ambient) and subscript 4 to driver conditions. For the purpose of this study, the initial throat shock overpressure, p_{Ts}, was determined by iteratively solving the basic shock tube equation, $P_4/P_1 = f(P_{T2}/P_1)$, where subscript 2 identifies conditions behind the incident shock.

TABLE I. LB/TS INITIAL TEST CONDITIONS
P_1 = 101.325 kPa; T_1 = 288.15 K

TEST SECTION								
p_s, psi	2.0	5.0	10.0	15.0	20.0	25.0	30.0	35.0
p_s, kPa	13.79	34.47	68.95	103.4	137.9	172.4	206.8	241.3
DRIVER								
P_4/P_1	4	14	38	55	80	110	145	188
P_4, MPa	0.4053	1.419	3.850	5.573	8.106	11.145	14.692	19.050
THROAT								
P_{T2}/P_1	1.929	3.256	4.689	5.288	5.974	6.575	7.120	7.652
p_{Ts}, kPa	94.11	228.6	373.8	434.5	504.4	565.0	620.1	674.0

Initially, the U.S. design studies were based on the Large Blast Simulator (LBS) at the Centre d'Etudes de Gramat (CEG), France (Gratias and Monzac 1981). However, it soon became clear that a much larger facility was needed in order to accommodate the full range of anticipated targets (Ethridge, et. al. 1984). Also, a broader range of shock overpressures and weapon yields was required to cover the test conditions specified in the operating envelope (Figure 2). The results of our computational studies with the BRL-Q1D code showed that the full-scale blast/thermal simulation facility must employ driver gas heating, an active RWE, and should use computer-controlled throat valves to optimize control and operation of the facility. The divergent nozzles were eliminated from the design; however, some questions remain about the usefulness of such divergent nozzles.

Experimental efforts were initiated at the same time, but test results became available only much later because the construction of the model facility required a long time. To date, small-scale experiments with heated driver gas, as well as an active RWE model, have been completed and the results have been used to validate

the computational predictions (Coulter 1987; Gion 1989; Schraml and Pearson 1990). A throat-valve model has been built and is awaiting testing for the validation of the design concept and the computational predictions. Also, a 1/6-scale test bed using a double diaphragm and an active RWE is in the construction stage and, when built, will be used for validating the design concepts, for research, and for vulnerability testing of small items of military equipment.

2.3 Nozzle Flow Phenomena. The drivers of the proposed U. S. LB/TS, as well as of the CEG-LBS, have the diaphragm which separates the high-pressure region from the low-pressure region of the shock tunnel mounted in the throat of a convergent nozzle. The CEG-LBS uses divergent nozzles to control the expansion of the flow into the expansion tunnel. When the diaphragm is ruptured, a shock travels downstream into the divergent section, while a rarefaction fan travels upstream into the convergent section. The time from the rupturing of the diaphragm to the establishment of a quasi-steady flow pattern in the nozzle is defined as the starting process of the nozzle. No previous experimental research is known for either the starting process or the quasi-steady flow phase of these nozzles.

The divergent nozzles were eliminated from the U. S. design because they seem to present certain problems. Figure 4 presents an experimental and a computational pressure history of a 42 kPa/10 kT blast wave. It is argued that the pressure spike that appears at the front of the blast wave in the experimental, as well as in the computational pressure history, is caused by the divergent nozzles. This argument is supported by computational results (Opalka 1987) which indicate that the greater the cone half-angle of the divergent nozzle, the smaller is the spike at the shock front. It is argued also that the divergent nozzles increase the thrust on the reaction pier because the driver-nozzle combination functions like a rocket motor.

Eliminating the divergent nozzles apparently seems to have a double advantage on the design and the performance of the U. S. LB/TS reducing the thrust on the pier as the drivers empty, as well as eliminating the spike at the front of the simulated blast wave. On the other hand, results of small-scale pilot experiments (Gion 1989) seem to indicate that there are pressure losses connected to the introduction of a large area discontinuity at the exit of the nozzle throat which are lessened when divergent nozzles are used. Therefore, the use of divergent nozzles cannot be easily dismissed. However, if divergent nozzles are included in the U. S. LB/TS design, the nozzle length becomes a critical material parameter which itself depends of the cone half-angle chosen for the nozzle design.

Amann (1968) has shown in his experiments that the start-up time is shortest when the cone half-angle of the divergent nozzle is largest. However, his research was limited to cone half-angles of 5°-15°, and it is not known whether or not the trend continues at higher angles. The BRL one-dimensional, and two-dimensional flow computations (Opalka 1987; Hisley and Molvik 1988) agree with earlier theoretical and experimental research that a recompression shock forms in the nozzles and either stays there for moderate diaphragm pressure ratios, or is swept down the expansion tunnel for higher diaphragm pressure ratios. For want of knowledge,

and for comparison with the numerical predictions, experimental information is needed on the flow start-up process with and without divergent nozzles from 15° to 90°, on the shock formation period, the formation and location of recompression shocks, and on the effect of the cone half-angle on the quasi-steady flow once the start-up process is completed.

3. EXPERIMENTAL APPARATUS

The experimental apparatus at the EMI (Reichenbach and Opalka 1990) consists of: A shock tube, which was especially modified for use in this study; a 24-spark Cranz-Schardin camera and shadowgraph arrangement; and electronic control and recording equipment.

3.1 EMI Shock Tube. The EMI shock tube has a circular cross section with an inner diameter of 200 mm. The driver section is 1.800 m long, and the driven section measures 6.980 m in length (Figure 5). It is followed by a 1.570 m long extension of rectangular crossection, which houses the test chamber. The rectangular cross section of the test chamber is 110 mm high by 40 mm wide with its center located 7.210 m downstream from the diaphragm. The side walls of the test chamber are formed by plane parallel windows (200 mm long by 110 mm high) of high quality optical glass to facilitate optical investigations of the shock wave propagation. An inlet channel of the same shape and cross section as the test chamber and formed of polished aluminum plates protrudes 641 mm upstream into the axisymmetric driven section. A rectangular section is cut out of the arriving shock wave by the sharp inlet edges of the channel walls (cooky cutter principle) to prevent the boundary layers which have formed inside the driven section from entering the test area.

The existing shock tube had to be modified in order to carry out the special task requested with this project. The modifications include a new driver pressure chamber which can be mounted inside the inlet channel, and the various model parts for the divergent nozzles (Figure 6). The length of the driver pressure chamber was chosen to be 1 m in order to delay the arrival of reflections from the end wall. The new driver pressure chamber includes the convergent section and that part of the nozzle throat which lies upstream of the diaphragm (see Figure 6a). The inner cross section of the driver is 64 mm high by 30 mm wide; it converges to a cross section that is 16 mm high by 30 mm wide at the diaphragm. Note that the diaphragm opening shown in Figure 6b is larger than the hight of the nozzle throat. It is reduced to the hight of the throat by lips on the half-nozzle models fitting into the opening (see Figure 7). The diaphragms are composed of two Ultraphan sheets, each 0.1 mm thick, with an ignition wire of 0.08 mm diameter sandwiched between them (Figure 6b). Cellulose acetate sheet (Ultraphan) has the desirable qualities of becoming brittle when stretched and breaking rapidly. With this construction, the diaphragm can be burst at an exactly predetermined moment in time by exploding the embedded wire with a high-voltage pulse.

The test objectives require that the diaphragm be mounted in or near the test section window of the shock tube in such a way that the view of the downstream region of the throat and divergent nozzle is only minimally obstructed. The lengths of the various divergent nozzle configurations (see Figures 6a and 7) necessitate relocating the models in the test section window so that optical records may be taken of all waves of interest from one (200 mm) to three window lengths (600 mm) downstream from the diaphragm. This requirement makes it necessary to locate the diaphragm either at, or one or two times the window length upstream from, the left edge of the test section window. The window locations are labeled B, C, and D in Figure 6a. The location A was not used in this experimental effort.

3.2 Nozzle Configurations. Four convergent-divergent nozzle models were fabricated (Figure 7), thus, producing the four different layouts of the divergent sections shown in Figure 6a. All dimensions were scaled proportionately to the area ratios of the convergent-divergent nozzles used in the CEG-LBS. The 45° convergent section is identical for all nozzle models and part of the driver assembly. The four divergent nozzle configurations are characterized as follows:

a) A 90° divergent nozzle, i.e., a throat without a divergent section dumping the gas directly into the expansion tunnel (Insert 2 shown in Figures 6a and 7a).

b) A divergent nozzle with a 45° cone half-angle extended to the full height of the expansion tunnel (Inserts 2 and 3 shown in Figures 6a and 7b).

c) A 16° divergent nozzle with the area and length ratios of the Q1D-computational CEG-LBS model (i.e., the 7 CEG-LBS nozzles combined into one) extended to the full height of the expansion tunnel (Inserts 2 and 4 shown in Figures 6a and 7c).

d) A 6° divergent nozzle with the area and length ratios and the cone half-angle of the nozzles used in the CEG-LBS design (Inserts 2 and 5 shown in Figures 6a and 7d).

3.3 Instrumentation. A 24-frame Cranz-Schardin spark camera and shadow-schlieren system was the principal tool for the optical study (Figure 8). The sparks from 24 point sources are focussed onto 24 objective lenses of the camera by means of a concave mirror. At the moment a spark is generated, it is projected onto the film plane through the objective lens onto which the image of the spark is copied. This procedure has the advantage of needing no moving parts to align the path of the light rays. Therefore, the optical resolution is determined essentially by the aperture of the objective lenses. Parallax may present a disadvantage in some cases. However, the effect of parallax is minimal in the present setup where a concave mirror with a long focal length ($f = 3.5$ m) is used in conjunction with a test section of shallow depth (40 mm). Parallax was found in these tests to be less than one percent of the length scale.

The density gradients in the flow are made visible by the schlieren method. The basic idea of the schlieren method is that part of the deflected light is intercepted before it reaches the photographic plane, so that the areas of the flow field

through which it has passed appear darker. The Toepler technique (Schardin 1934), using sharp knife edges, was found to yield the best results (see Figure 8). The shadow method visualizes the second derivative of the density and is well suited for the visualization of shock waves. The knife edge is removed and, to generate the shadow effect, the objective lenses are focussed on a reference plane typically at a distance of 400 mm beyond the center plane instead of on the center plane of the test chamber. A point source of light is required for this method to work well. In the EMI system, the light source has a diameter of less than 1 mm. In the following experiments, both methods were combined and, in this way, clear images were obtained of the shock waves as well as of the density gradients.

Other equipment used included a high-voltage power unit, the trigger gauges and electronic delay units for the timing of the Cranz-Schardin camera, and several 12-bit transient recorders. Kistler quartz pressure gages of type 603B were used to sense the static pressure. They have a characteristic frequency response of approximately 500 kHz. Electrical filters with a maximum frequency response of 180 kHz were installed between the pressure gauges and the charge amplifier in order to prevent an overshoot of the signal.

3.4 Test Conditions and Procedure. The four model configurations were tested at seven driver pressure levels; namely, at $P_{41} \equiv P_4/P_1 = 4$, 14, 38, 55, 80, 110, and 188. To test the functionality of the modified shock tube and to get a feel for the starting process of the various nozzles, the models were tested at the lowest specified driver pressure level ($P_{41} = 4$) first. The tests then continued with the next highest driver pressure level ($P_{41} = 14$). The operating driver pressure was 1.3 MPa (13 bar) over atmospheric pressure, except for the lowest driver pressure ratio where the driver pressure was 300 kPa (3 bars) over atmospheric pressure. The actual initial test conditions are listed in Table II for all experiments. The experimental driver pressure p_4 given in the table is the fill pressure above atmospheric pressure and is related to the absolute driver pressure by $p_4 = P_4 - P_0$. The individual letters B, C, and D indicate the window location at which the optical records were taken (see Figure 6a). The combination of B/C and C/D indicates that the window was located halfway in between the positions shown in Figure 6a.

The test preparation was begun by installing the desired model configuration and the diaphragm. The shock tube was then closed, the Cranz-Schardin camera and the pressure recorders were readied, and all electrical connections were checked. The recording film holder was opened in the darkened room and the firing and recording controls were activated before the driver was pressurized. Once the driver had reached the specified pressure, the driven section was evacuated as necessary until the desired driver pressure ratio was established (see Table II). The rupturing of the diaphragm was initiated with an electric pulse of 10-20 kV to explode the wire embedded between the two Ultraphan layers of the diaphragm. The same pulse triggered the camera and the other recording equipment after some preset delay time.

TABLE II. INITIAL TEST CONDITIONS

Config/P_{41}	Shot #	Window Pos.	P_0 *mbar*	T_0 *°C*	p_4 *bar*	P_1 *mbar*	P_{41}
90° Half-Nozzle (N90)							
N90/004	13249	B	990	22.7	3.0	990	4.030
"	13254	B	989	23.5	"	989	4.033
N90/014	13258	B	988	22.6	13.0	988	14.16
N90/038	13310	B	996	23.2	13.0	368	38.03
N90/055	13301	B	992	24.2	13.0	254	55.09
"	13302	B	992	23.7	"	"	55.09
N90/080	13311	B	996	23.4	13.0	174	80.44
N90/110	13314	B	993	23.5	13.0	127	110.2
N90/188	13312	B	994	23.9	13.0	74	189.1
"	13313	B	993	23.2	"	"	189.1
45° Half-Nozzle (N45)							
N45/004	13244	B	990	24.6	3.0	990	4.030
"	13253	B	990	23.2	"	"	4.030
N45/014	13259	B	988	23.3	13.0	988	14.16
"	13265	B/C	995	24.3	"	995	14.07
N45/038	13309	B	995	22.5	13.0	368	38.03
N45/055	13303	B	992	24.3	13.0	254	55.09
"	13321	B/C	993	23.8	"	"	55.09
N45/080	13308	B	990	24.2	13.0	174	80.40
"	13319	B/C	994	22.3	"	"	80.43
N45/110	13306	B	990	24.0	13.0	127	110.2
"	13320	B/C	993	23.5	"	"	110.2
N45/188	13307	B	990	24.2	13.0	74	189.1
"	13318	B/C	990	24.8	"	"	189.1

The principle of the electronic control circuit for the experimental process can be seen in Figure 9. The preset delay time between the ignition pulse for bursting the diaphragm and the first spark pulse of the Cranz-Schardin camera was measured by a time counter. Some interference from the strong trigger pulse was suffered on the recording equipment, and a few pressure records were lost. A test log was kept to record these events together with the initial test and ambient conditions for each

shot, the trigger times for the pressure recorders and for the Cranz-Schardin camera, and the spark frequencies for the camera.

TABLE II. INITIAL TEST CONDITIONS (continued)

Config/P_{41}	Shot #	Window Pos.	P_0 *mbar*	T_0 *°C*	p_4 *bar*	P_1 *mbar*	P_{41}
			16° Half-Nozzle (N16)				
N16/004	13245	B	986	24.7	3.0	986	4.043
"	13246	C	990	23.6	"	990	4.030
N16/014	13260	B	988	23.5	13.0	988	14.16
"	13264	C	994	23.8	"	994	14.08
N16/038	13317	B	990	24.3	13.0	368	38.02
"	13322	C	993	22.2	"	"	38.02
N16/055	13304	B	992	24.8	13.0	254	55.09
"	13323	C	993	22.8	"	"	55.09
N16/080	13316	B	993	24.0	13.0	174	80.42
"	13324	C	993	23.0	"	"	80.42
N16/110	13305	B	990	23.4	13.0	127	110.2
"	13325	C	993	23.7	"	"	110.2
N16/188	13315	B	993	24.1	13.0	74	189.1
"	13326	C	993	24.0	"	"	189.1
			6° Half-Nozzle (N06)				
N06/004	13247	B/C	987	24.0	3.0	987	4.040
"	13248	C/D	985	24.5	"	985	4.046
N06/014	13261	B	990	23.6	13.0	990	14.13
"	13262	C/D	994	23.0	"	994	14.08
"	13263	C	994	23.4	"	994	14.08
N06/038	13327	C/D	993	23.0	13.0	368	38.02
N06/055	13328	C/D	993	23.2	13.0	254	55.09
N06/080	13329	C/D	992	24.5	13.0	174	80.41
N06/110	13330	C/D	992	25.5	13.0	127	110.2
N06/188	13331	C/D	992	24.5	13.0	74	189.1

4. EVALUATION OF EXPERIMENTAL DATA

The nozzle flow start-up phenomena observed and the data reduction methods used are described in this section. With each test shot, 24 shadow or schlieren pictures were recorded on film by the Cranz-Schardin camera at constant time intervals. A set of the optical records was forwarded by EMI to BRL for data reduction and analysis. The complete set of X-t diagrams of the evaluated optical records is presented in Appendix A.

The static pressure was recorded at three available gage locations in the tunnel ceiling, 270 mm, 760 mm, and 889 mm downstream from the center of the test section window. The pressure was recorded at all seven driver pressure ratios for the 90°, 45°, and 16° divergent half-nozzles in the window position B for which the diaphragm is located at the upstream edge of the test section window, 100 mm from its center. A set of the pressure records was also forwarded by EMI to BRL for evaluation.

4.1 Description of Typical Flow Phenomena. The 16° divergent half-nozzle appears to be best suited for an explanation of the typical flow start-up phenomena observed in this study because the available field of view (400 mm) is the longest among the four configurations under investigation. Two test runs were needed to record the flow throughout the entire length of the 16° half-nozzle because the field of view of the optical window was limited to 200 mm. One test run covered the first 200 mm of the 16° half-nozzle (window position B), and another test run covered the range from 200 - 400 mm behind the diaphragm location (window position C). Therefore, each snapshot in time as, e.g., shown in Figure 10 is composed of two separate photographic records. A heavy vertical line halfway through the nozzle of some of the snapshots indicates that the fields of view of the two photographs did not quite overlap.

A low-pressure case was chosen to illustrate the flow start-up phenomena because all the phenomena of interest remain within the field of view until the start-up process of the nozzle is completed. A sample sequence of shadowgraphs for the 16° divergent half-nozzle (N16) at the driver pressure ratio $P_{41} = 14$ (Code N16/014) is presented in Figures 10a and 10c. The major nozzle flow phenomena were traced from these photographs and are illustrated in Figures 10b and 10d. Figures 10a and 10b show the early phase of the flow start-up process, and Figures 10c and 10d show the late phase of the flow start-up process. Flow phenomena like the incident shock, the contact surface, boundary layer build-up, regions of flow separation, and a system of multiple recompression shocks can be seen developing and moving within and past the field of view. They are described in the following paragraphs.

The **incident shock** begins to form immediately after the flow is initiated by bursting the diaphragm. Since the diaphragm breaks into fragments of uneven sizes, the opening process is asymmetrical and causes an uneven flow progress across the height and depth of the throat. Initially, the shock consists of a system of two to three curved compression waves which catch up with each other inside the throat

channel (Figures 10a,b at 106 μs after diaphragm break) and reflect from the ceiling and the floor of the throat channel combining eventually into one incident shock (206 μs). This formation period may take up to about 500 μs at the low end of the driver pressure range, by which time the shock has progressed well into the divergent section of the half nozzle (606 μs). A shock reflection is generated at the ceiling of the half nozzle exit (Figures 10c,d at 821 μs) proceeding across the flow area and reflecting later on at the floor plate of the expansion channel.

The **contact surface** between the expanding driver gas and the gas in the low-pressure region of the divergent half-nozzle follows the incident shock at close range. It can be easily detected because the associated flow turbulence, which it brings with it, changes the texture of the background in the photographs (see Figures 10a and 10c). Because of the turbulence, the contact front is very rugged. Often, darker strings perpendicular to the flow direction can be detected in the turbulent region behind the contact front (e.g., Figure 10a, 606 μs). It is thought that these strings are combustion products of the exploding wire that ruptures the diaphragm, rather than compression waves which dissipate with time (Figure 10c, 1.321 ms). Once the contact surface has entered the divergent section of the half-nozzle, a variety of phenomena begin to occur simultaneously.

An **expansion fan** begins to develop at the exit of the throat channel, at the corner with the divergent section of the half nozzle. It is best seen in Figure 10c; in Figure 10a, the diaphragm fragments exiting the throat channel obscure the image of the developing expansion fan. Inside the divergent section of the half-nozzle, a **recompression shock** begins to form (606 μs). This shock develops into a bottle shock spawning a second shock ahead of itself (Figure 10c, 1.322 ms). The second shock also develops into a bottle shock and may spawn a third shock ahead of itself in the process (1.822 ms). Extensive **flow separation regions** at both ceiling and floor of the divergent half-nozzle develop during this process due to the boundary-layer build-up in the flow channel. With the boundary layer well developed, the system of bottle shocks changes into a system of **multiple X-type recompression shocks**. The start-up process of the nozzle comes to completion when this system of multiple X-type shocks becomes stationary either inside the nozzle, as in the present case shown in Figures 10c and 10d (2.322 ms), or downstream from the divergent half-nozzle for high driver pressure ratios, as suggested in the photographs shown in Figures 11b and 12.

Throat shocks appear inside the throat channel as a consequence of the boundary-layer build-up (406 μs and later). As many as six shocks have been observed at the lowest pressure level (P_{41} = 4). Two of these warrant special mention because of their general presence at almost all test conditions. The narrowest cross section exists at the diaphragm location. Once the flow reaches the sonic condition in this cross section, it expands supersonically upon exiting into the throat channel and a standing X-type recompression shock appears between 10-15 mm downstream from the diaphragm location (606 μs) at all pressure levels except the lowest one. A second, bifurcated recompression shock appears in the throat channel at about 50-60 mm downstream from the diaphragm location and remains there

throughout the start-up process of the nozzle (821 μs and later). A strong shock at first, it separates into multiple bifurcated or multiple X-type shocks at later times.

Perhaps the biggest surprise in these photographs is the discovery of the asymmetric flow through the divergent half-nozzle. It was the expectation of the experimenters to obtain one-half of a symmetrical flow pattern above the center axis of the nozzle. This was accomplished for the flow ahead of and up to the contact surface. Behind the contact surface, however, the boundary-layer build-up along the floor plate and the ceiling eventually causes the flow to separate. The flow then seeks its own path by turning and more or less following the centerline of the half-nozzle.

4.2 Vortices, Fragments, and Other Curiosities. The 90° half-nozzle is a nozzle without a divergent section. Two examples of the flow start-up process in the 90° half-nozzle are presented in Figure 11. Figure 11a shows a sequence of selected shadowgraphs for the lowest driver pressure ratio tested, $P_{41} = 4$ (Code N90/004). Recompression shocks can be seen in the throat and in the flow channel downstream from the throat exit where the flow begins to turn, but the typical X-type shock near the diaphragm is not seen at this pressure level. A system of five recompression shocks develops in the throat of which one shock becomes stationary at the throat exit and another one becomes stationary a short distance downstream from the throat exit.

The interesting phenomenon of this case (N90/004) is the big vortex that fills the corner downstream from and above the exit from the throat channel while the flow continues straight ahead in a channel the height of the throat along the floor of the expansion tunnel. The vortex can be seen beginning to develop in Figure 11a at 0.302 ms and filling the entire dead-water region at about 1.302 ms. This vortex flow suggests that a sizable amount of internal energy is used up by the filling of the dead-water region formed by the area discontinuity at the throat exit; and this energy loss should have an influence on the downstream pressure recovery.

This pressure level is one of two at which such a big vortex was observed for the 90° half-nozzle configuration. At the next higher pressure level, $P_{41} = 14$, the vortex is equally big but fills the dead-water region faster and takes on a different appearance because the structure of the turning flow is distinctly different from the present case. The lack of observing such distinct vortices at higher pressure levels (i.e., $P_{41} = 38$, and above) does not, however, imply that they do not exist. Rather it is surmised that due to the turning of the flow and the faster equalization of the static pressure in the corner, they may have been missed at the relatively coarse sampling sequence employed in these tests.

The mainstream flow out of the throat in Figure 11a continues straight ahead for the entire length of the test section without turning (see picture at 2.102 ms) and the schlieren picture at 1.702 ms shows a very distinct slip stream commencing at the throat exit and continuing through the range of observation. Unfortunately, the flow further downstream from the throat exit could not be observed because it was not possible to mount this configuration further upstream from the test section

window. This proved a major handicap at the higher pressure ratios where the flow phenomena of interest all moved past the field of view before the start-up process was completed.

Figure 11b shows a sequence of selected shadowgraphs for the start-up process at the highest driver pressure ratio investigated, P_{41} = 188 (Code N90/188). A bottle shock can be seen to develop early in the start-up process (240-390 μs) before the recompression shock moves out of the field of view. From 240 μs on, the flow appears to expand linearly at an increasing angle and steadying at 45° after 690 μs. The flow expansion appears to be disturbed by the strong reflection of the incident shock from the ceiling at 540 μs. By this time, the recompression shock has moved beyond the field of view, and the start-up process has escaped observation to its completion.

The flow start-up process in the 45° half-nozzle is illustrated in Figure 12 for the driver pressure ratio, P_{41} = 80 (Code N45/080). For this configuration, a field of view of 300 mm was available which allowed us to observe the start-up flow phenomena for a longer distance downstream from the throat exit than for the 90° half-nozzle. Still, the field of view is too limited to record all recompression shocks up to the completion of the start-up period. The shadowgraph sequence in Figure 12a shows that a bottle shock has formed at 385 μs, before the diaphragm fragments enter the divergent part of the half-nozzle. At later times (Figure 12b), the expanding flow and the bottle shock are disturbed by the reflected shock from the ceiling of the expansion tunnel and by the diaphragm fragments.

The fragments of the ruptured diaphragms present an unavoidable disruption of the flow field in all test cases. In the example shown (Figure 12b), the diaphragm fragments are seen to disrupt the bottle shock from 803 μs to 1.103 ms. As the fragments leave the scene, the bottle shock recovers and becomes stationary within the field of view (1.463 ms). However, the second recompression shock which had already formed ahead of the bottle shock at 803 μs has moved beyond it. The throat shocks also are clearly visible in all the photographs of Figure 12.

The start-up process of the nozzle is also characterized by the flow separation along the upper wall of the divergent nozzle. Initially, the flow separates at the throat exit. A distinct slip stream can be seen at 385 μs commencing at the throat exit. As the start-up process continues, the separation point moves up along the wall toward the nozzle exit at the ceiling of the expansion channel until a stable condition is reached (1.103 ms). The dead-water region near the corner is considerably smaller than the one observed with the 90° half-nozzle and much of the flow vorticity is avoided with the addition of the 45° divergent nozzle. The significance of the effect which the 45° divergence has on the flow will be discussed in the following section.

4.3 Data Reduction Procedures. The shadow and schlieren pictures were evaluated by measuring the distances of the various flow phenomena from a reference point in the photograph with the help of a digitizing pad that was controlled by

a Zenith PC. The measured locations of these flow phenomena, e.g., incident shock, contact surface, various recompression shocks, and some diaphragm fragments, with reference to the diaphragm location (X = 0), were then recorded as functions of time measured from the bursting of the diaphragm (t = 0). From these records, X-t diagrams were generated on an Alliant FX/1 computer using PVI (Precision Visuals, Inc. 1986) software. The data points for the window positions, B/C (100-300 mm), C (200-400 mm), and C/D (300-500 mm), downstream from the diaphragm location were matched with the data points for the window position B (0-200 mm) by adding a time difference to the 24 recorded spark times so that the data points for the incident shock recorded in the downstream window positions C and D would continue on a straight line drawn through the last three data points for the incident shock recorded in window position B. All X-t diagrams are shown in Appendix A.

It was learned from the X-t diagrams that the data points for the incident shock generally follow a cubic polynomial. From the X-t diagram for case N16/014, e.g., one can learn that the incident shock and the contact surface initially accelerate in the throat of the nozzle, become constant for a short period of time, and, finally, decelerate in the divergent section of the nozzle. Therefore, a least-sqares polynomial of third degree was fitted to the data for the incident shock to determine the intercept in time and this value was then used to correct the spark times so that the data for the incident shock and the contact surface would pass through the origin of the plot.

Measurements of the static pressure were taken at three available locations along the ceiling of the expansion tunnel, 370 mm, 860 mm, and 989 mm downstream from the diaphragm location. Examples are shown in Figures 13 - 15. Noise caused by the high-voltage trigger signal can be detected at time zero. Most of the pressure records show two, and sometimes three, shocks arriving at the gage positions in short succession of each other (about 10 - 50 μs apart). In a first attempt at evaluation, these pressure peaks were measured, scaled, and recorded with their respective arrival times for each of the three gages. A comparison of the shock recovery for the three half-nozzles using the pressure peaks of the pressure histories, however, proved unsatisfactory and was discarded. Consequently, it was decided to use a different approach.

In a second attempt at evaluation, the height of the pressure plateau behind the incident shock(s) was determined from the pressure records averaging out the pressure fluctuations by inspection. This judgement appeared somewhat subjective because the fluctuations of the pressure traces are considerable indeed; however, this approach was more successful than the first one. In one-third of the records, the pressure plateau agreed with the first pressure peak (Figure 13), in another third it coincided with the second pressure peak (Figure 14), and in the last third of the records it fell in between the two pressure peaks (Figure 15). From the measurements, the shock strength, P_{21}, was determined and plotted versus the driver pressure ratio, P_{41}, and the shock Mach number, M_s. The results are discussed in the following section.

5. DISCUSSION OF RESULTS

The objective of this experimental investigation was to gather information on the flow start-up phenomena in convergent-divergent nozzles such as are used in large blast simulators. Of particular interest was the time required for the incident shock to form, the influence of the divergent nozzle angle on the shock recovery, the flow start-up period, and a comparison with computational predictions of the flow start-up process. Subsequently, the shadowgraphs, X-t diagrams, and pressure records were evaluated with this objective in mind. The flow start-up period, the shock formation process, the flow expansion in the divergent nozzles, and the pressure recovery for the 16°, 45°, and 90° nozzles were summarized in graphs of the defined nozzle characteristics versus driver pressure ratio or the shock Mach number and are discussed in this section.

The 6° half-nozzle was excluded from the discussion because the available data were too limited in scope. Except at driver pressure ratios P_{41} = 4 and 14, optical records were obtained only in window position C/D which afforded a view of the area discontinuity at the nozzle exit. The area discontinuity, it turned out, had an effect comparable to that of the 90° nozzle in that the nozzle acted like an extended throat channel and, with the exception of the formation of the incident shock and the throat shocks, the start-up phenomena of interest occured mostly downstream from the nozzle exit. The field of view in this position proved to be too limited to successfully record the flow start-up processes.

5.1 Flow Start-up Period. The start-up process of the nozzle was defined in Section 2.3 as the time from the rupturing of the diaphragm to the establishment of a quasisteady flow pattern in the nozzle. All flow phenomena observed during the start-up process of the half-nozzles are well known from previous research of the steady flow in ducts and nozzles at various exit pressure ratios of the nozzle (Emmons 1958). The only difference for unsteady flow appears to be that all these various phenomena appear together in the course of one flow sequence changing from one into another with time. For example, a single, strong, bifurcated throat shock changes with time into weaker, multiple bifurcated shocks and still later into multiple X-type shocks in response to the changing back pressure ratio of the nozzle. This holds also true for the system of recompression shocks which develops in the divergent nozzle and downstream from its exit, respectively.

The flow start-up period was determined from the X-t diagrams for three half-nozzles. It is shown in Figure 16 as a function of the driver pressure ratio. The data show that the flow start-up period decreases for all nozzles with increasing divergent angle. The flow start-up period for the 16° half-nozzle could be determined for three pressure levels only (P_{41} = 14, 38, 55) because either the recording-time periods, or the field of view for the other test cases were insufficient. These data points are close above those for the 45° nozzle. The relatively large difference in start-up time for the 90° half-nozzle as compared to the 45° half-nozzle can be explained by the fact that the flow start-up period for this nozzle was determined from the data for the throat shocks because the field of view behind the throat exit

was too limited to observe the entire start-up process. It is surmised that if the entire start-up process could have been observed, the differences in start-up time between the 45° and 90° half-nozzles would have been found smaller, because in those cases in which it could be observed (e.g., case N16/014 and N45/080), the X-t diagrams reveal that the system of bottle shocks downstream from the nozzle exit becomes stationary at somewhat later times than the throat shocks.

5.2 Shock Formation. In the general description of the flow phenomena in Section 4.1, it was mentioned that the incident shock starts out as a series of compression waves which catch up with each other in the throat channel of the nozzle (e.g., Figure 12, 75 μs). The incident shock is further built-up by shock reflections from the bottom or the ceiling of the throat channel (Figure 12, 135 μs) and appears to be well-formed a short time after it has emerged from the throat channel (Figure 12, 255 μs). These observations could be made in all test cases and Figures 10 - 12 present typical examples of the formation of the incident shock. The approximate period and distance of shock formation were determined by inspection from the optical records for each test case and the results are plotted in Figure 17.

Figure 17a shows the time it takes the incident shock to be well-formed as a function of the driver pressure ratio for the three half-nozzles. The results indicate that the incident shock forms fastest in the 16° half-nozzle and slowest in the 90° half-nozzle. The time difference between the two configurarions appears to be approximately 50 μs over the whole range of driver pressure ratios. The shock formation in the 45° half-nozzle presents a transition between the other two nozzles starting out with periods even longer than in the 90° nozzle at the two lowest pressure levels, and ending up with shock formation periods almost identical to the 16° nozzle at pressure ratios above 40. Figure 17b presents the interesting result that the shock formation distance is practically constant over the whole pressure range tested.

The differences found in the shock formation periods for the three nozzle angles may be significant for the LB/TS design if these times scale with the volume of the facility. The statistical significance of the differences found is minimized however by the tolerances involved in their determination. The tolerance associated with each data value is proportionate to the time interval which was used for sequencing the light sparks of the Cranz-Schardin camera. At the lower end of the pressure range, the time interval between data points is 100 μs, and at the upper end of the pressure range it narrows down to 40 μs. As a result, the differences in shock formation period between the three nozzles may be insignificant altogether because they are of the same magnitude as the tolerances involved in measuring them.

5.3 Flow Expansion and Separation. The most significant flow feature of the 90° half-nozzle is that the flow forms its own divergent nozzle. As the driver gas behind the contact surface leaves the throat channel, the flow begins to expand at some angle depending on the back pressure at the throat channel exit. This angle can be identified by the slip stream visible in the shadowgraphs (e.g., Figure 11).

The expansion angle approaches a quasi-steady value once the local disturbances caused by the shock reflections from the ceiling and the floor have died down and the diaphragm fragments have passed (e.g., Figure 11b, 915 μs). The flow expansion angle was determined by reading and averaging the maximum and minimum angles of the slip stream in the shadowgraphs and schlieren pictures at late times close to the completion of the start-up process. It is plotted versus the driver pressure ratio in Figure 18a and compared to the flow expansion angles in the 45° and 16° half-nozzles which were determined in the same manner. The results in Figure 18a show that the flow stays attached in the 45° nozzle for driver pressure ratios of 55 and above but seeks its own expansion angle at lower pressure ratios. In the 16° half-nozzle, the flow stays attached for driver pressure ratios above 14.

The complimentary phenomenon to flow expansion is the separation of the flow from the walls of the diverging duct that is formed by the nozzle configurations. The flow separation angle for the three half-nozzles is plotted versus the driver pressure ratio in Figure 18b. In the 90° half-nozzle, the flow has no choice but to separate upon exiting at the exit of the throat channel. The flow separation angle is defined in the same manner as the flow expansion angle and is therefore equal to the latter. In the 16° nozzle, on the other hand, flow separation is almost nonexistent. Only at the two lowest driver pressure ratios does the flow separate halfway through the nozzle due to the boundary layer build-up. At pressure levels above 14, the flow stays attached to the nozzle walls almost to the nozzle exit, where it forms a small dead-water region to negotiate the corner at the ceiling of the expansion tube.

In the 45° divergent half-nozzle, flow separation occurs at the three lowest driver pressure levels tested, i.e., P_{41} = 4, 14, and 38. At these pressures, the flow separates at the exit corner of the throat channel for the entire flow start-up period. At higher driver pressure levels, flow separation occurs early on in the start-up process at the exit corner of the throat channel but as the start-up process continues, the separation point moves downstream along the ceiling toward the exit of the divergent nozzle. Toward the end of the start-up process, the separation point becomes stationary at some point along the ceiling of the divergent nozzle. The flow then stays attached to the ceiling of the divergent section of the half-nozzle.

The flow separates at a point near the corner of the nozzle exit, creating a dead-water region to negotiate the corner formed by the divergent nozzle and the expansion tube. The function of the flow separation angle for the 45° half nozzle in Figure 18b shows a maximum about the driver pressure ratio, P_{41} = 40, and slightly smaller separation angles for the higher pressure ratios. It is noted that this is not the same angle as the flow expansion angle shown in Figure 18a. In comparison to the 90° half-nozzle, however, the flow through the 45° half-nozzle showing separation angles of the same magnitude avoids much of the vorticity found in the flow field at the area discontinuity of the 90° half-nozzle.

5.4 Pressure Recovery. The static pressure history was recorded by pressure gages mounted in three locations along the ceiling of the expansion tunnel, i.e., 370mm (gage # 37), 860mm (gage # 86), and 989mm (gage # 99) downstream from the diaphragm location. The incremental shocks seen in these records following the incident shock are most likely caused by reflections of the curved shock front from the walls of the expansion tunnel as shown by Amann (1985). From the records of the pressure histories at these gage locations, the plateau pressure behind the incident shock was determined and plotted versus (a) the driver pressure ratio and (b) the shock Mach number for all half-nozzles tested. An approximate smooth curve or a linear least-squares regression was fitted through the data points for each half-nozzle. The results are shown in Figures 19-21 for the three gage locations.

The results of shock strength, P_{21}, versus driver pressure ratio P_{41}, at gage # 37 (Figure 19a), closest to the diaphragm location, do not present conclusive evidence for a loss of shock overpressure as a function of the angle of divergence in the nozzles. Over the whole range of driver pressure ratios, both the 90° as well as the 16° half-nozzles show nearly identical shock overpressures which are higher than the corresponding values for the 45° half-nozzle. However, when plotted versus the shock Mach number, M_s, (Figure 19b), the shock strength in the 16° half-nozzle appears to be higher than in the other two nozzles for the same shock Mach number. Therefore, the results are apparently somewhat ambiguous at this gage location because of the closeness to the nozzle exits. But, at distances further away from the nozzle exits, at gages # 86 and # 99, the loss of shock overpressure with increasing angle of divergence is defined clearly.

The approximate curve fits of the shock strength versus driver pressure at gage # 86 in Figure 20a suggest that the 16° divergent half-nozzle produces an enhanced shock strength compared to that obtained without a divergence, i.e., the 90° half-nozzle. The difference in shock strength between the two nozzles amounts to 7.8 percent at the highest driver pressure ratio (P_{41} = 188). The gain in shock strength behind the 45° nozzle is 3.5 percent compared to the shock strength behind the 90° half-nozzle at the maximum pressure ratio. The corresponding data at gage # 99 seem to indicate an enhancement of 11 percent of the shock strength for the 16° half-nozzle and of 7.8 percent for the 45° half-nozzle over the shock strength for the 90° half-nozzle at the upper end of the pressure scale. These results agree with those of small-scale LBS-model experiments carried out at the BRL (Coulter 1987; Gion, Private Communication) indicating a 10 percent enhancement in the shock strength for drivers equipped with 6° divergent nozzles.

Plotting the shock pressure ratios against the shock Mach number (Figures 19b-21b), and fitting them with a linear least-squares regression, reveals the uncertainties involved in the measurements. Ideally, all data points would fall on a straight line, but in reality there exist inaccuracies in measurement. The correlation is very good, however; all regressions have correlation factors above 0.9974 and the correlations improve with distance from the diaphragm location to better than 0.9992 at the gage location furthest away from the diaphragm.

An estimate of the uncertainties of the results was also attempted by comparing the data points from gage # 86 with those from gage # 99. The records of the shock overpressure of these gage positions indicate that the pressure loss between them is negligible if existent at all. The distance between the two gages is only 129 mm, and, in many instances, a higher pressure was recorded at the more distant gage. The relative differences in the measurements of the shock pressure at these gages, $\delta P_{86-99} = (P_{86} - P_{99})/P_{99}$, may therefore be used to determine the experimental uncertainties. The uncertainties of the experimental measurements are defined by the arithmetic mean, $\bar{x}$, of the differences of all these pressure measurements and their standard deviation, σ_{n-1}. The arithmetic mean was determined to $\bar{x} = 0.0175$, or 1.75 percent with a standard deviation of $\sigma_{n-1} = 0.0136$, or 1.36 percent of the relative differences in the pressure measurements. This result implies that the loss in shock strength between the 16° and the 90° half-nozzles of about 10 percent is statistically significant and therefore real.

5.5 Comparison of Experimental Data with Computational Results. A systematic comparison of the experimental data of this study with BRL-Q1D code computational results was carried out and is presented in Appendix B. The BRL-Q1D code (Opalka and Mark 1986) is a computer program written in FORTRAN 77 language that uses quasi-one-dimensional, adiabatic, inviscid, numerical algorithms to solve the Euler equations. The code incorporates two computational techniques. One is an implicit finite-difference technique developed by Beam and Warming, the other is an explicit finite-difference technique according to MacCormack. These techniques are applied to the quasi-one-dimensional Euler equations in their weak conservation form. The governing equations are derived for arbitrary geometries and transformed into a uniform computational grid retaining the weak conservation form. Linear and non-linear gridding options are available. The implicit technique (Beam and Warming 1979) was used in this application. Central spatial differencing casts the difference equations into a block-tridiagonal structure which is solved for the increments in the dependent variables at each successive time step.

The BRL-Q1D code can provide only a rough, qualitative estimate of the complex flow start-up process in convergent-divergent nozzles because it is limited to one flow dimension and does not model viscous effects. Generally, the computational results are fair considering the inherent limitations of the code. The flow phenomena observed in the experiment are generally reproduced by the computations as long as they are not strongly dependent upon viscous effects. With the exception of the 90° half-nozzle, the experimental incident shock and contact surface are matched by the computational data for low driver pressures. With increasing driver pressure, however, the experimentally observed initial flow acceleration and shock formation phase becomes more pronounced. Hence, an increasing discrepancy between the experimental and the computational paths for the incident shock and the contact surface is observed with increasing driver pressure.

The system of recompression shocks observed in the experiment coexists with, and is functionally dependent upon, the boundary layer build-up during the start-up period of the nozzles. The boundary layer and the recompression shock system

cannot be modeled by the inviscid computational scheme. With the exception of the 6° half-nozzle, the computations predict only one recompression shock which generally does not coincide with the experimental system, and moves much slower than the experimental shocks at low driver pressures, and much faster at high driver pressures. In between, there exists one pressure level at which the computational recompression shock happens to coincide with one of the experimental shocks. This pressure level is different for each divergent nozzle angle.

The experimental evidence suggests that the system of multiple X-type recompression shocks does not move nearly as far downstream into the expansion tunnel as does the computational single recompression shock and decays faster than the computation predicts. The computation also cannot predict the standing recompression shocks in the throat channel. It predicts a moving shock instead which weakens and dissipates as it approaches the exit of the throat channel. For the 90° half-nozzle, the computation produces a standing recompression shock at the exit of the throat channel at all pressure levels in addition to the aforementioned shock.

6. CONCLUSIONS

Four convergent-divergent nozzle configurations were successfully tested at seven driver pressure ratios to study their flow start-up processes. However, the field of view for the 6° divergent half-nozzle and the 90° half-nozzle downstream from the nozzle exit was too limited, and additional optical test records are desirable for a comparative study of the flow start-up processes downstream from the exits of the 90° and 6° half-nozzles. The results for the 6° divergent half-nozzle were not discussed here because they were too incomplete to contribute to the discussion.

The pressure histories and the optical flow records reveal that the flow is very sensitive to local disturbances, e.g., flow asymmetries caused by the breaking of the diaphragm, the passage of the diaphragm fragments through the flow field, and the boundary-layer build-up during the start-up period of the nozzles. Strong reflections of the incident shock at the exit corner of the 45° and 90° half-nozzles interfere with the flow during the start-up process. A system of multiple recompression shocks is generated by the flow in the throat channel and in the divergent section of the half-nozzle in response to the boudary layer build-up along the walls of the flow channel.

From the observations and the analysis of the available data, the following conclusions could be drawn.

a) The 90° nozzle effectively forms a divergent section by establishing its particular flow expansion angle in response to the particular driver pressure ratio, but the penalty to be paid is a loss in shock strength of about 10 percent compared to the shock recovery in the 16° divergent half-nozzle at the highest driver pressure ratio.

b) The shock formation period ranges from 440± 50μs at the low end of the pressure scale to 250± 25μs at full scale for all nozzles. The shock formation distance is practically constant over the entire pressure range with a mean value of 157mm and a standard deviation of the recorded values of σ_{n-1} = 16mm.

c) The start-up period of the 45° nozzle ranges from 2.55ms at the lowest pressure level (P_{41} = 4) to 1.12ms at the highest pressure level (P_{41} = 188). The information on the start-up period for the other nozzles is incomplete.

d) No pressure spikes at the incident shock front of the pressure histories were observed in these experiments such as were found in the experimental CEG-LBS pressure histories or in the BRL-Q1D computations. This is thought to be due to the low area expansion ratio (1:7.5) between the throat and the expansion tunnel.

e) The BRL-Q1D code proved to be an inappropriate tool for studying the detailed flow phenomena of the start-up process in nozzles. It remains a useful engineering tool for generating 0th-order estimates of such flow phenomena and for parametric design studies in shock tubes and tunnels.

Based on the present findings, it is recommended that the experiment be repeated for higher throat/test-section area expansion ratios of 1:15 and 1:30 with redesigned divergent nozzle models of 16°, 30°, 45°, and 90°. The influence of a partial area discontinuity at the nozzle exit should be studied in this future phase of the experiment. Since the half-nozzle configuration did not yield the desired one-half symmetrical flow pattern above the center axis (p. 12), future tests should include at least one full-nozzle configuration.

The 90° half-nozzle is of special interest to the project engineer because the elimination of the divergent nozzles from the LB/TS design saves a great deal of material cost in nozzle construction. It was found that the flow through the 90° half-nozzle with its area discontinuity at the throat channel exit behaves like the flow through the 45° half-nozzle but yields a lower shock pressure than the latter. The money saved by not having an efficient nozzle design may be lost several times over by requiring a higher design pressure for the drivers and, thereby, thicker walls and a stronger pressure delivery system. Therefore, 45° divergent nozzles are recommended for the full-scale LB/TS to avoid additional losses in shock pressure.

REFERENCES

Amann, H.-O. "Vorgaenge beim Start einer ebenen Reflexionsduese" (Processes during the Start-up of a Planar Reflection Nozzle). Report Nr. 9/68, Fraunhofer Gesellschaft, Ernst-Mach-Institut, Freiburg im Breisgau, (West) Germany, 1968.

Amann, H. O. "Das Spike Problem bei der Simulation von Blastwellen" (The Spike Problem in Simulated Blast Waves). EMI-Report E13/85, Fraunhofer Gesellschaft, Ernst-Mach-Institut, Freiburg im Breisgau, (West) Germany, May 1985.

Beam, R. M., and R. F. Warming. "An Implicit Factored Scheme for the Compressible Navier-Stokes Equations II:/ The Numerical ODE Connection." Paper No. 79-1446, AIAA 4th Computational Fluid Dynamics Conference, Williamsburgh, VA, 23-24 July 1979.

Cadet, A., and J. B. G. Monzac. "The Large-Scale Nuclear-Blast Simulator of the Gramat Research Center: Description and Operational Utilization." Proceedings of the Seventh International Symposium on the Military Application of Blast Simulation (MABS-7), vol. 1, paper no. 1.2, Medicine Hat, Alberta, Canada, 13-17 July 1981.

Coulter, G. A. "Blast Parametric Study Using a 1:57 Scale Single Driver Model of a Large Blast Simulator", BRL-MR-3597, U.S. Army Ballistic Research Laboratory, Aberdeen Proving Ground, MD, June 1987.

Emmons, H. W. (ed.) "Fundamentals of Gas Dynamics." High Speed Aerodynamics and Jet Propulsion, vol. III, New Jersey: Princeton University Press, 1958.

Ethridge, N. H., R. E. Lottero, J. D. Wortman, and B. P. Bertrand. "Computational and Experimental Studies of Blockage Effects in a Blast Simulator." ARBRL-TR-02564, U.S. Army Armament Research and Development Center, Ballistic Research Laboratory, Aberdeen Proving Ground, MD, June 1984.

Gion, E. J. "A Multiple Driver Shock Tube Model of a Large Blast Simulator." BRL-MR-3757, U.S. Army Ballistic Research Laboratory, Aberdeen Proving Ground, MD, May 1989.

Gion, E. J. U.S. Army Ballistic Research Laboratory, Aberdeen Proving Ground, MD, Private Communications, 1989.

Gratias, S., and J. B. G. Monzac. "The Large-Scale Nuclear-Blast Simulator of the Gramat Research Center: Concept, Research, Performance." Proceedings of the Seventh International Symposium on the Military Application of Blast Simulation (MABS-7), vol. 1, paper no. 1.1, Medicine Hat, Alberta, Canada, 13-17 July 1981.

Hisley, D. M., and G. A. Molvik. "Axisymmetric Calculations for the Large Blast/Thermal Simulator (LB/TS) Shock Tube Configuration." BRL-TR-2935, U.S. Army Ballistic Research Laboratory, Aberdeen Proving Ground, MD, September 1988.

Mark, A., K. O. Opalka, C. W. Kitchens, G. A. Coulter, G. Bulmash and C. N. Kingery. "Simulation of Nuclear Blasts with Large-Scale Shock Tubes." Proceedings of the Eighth International Symposium on Military Applications of Blast Simulation (MABS-8), Spiez, Switzerland, 20-24 June 1983.

Opalka, K. O. "Large Blast and Thermal Simulator Advanced Concept Driver Design by Computational Fluid Dynamics", BRL-TR-3026, U.S. Army Ballistic

Research Laboratory, Aberdeen Proving Ground, MD, August 1989.

Opalka, K. O., and R. J. Pearson. "Advanced Concept Large Blast/Thermal Simulator CFD Design Studies." Computers in Engineering 1989 Conference Proceedings, pp. 189-195, ASME, New York, NY, August 1989.

Opalka, K. O., and R. J. Pearson. "Real Time Flow Control in Large Blast/Thermal Simulators." Proceedings of the 1988 Army Science Conference, Ft. Monroe, Hampton, VA, 25-28 October 1988.

Opalka, K. O. "Large Blast-Wave Simulators (LBS) With Cold-Gas Drivers: Computational Design Studies", BRL-TR-2786, U.S. Army Ballistic Research Laboratory, Aberdeen Proving Ground, MD, March 1987.

Opalka, K. O., and A. Mark. "The BRL-Q1D Code: A Tool for the Numerical Simulation of Flows in Shock Tubes with Variable Cross-Sectional Areas," BRL-TR-2763, U.S. Army Ballistic Research Laboratory, Aberdeen Proving Ground, MD, October 1986.

Pearson, R. J. "Large Blast/Thermal Simulation." SAE Technical Paper # 871746, Society of Automotive Engineers, 400 Commonwealth Drive, Warrendale, Pennsylvania, October 1987.

Pearson, R. J., K. O. Opalka, and D. M. Hisley. "Design Studies of Drivers for the US Large Blast/Thermal Simulator," Proceedings of the Ninth International Symposium on Military Applications of Blast Simulation (MABS-9), vol. 1, paper no. I.6, Southend-on-Sea, Essex, England SS3 9XE, September 1985.

Precision Visuals, Inc. "Picsure User's Guide." 6260 Lookout Road, Boulder, CO, December 1986.

Reichenbach, H., and K. O. Opalka. "An Optical Study of the Flow Start-up Process in Four Convergent-Divergent Nozzles." EMI-Report E 3/90, Fraunhofer Gesellschaft, Ernst-Mach-Institut, Freiburg im Breisgau, (West) Germany, March 1990.

Schardin, H. "Das Toeplersche Schlieren Verfahren" (The Toepler Schlieren Method). V.D.I. Forschungsheft 366, 1934.

Schraml, S. J., and R. J. Pearson. "Small Scale Shock Tube Experiments Using a Computer Controlled Active Rarefaction Wave Eliminator." BRL-TR-3149, U.S. Army Ballistic Research Laboratory, Aberdeen Proving Ground, MD, September 1990.

(intentionally left blank)

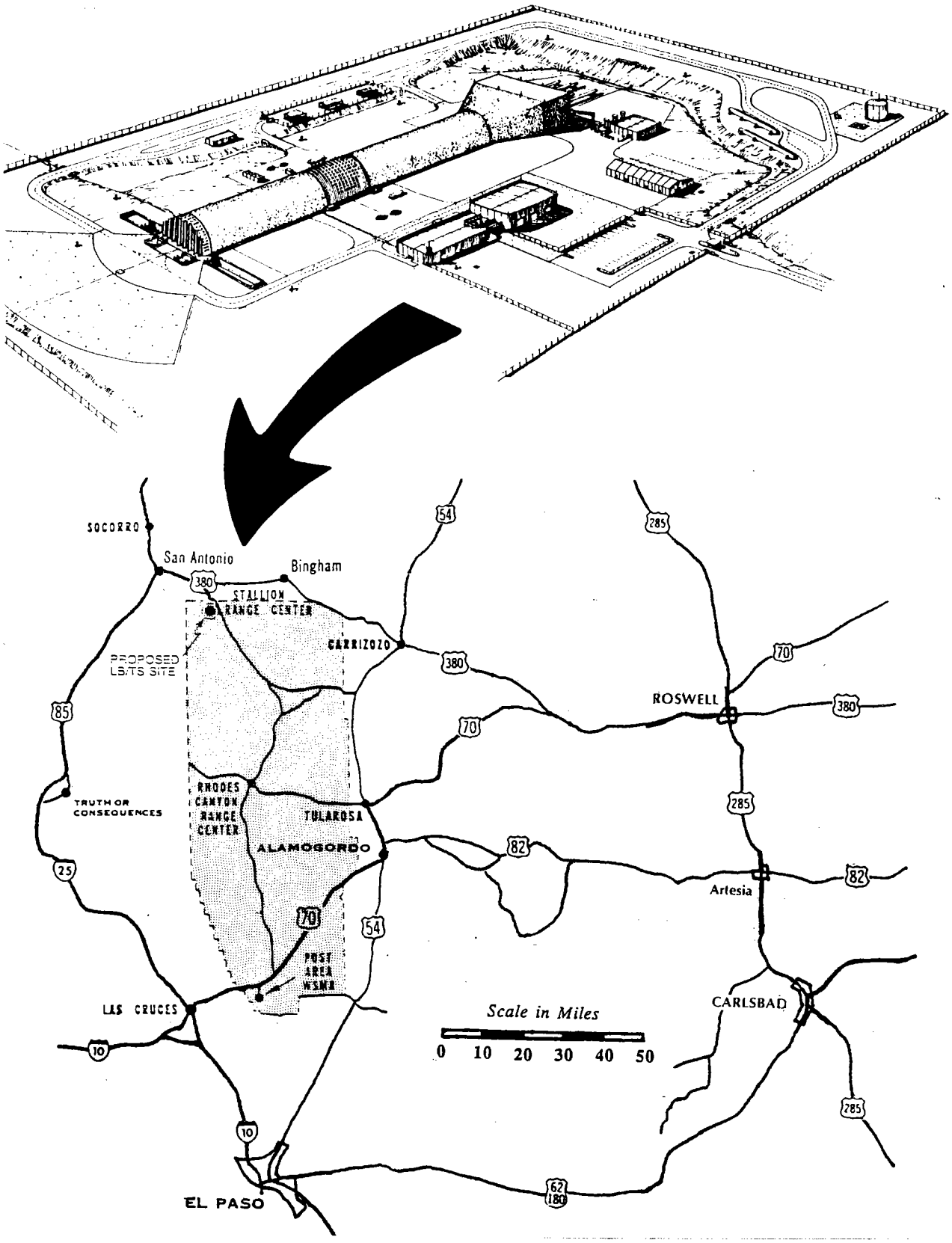

Figure 1: The Planned U. S. LB/TS Facility.

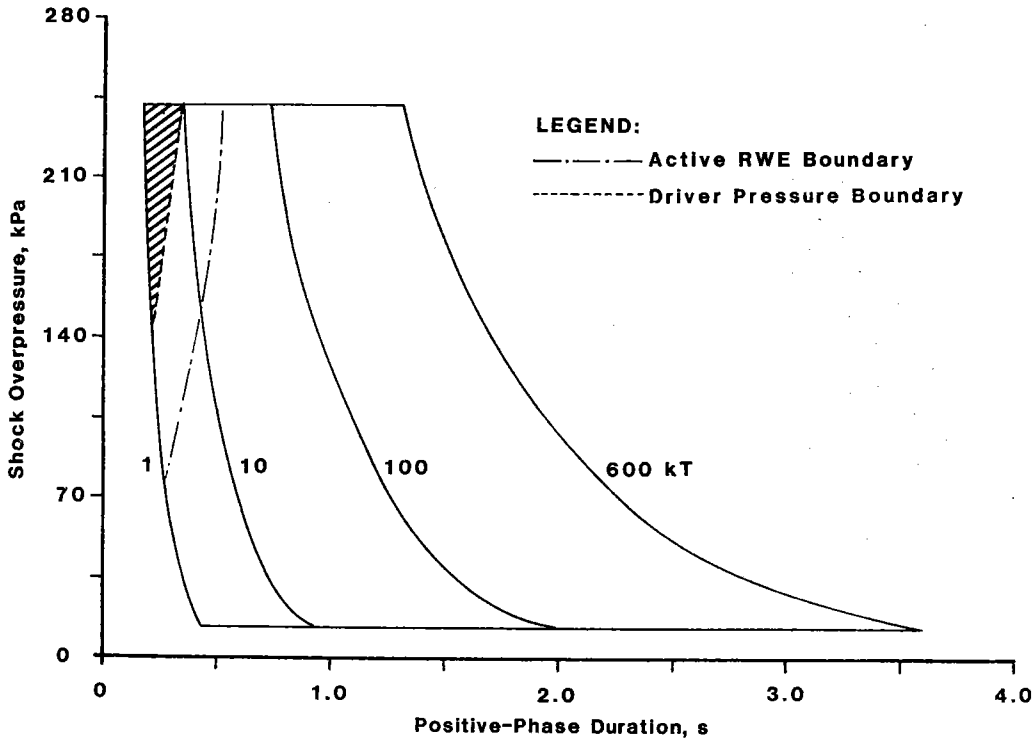

(a) Based on Positive Phase Duration

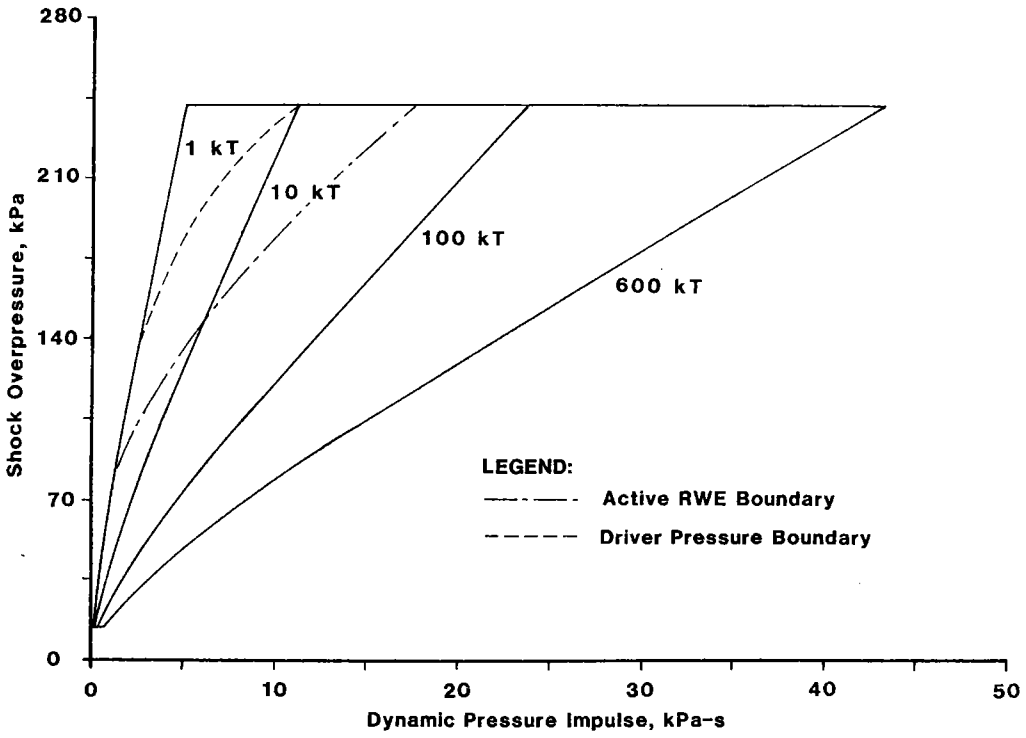

(b) Based on Dynamic Pressure Impulse

Figure 2: The U. S. LB/TS Design Envelope (Source: USA-HDL).

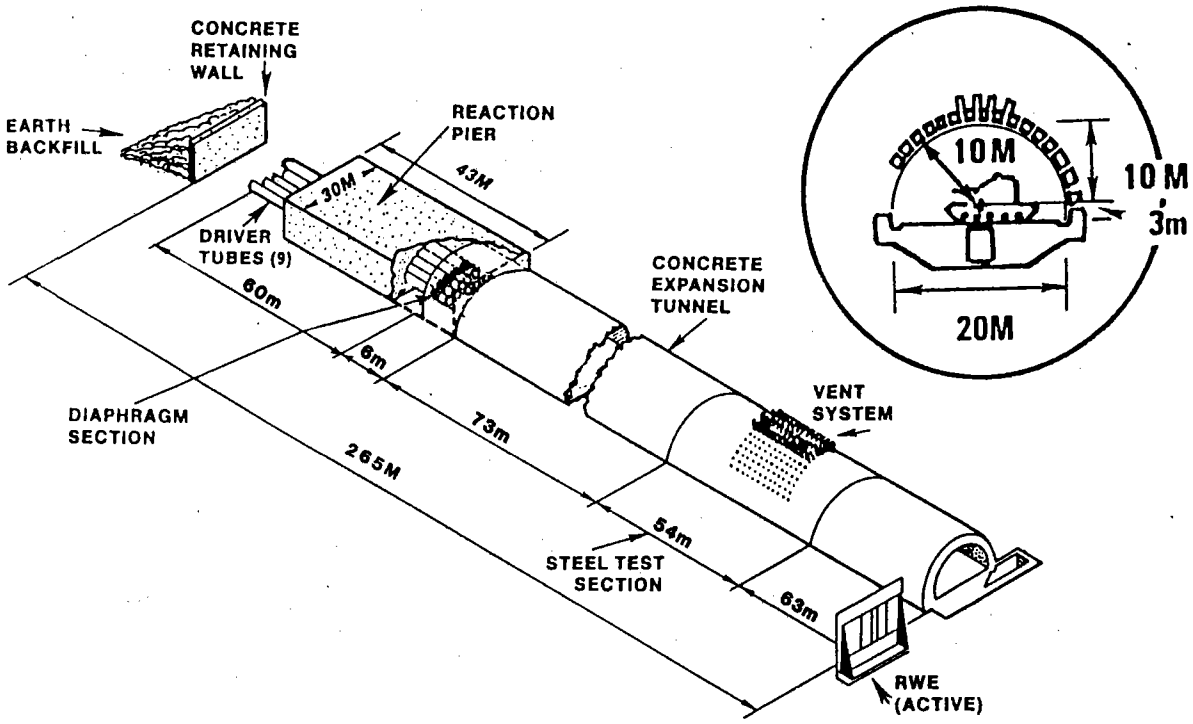

(a) Layout of the Facility

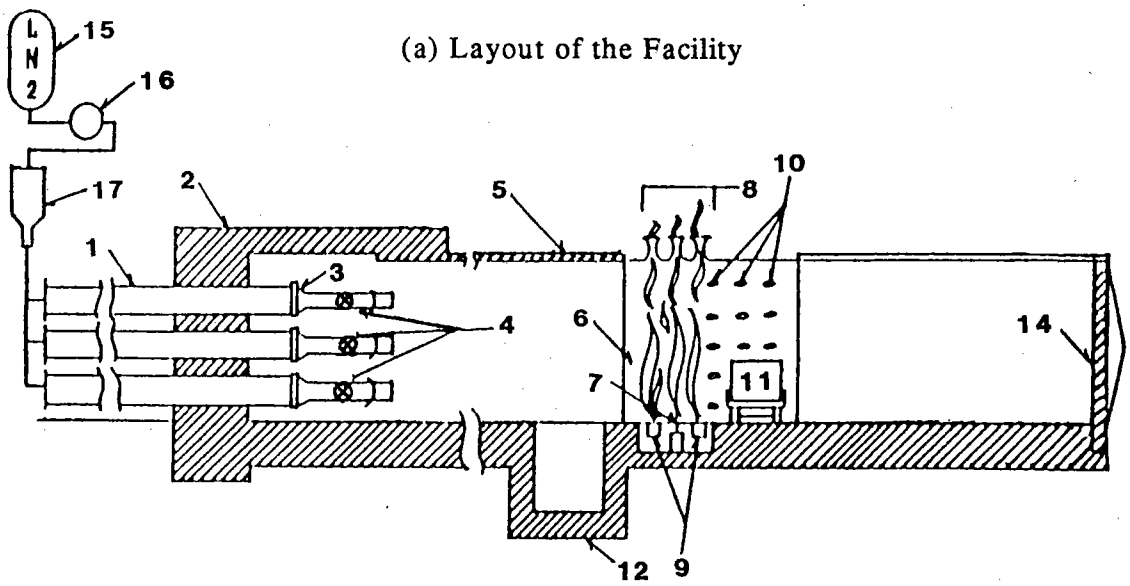

LEGEND

1 - Steel Driver Tubes
2 - Concrete Reaction Pier
3 - Converging Nozzles
4 - Diaphragms (or Throat Valves)
5 - Concrete Expansion Tunnel
6 - Steel Test Section
7 - Thermal Radiation Sources
8 - Combustion Products Ejectors
9 - Air Curtain Plenum
10 - Instrumentation and Light Ports
11 - Test Target
12 - Soil Tank (eliminated)
14 - Rarefaction Wave Eliminator
15 - Liquid Nitrogen Storage
16 - Cryogenic Pumps
17 - Pebble-Bed Superheaters

(b) The BRL LB/TS Concept

Figure 3: Large Blast/Thermal Simulator Design Concept.

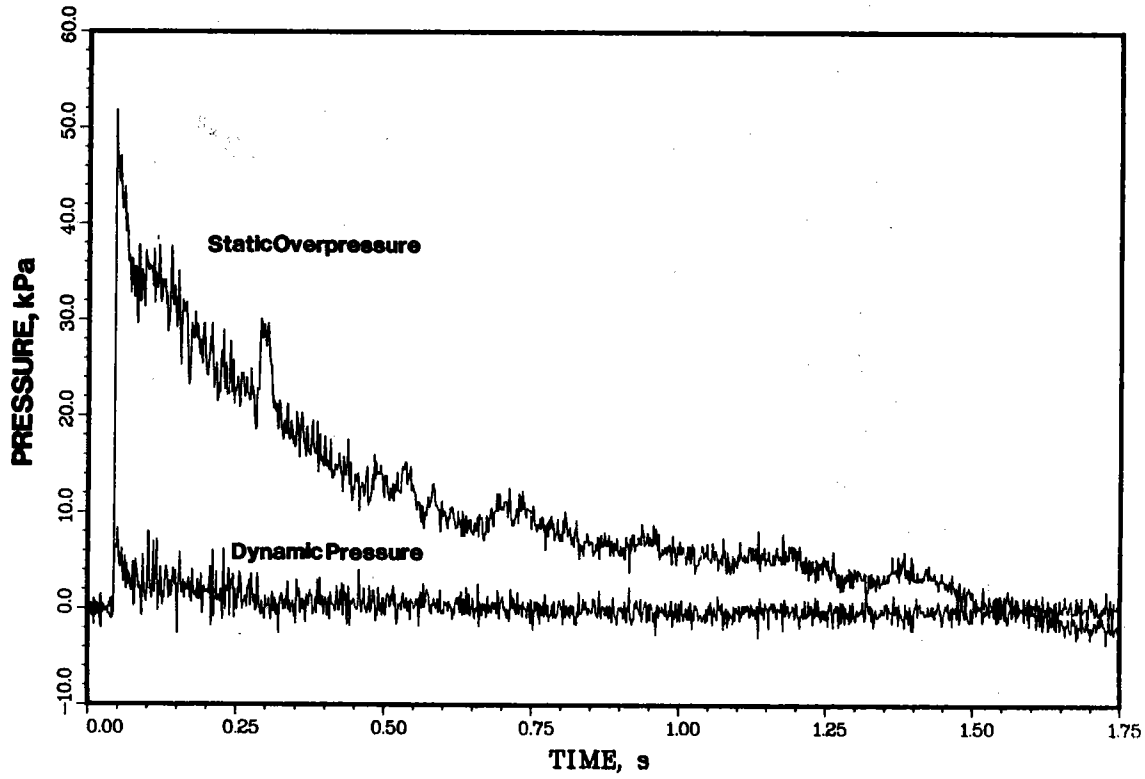

(a) Experimental Record (CEG-LBS)

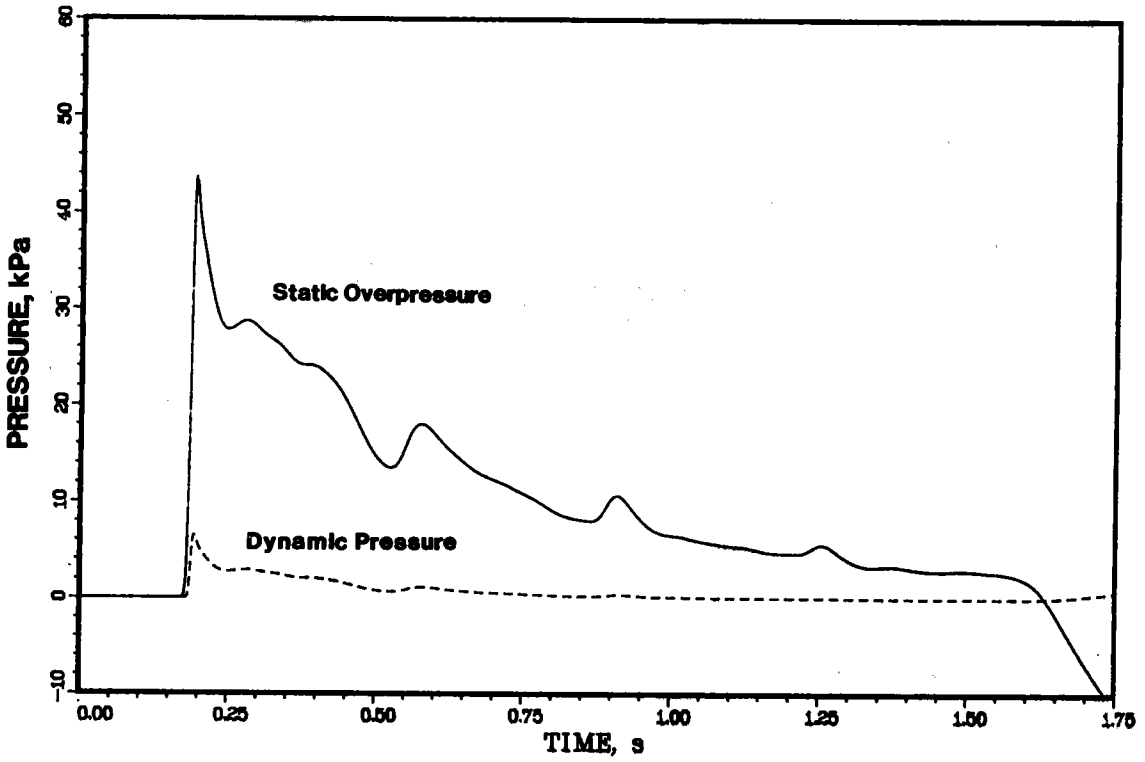

(b) Computational Record (BRL-Q1D)

Figure 4: Experimental and Computational Pressure History for a 42 kPa/10 kT Blast Wave.

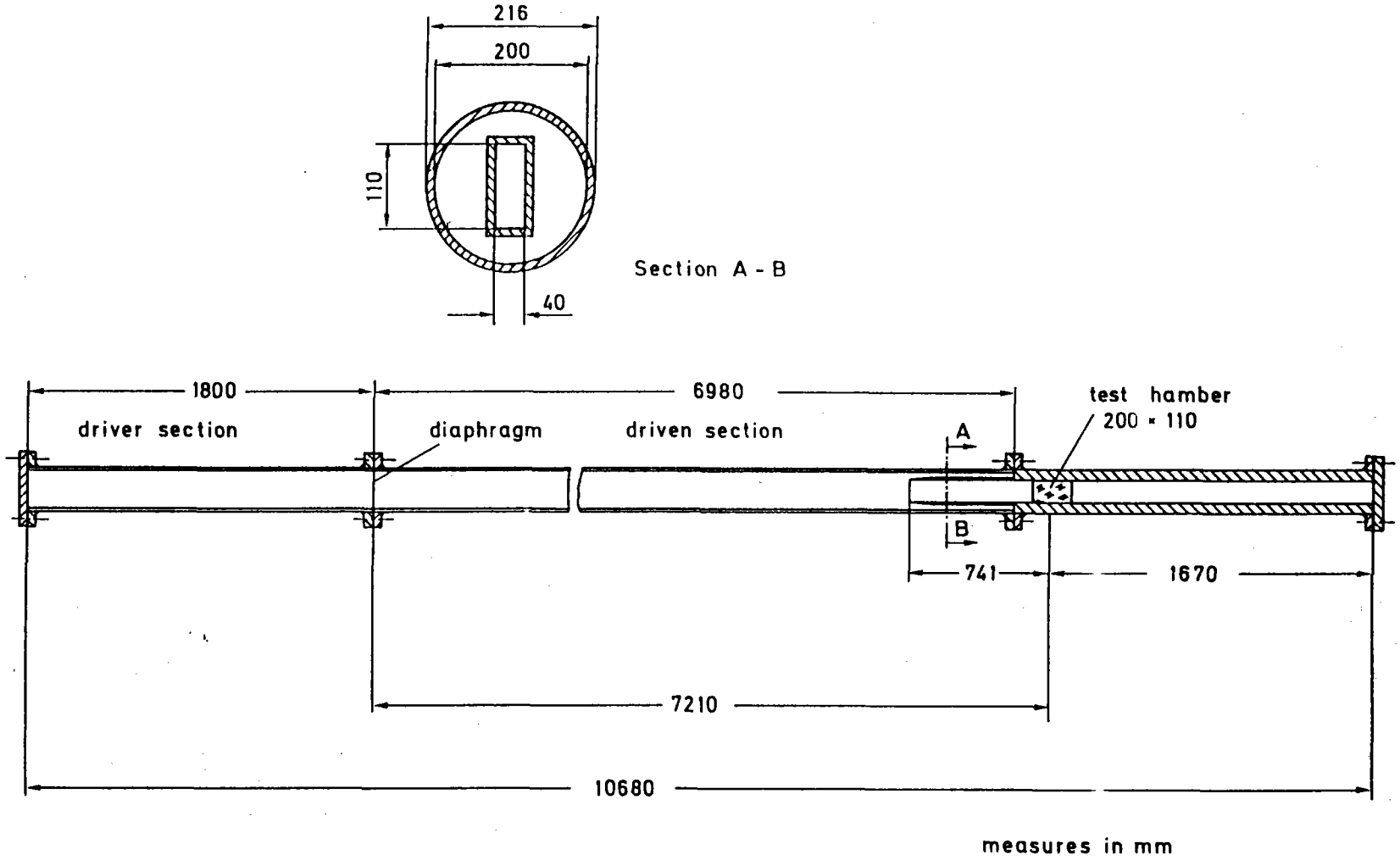

Figure 5: EMI 200mm Shock Tube.

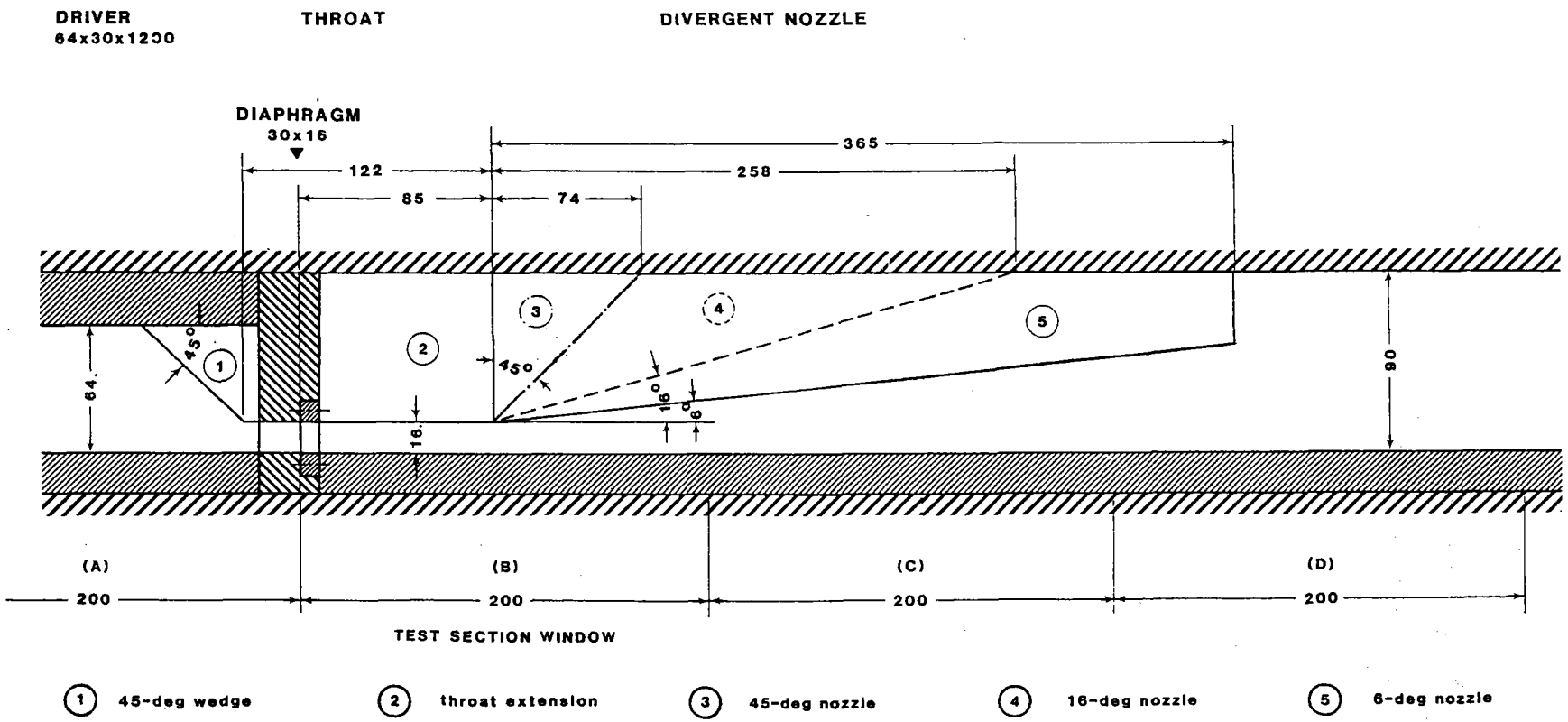

2D EMI HALF NOZZLE

All Dimensions in mm

SCALE 1:2

KOO - Dec 15, 1988

(a) Model Layout

Figure 6: EMI Planar Driver and Nozzle Design.

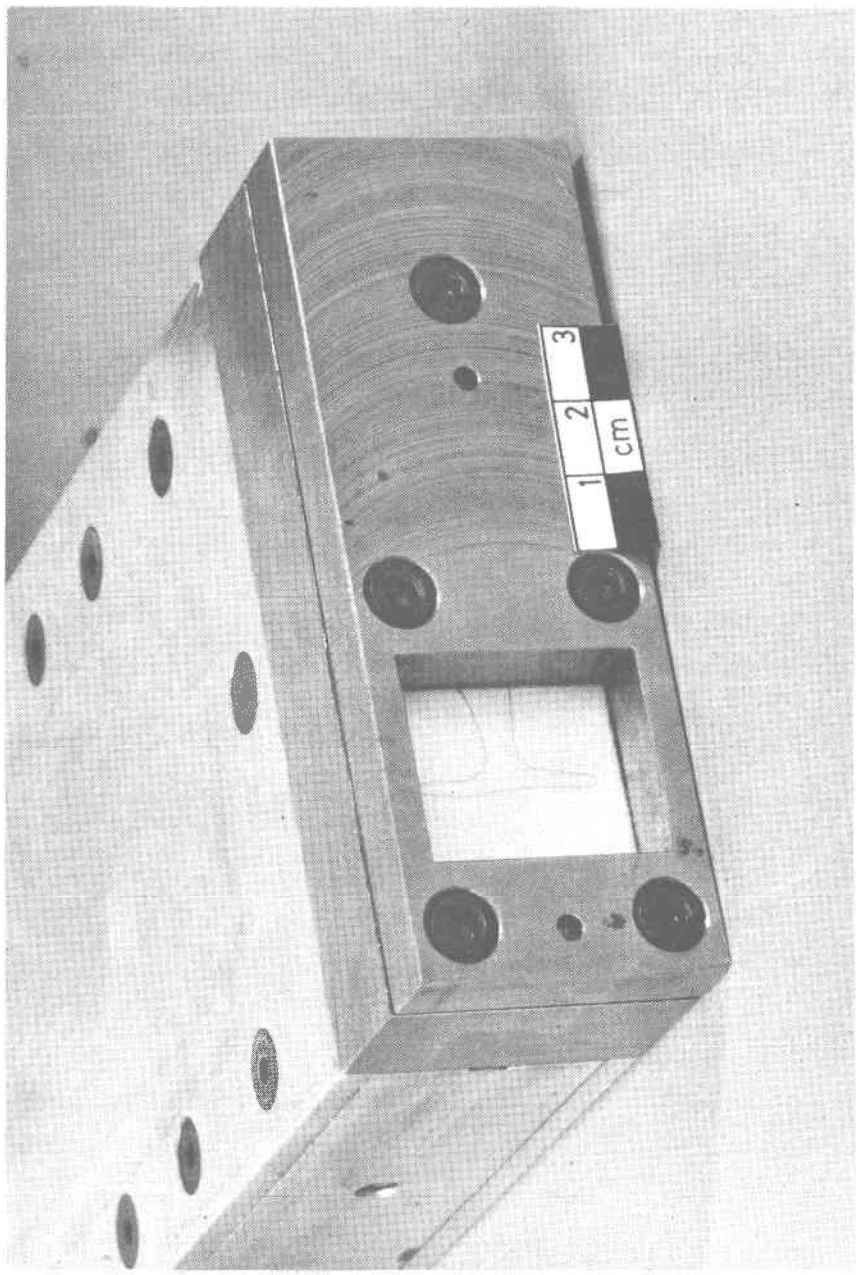

(b) Diaphragm Section

Figure 6: (concluded)

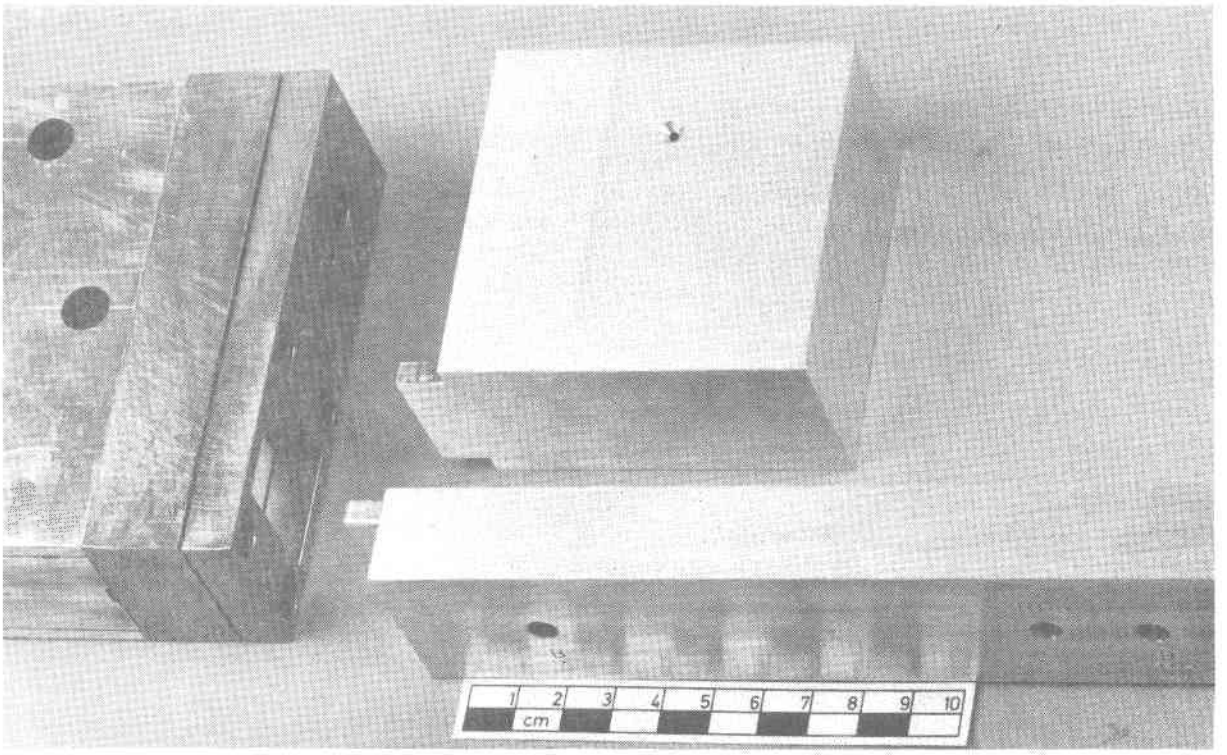

(a) 90° Half-Nozzle

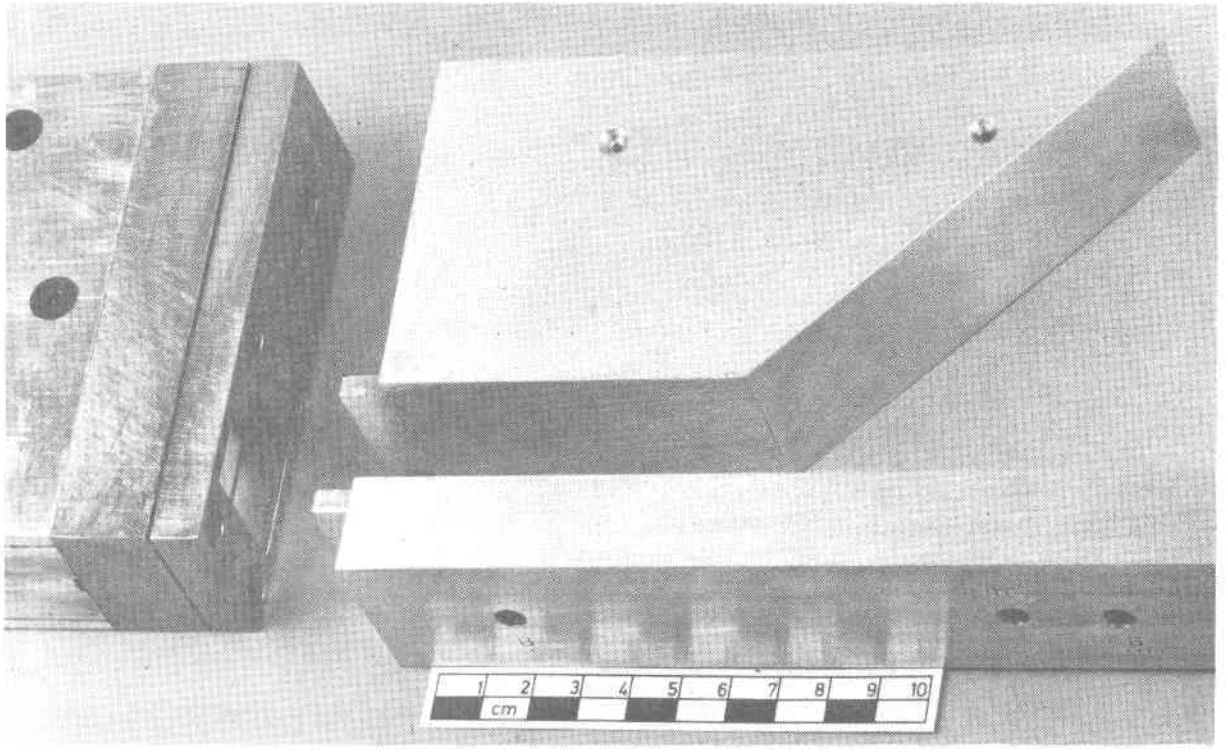

(b) 45° Half-Nozzle

Figure 7: Models of the Divergent Nozzle Configurations.

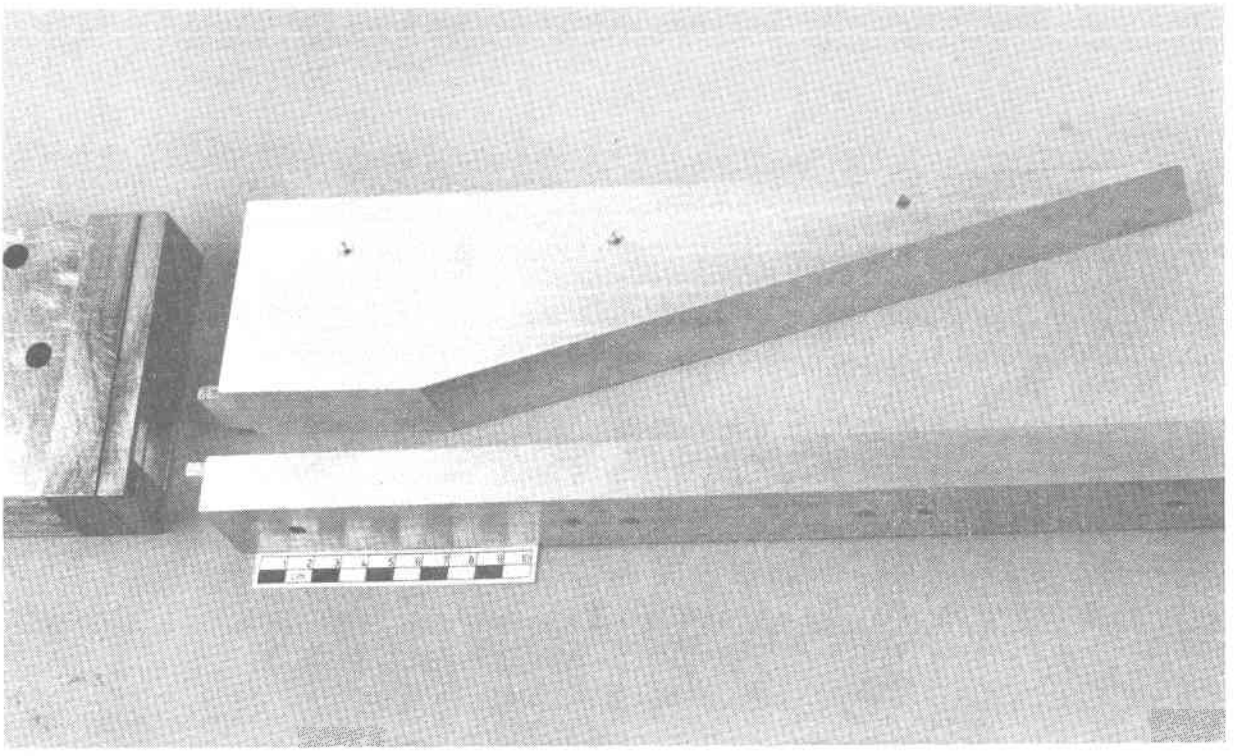

(c) 16° Half-Nozzle

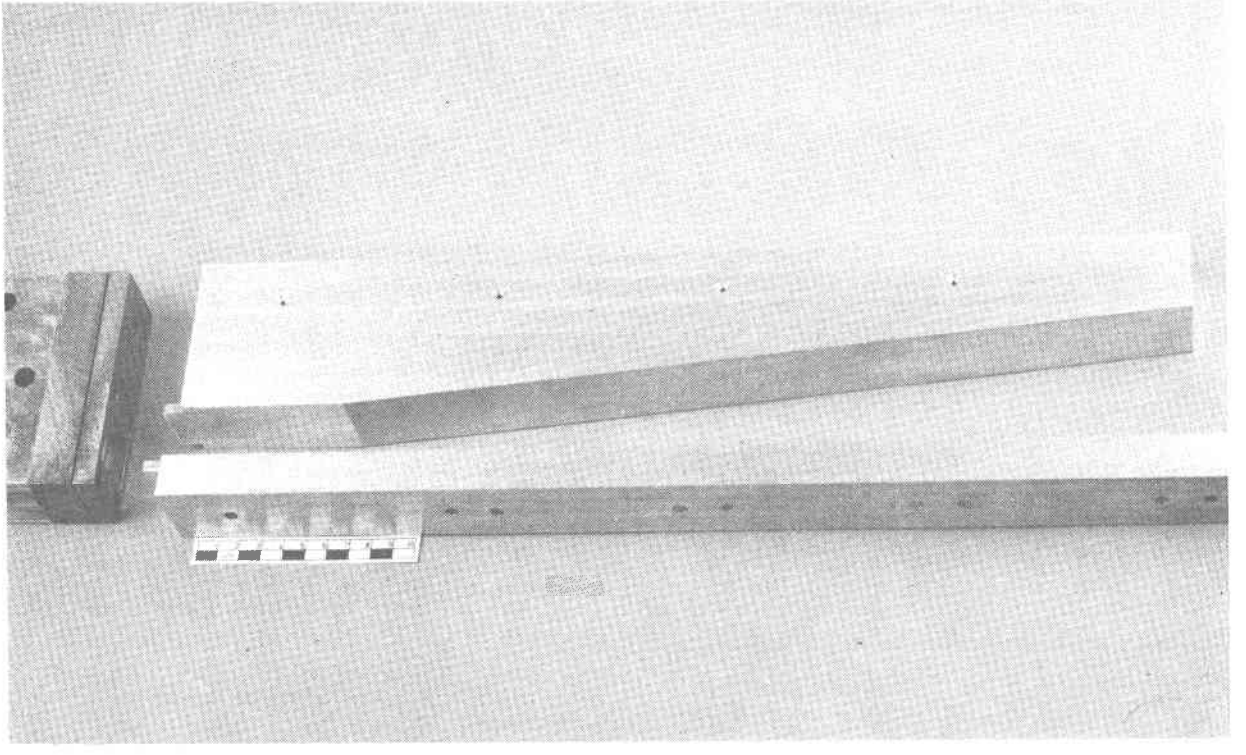

(d) 6° Half-Nozzle

Figure 7: (concluded)

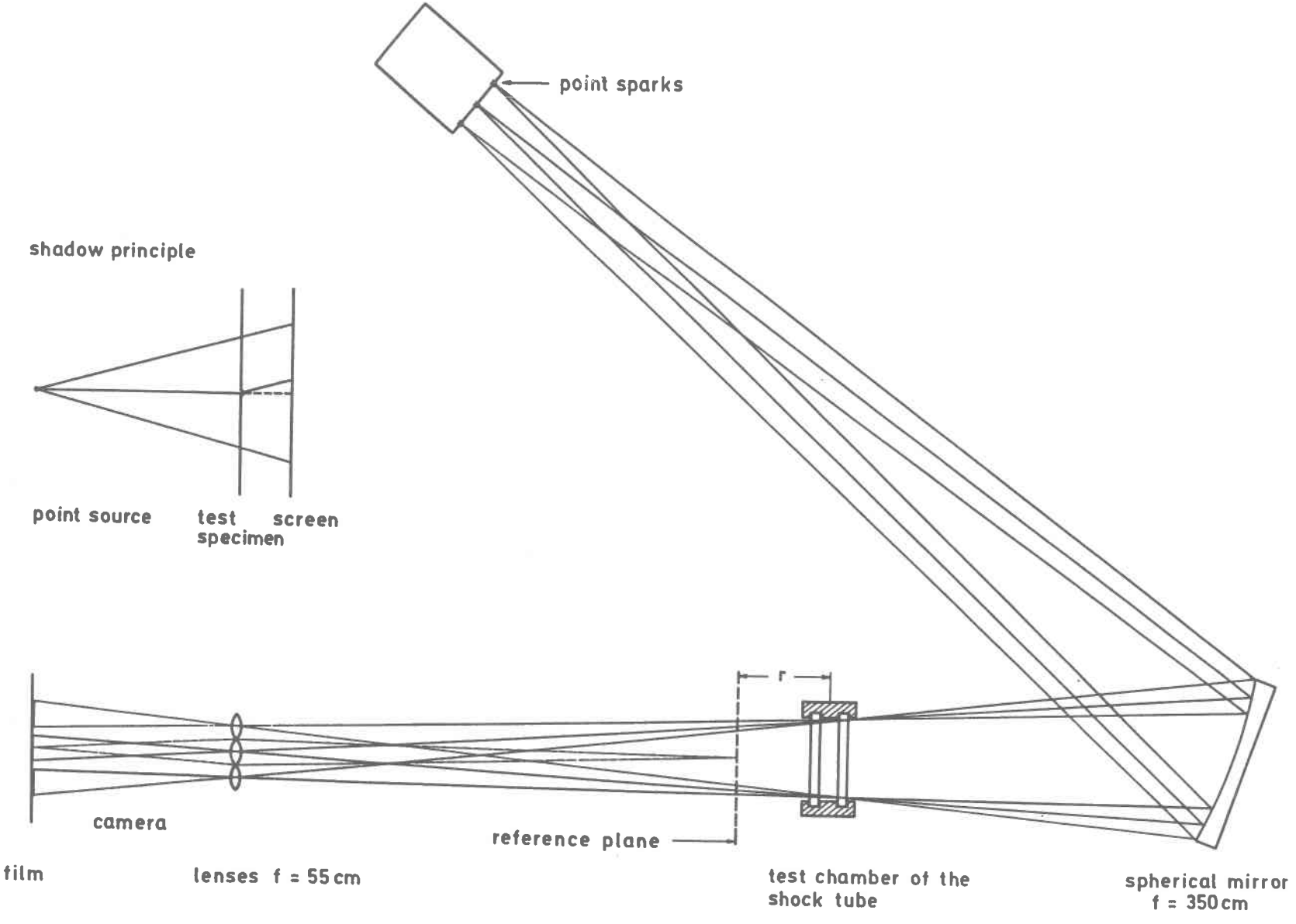

Figure 8: EMI 24-Frame Cranz-Schardin Camera and Shadowgraph Arrangement.

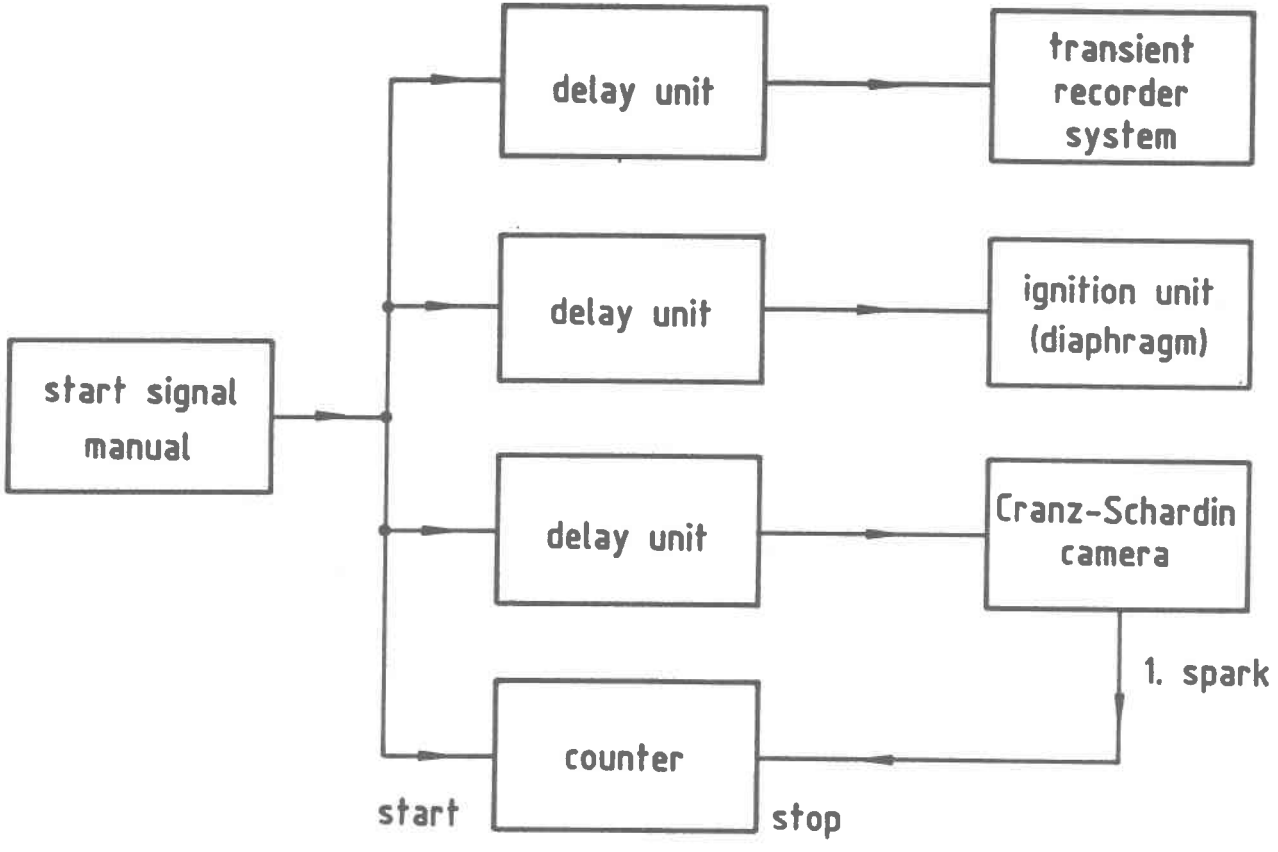

Figure 9: Triggering Circuit (EMI).

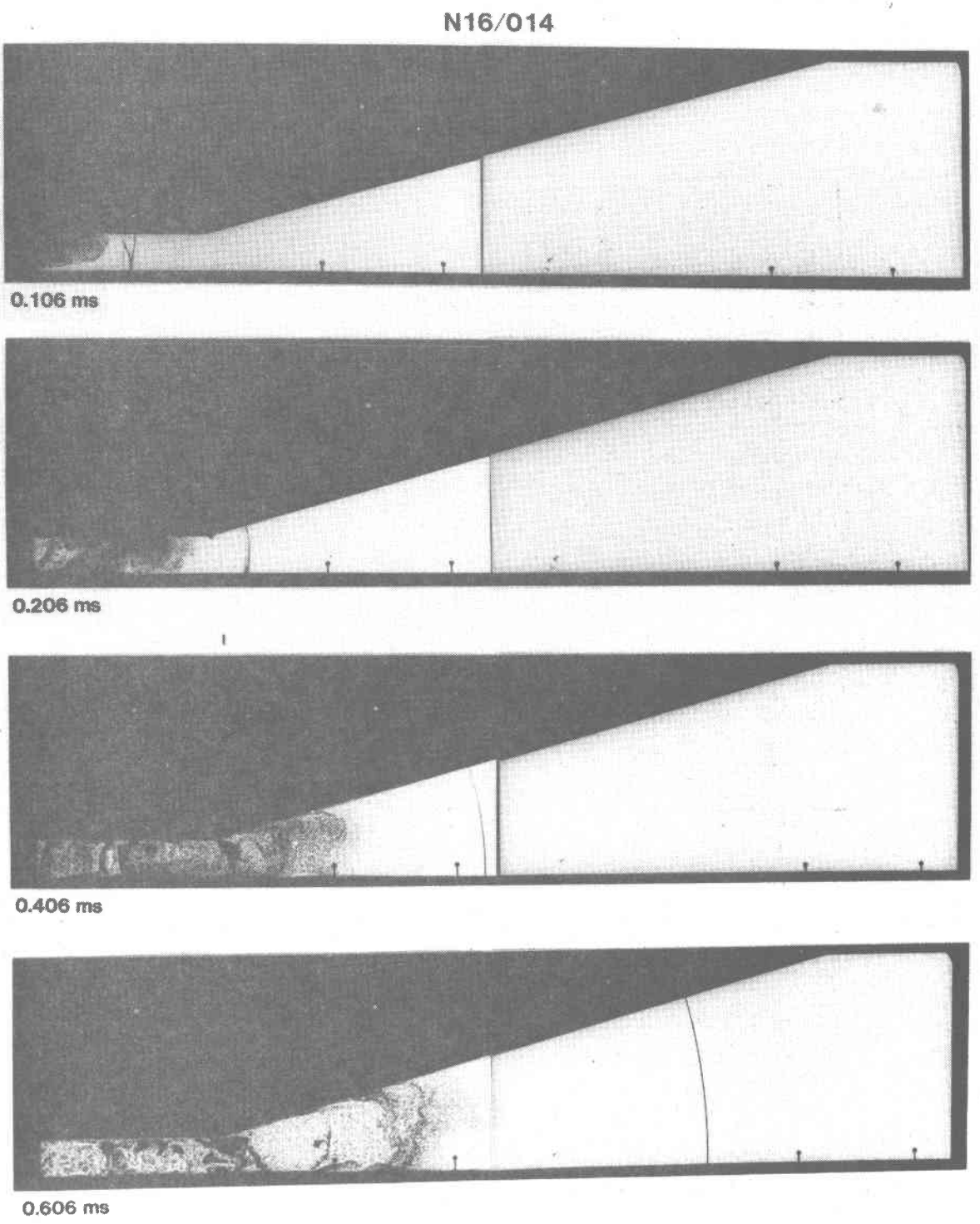

a) Shadowgraph Sequence in Early Phase of Flow Start-up

Figure 10: Flow Start-up Process in the 16° Half-Nozzle at Driver Pressure Ratio $P_{41} = 14$.

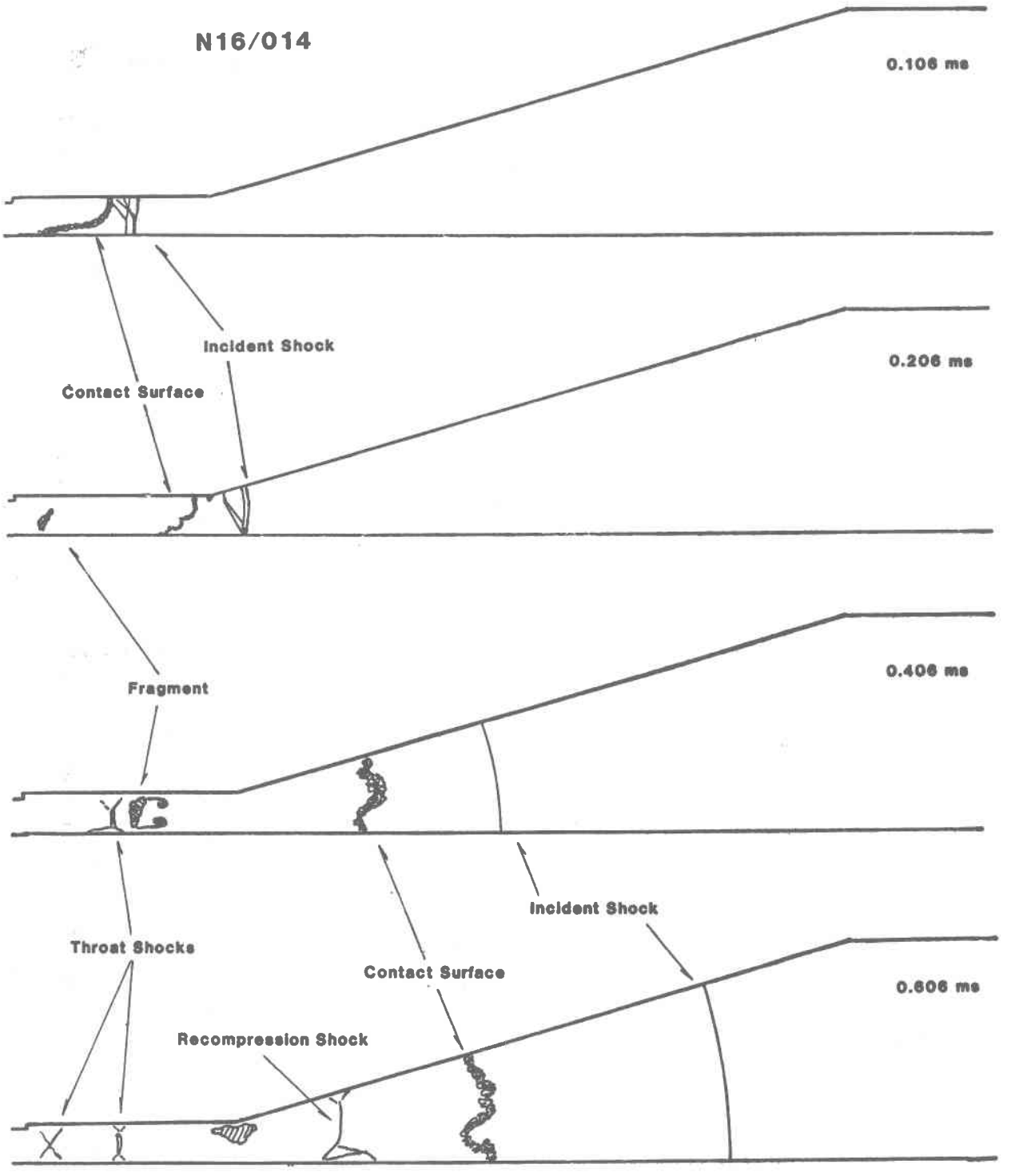

b) Illustration of Major Flow Phenomena in Early Phase

Figure 10: (continued)

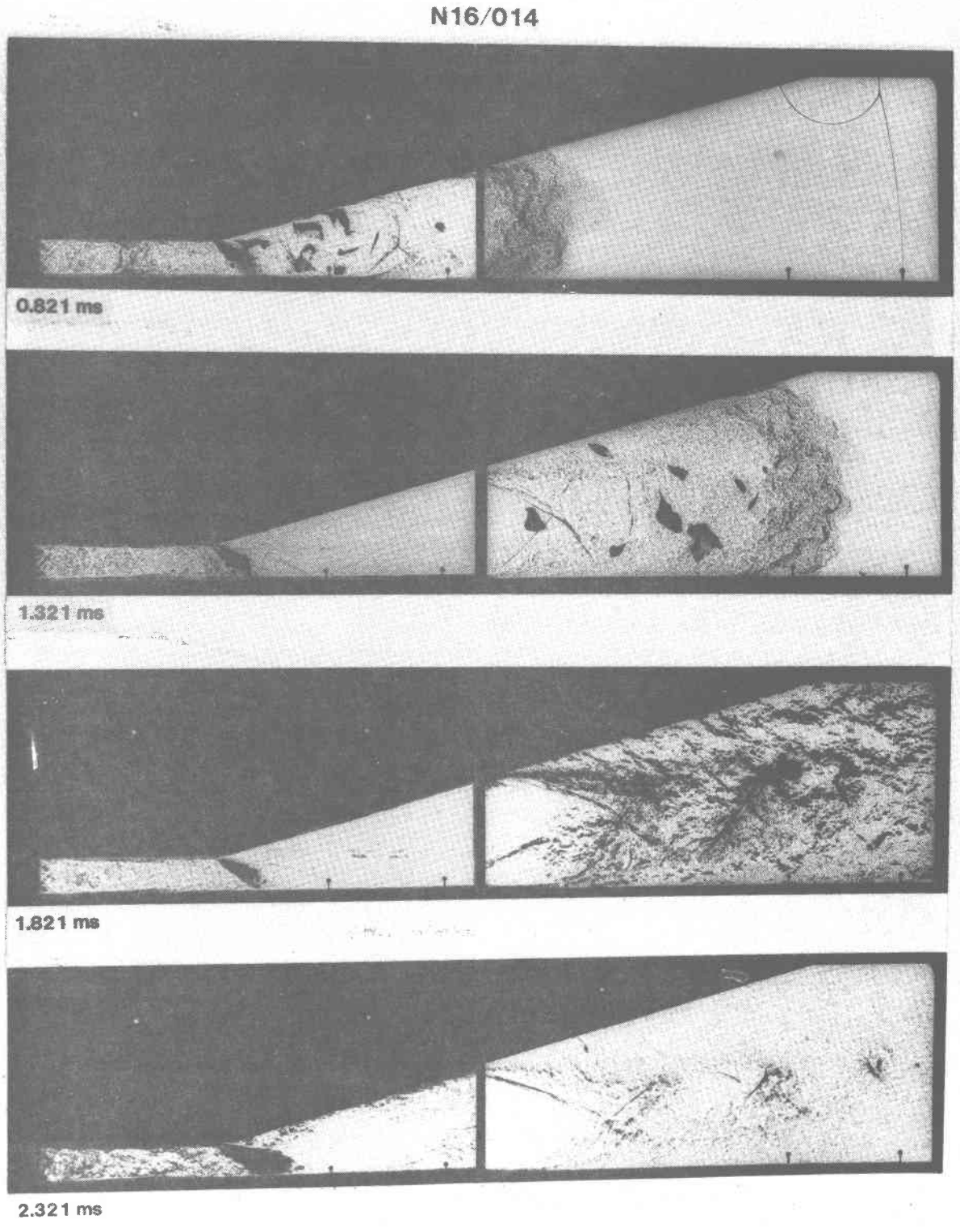

c) Shadowgraph Sequence in Late Phase of Flow Start-up

Figure 10: (continued)

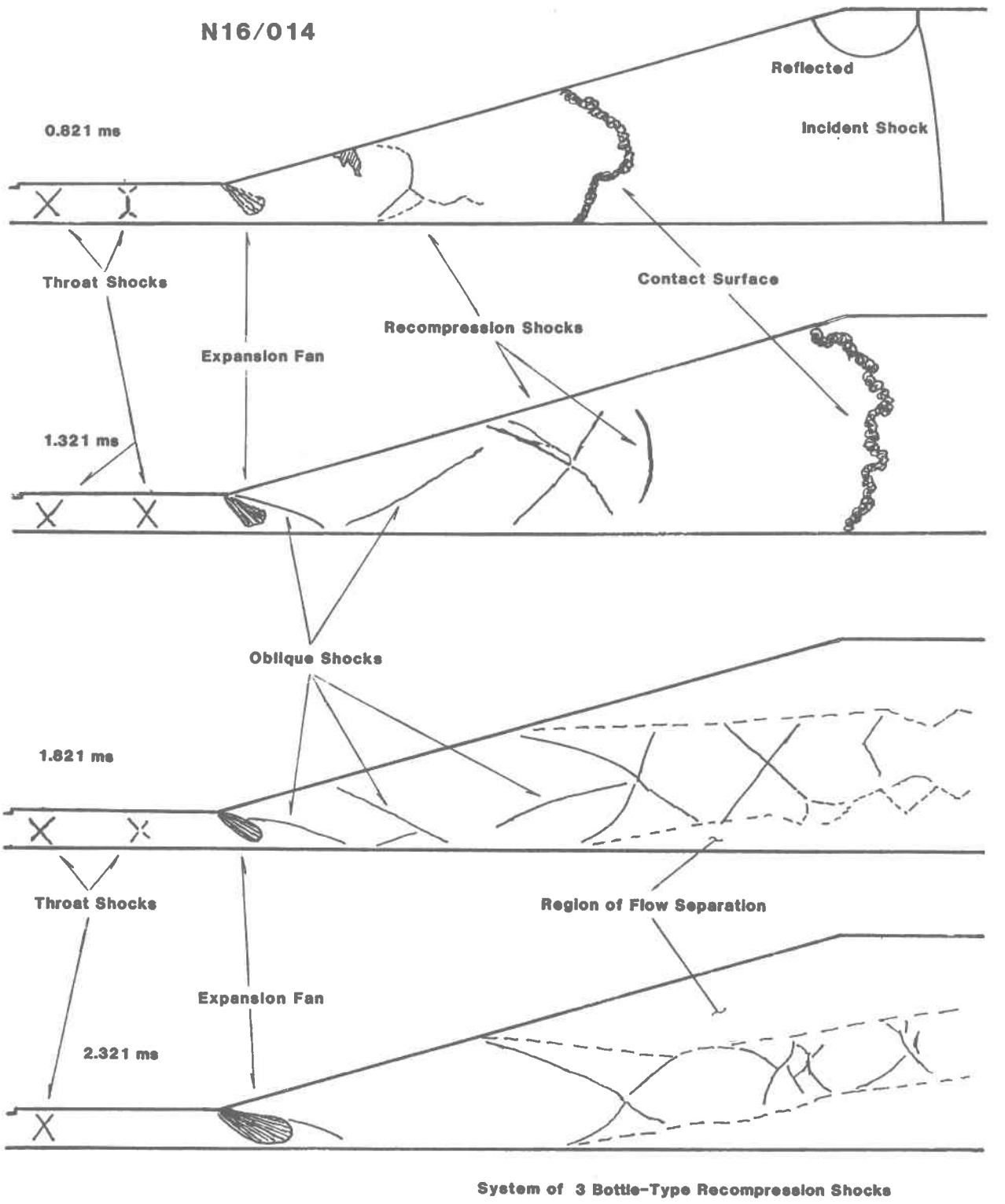

d) Illustration of Major Flow Phenomena in Late Phase

Figure 10: (concluded)

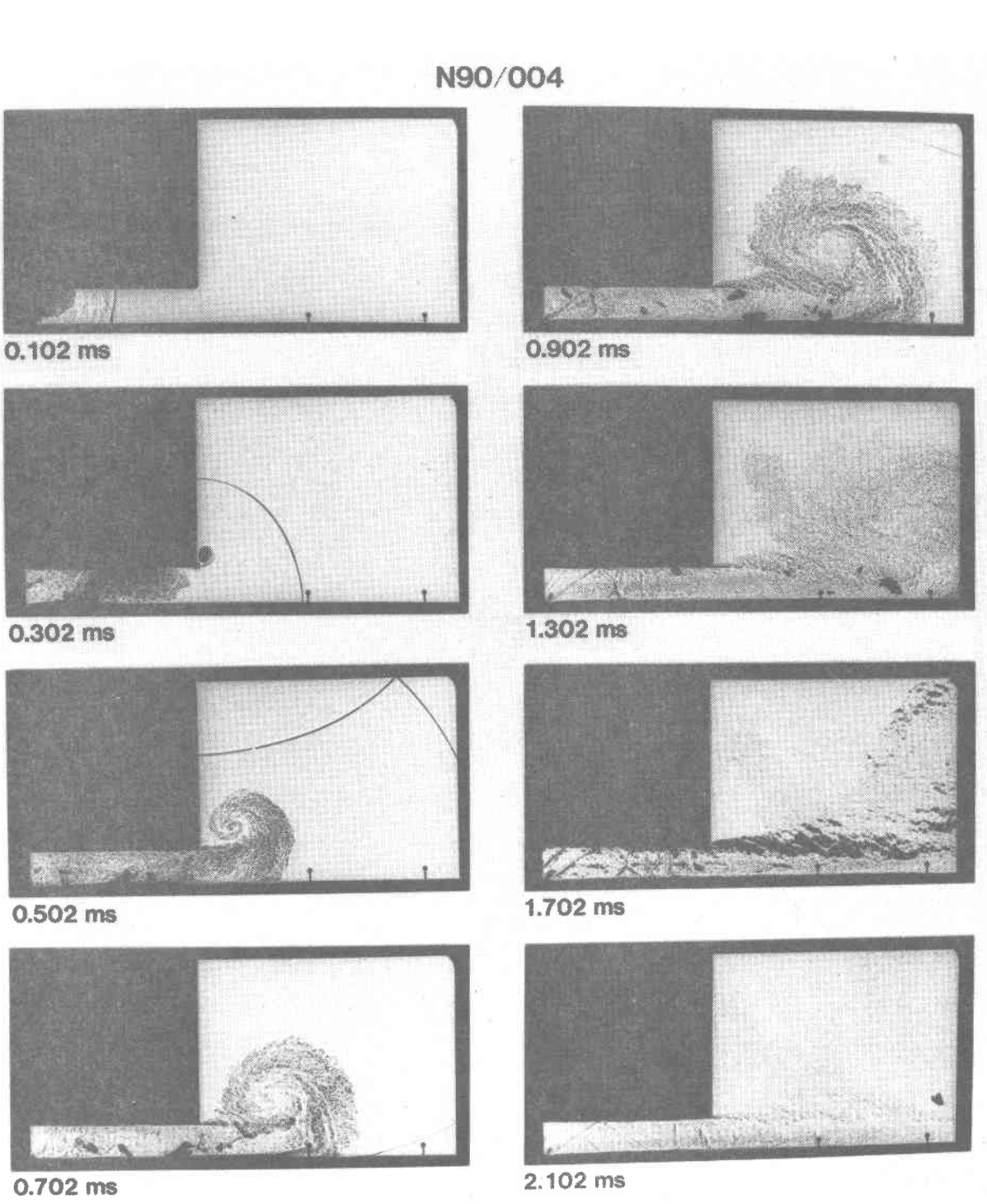

a) Driver Pressure Ratio $P_{41} = 4$

Figure 11: Two Sequences of Selected Shadowgraphs for the 90° Half-Nozzle.

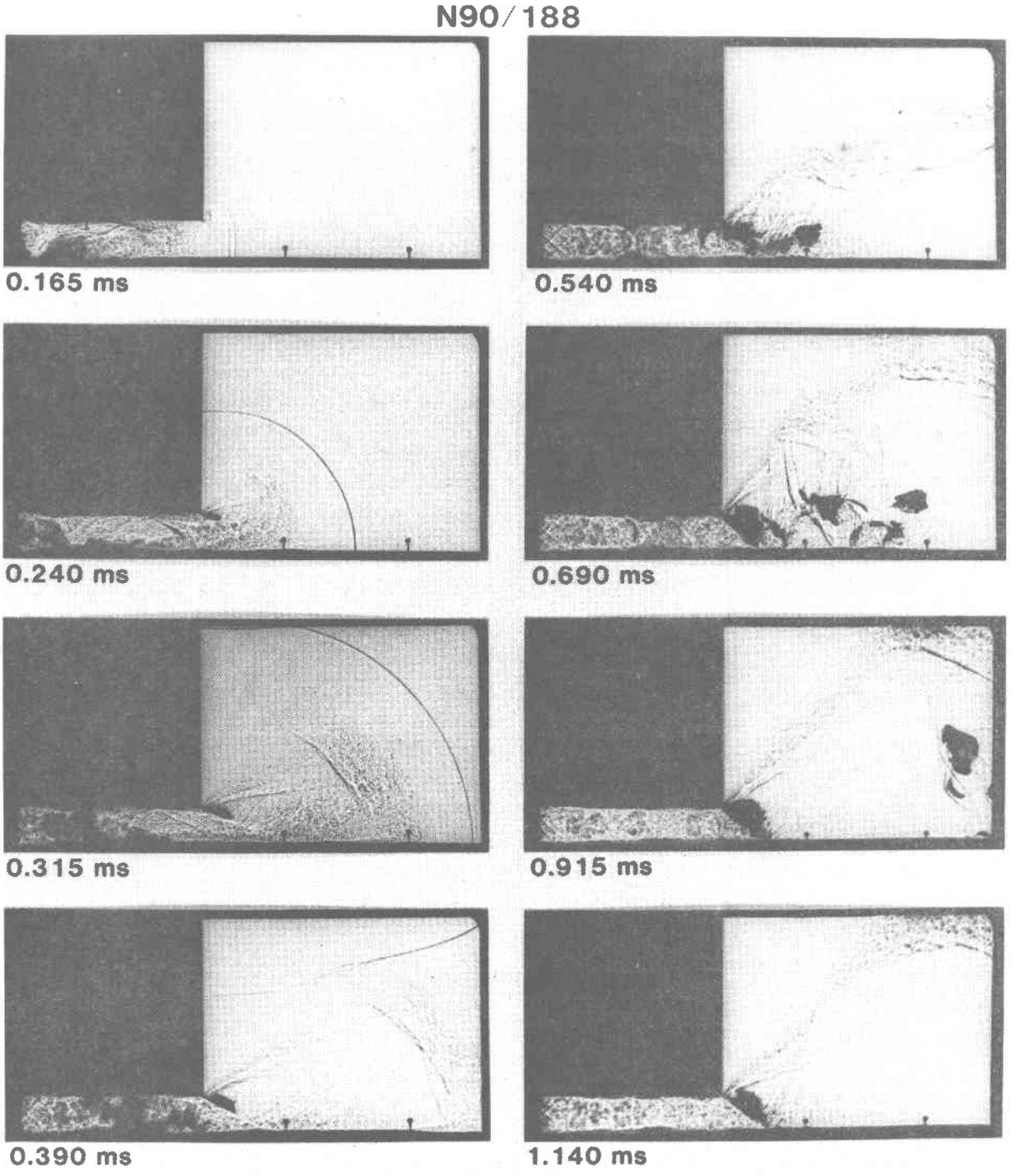

b) Driver Pressure Ratio P_{41} = 188

Figure 11: (concluded)

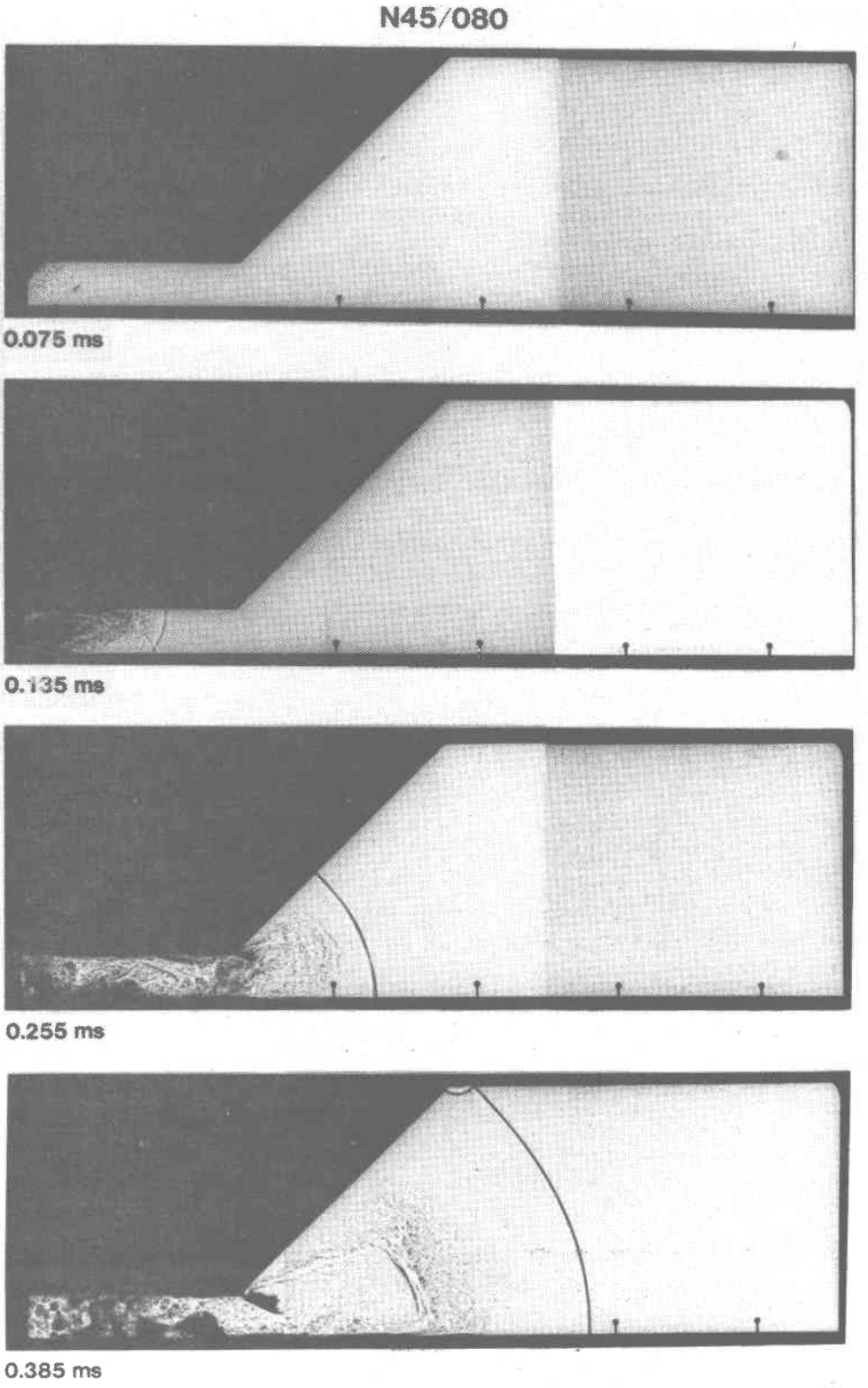

a) Early Phase

Figure 12: Sequence of Selected Shadowgraphs for the 45° Half-Nozzle at Driver Pressure Ratio $P_{41} = 80.$

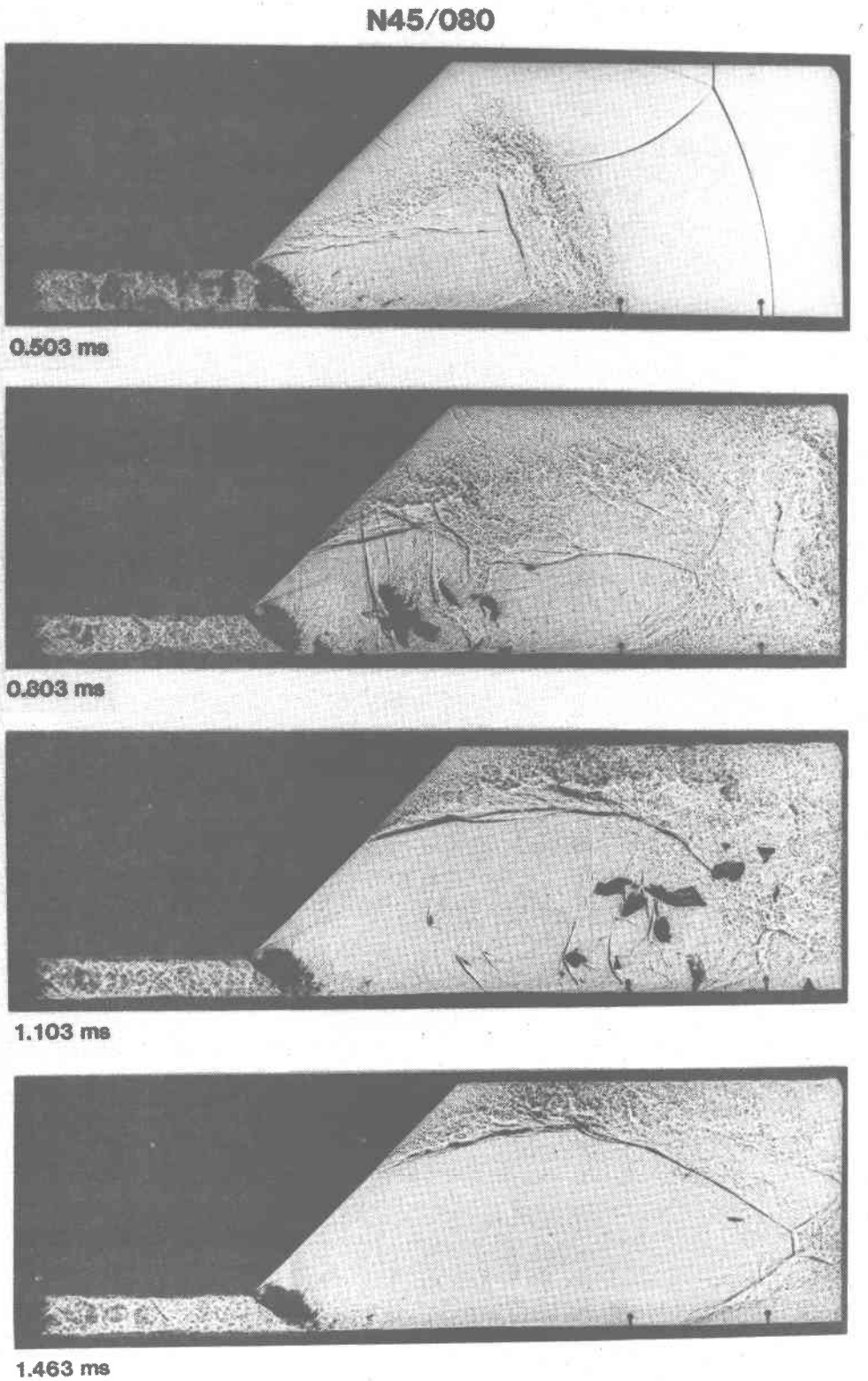

b) Late Phase

Figure 12: (concluded)

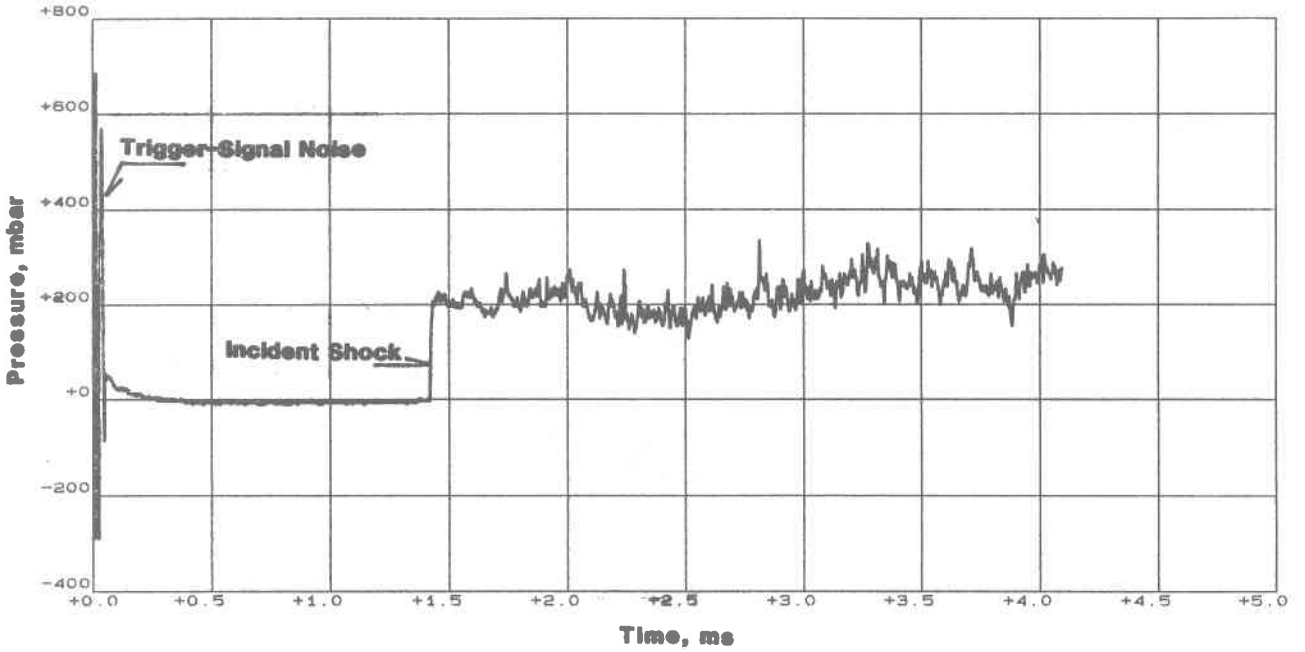

a) Long Time Scale

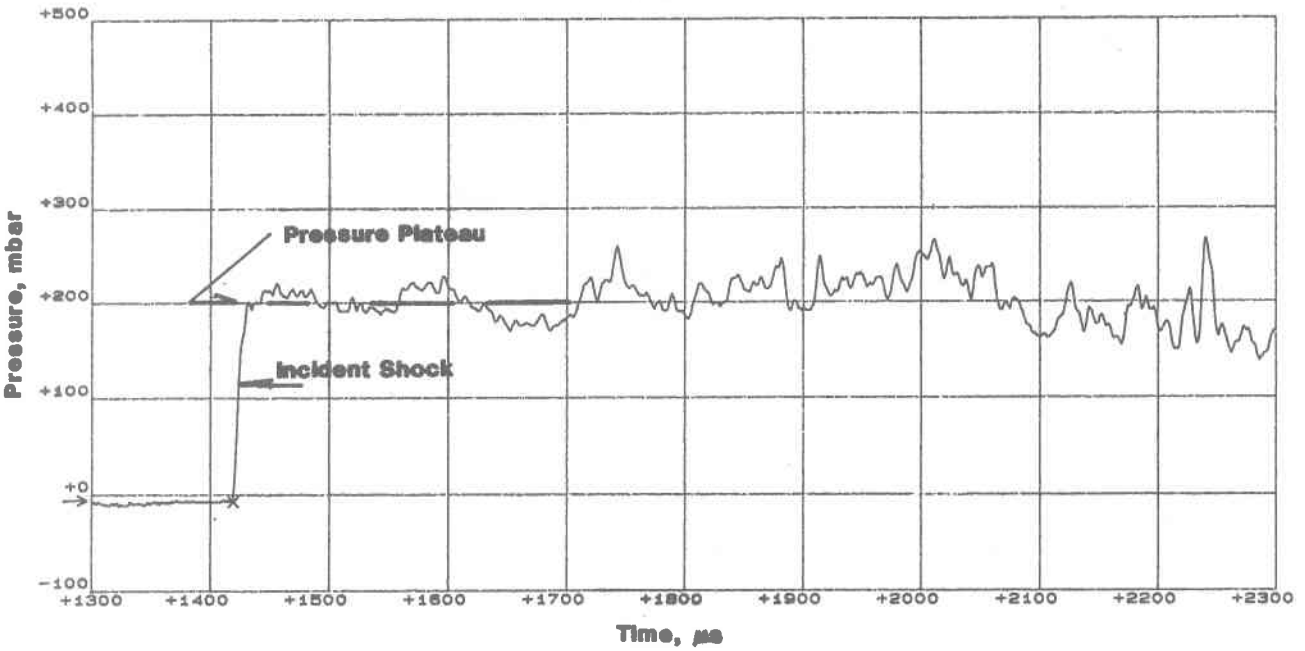

b) Short Time Scale

Figure 13: Static Overpressure History for the 90° Half-Nozzle at Driver Pressure Ratio P_{41} = 188, 860 mm Downstream from the Diaphragm.

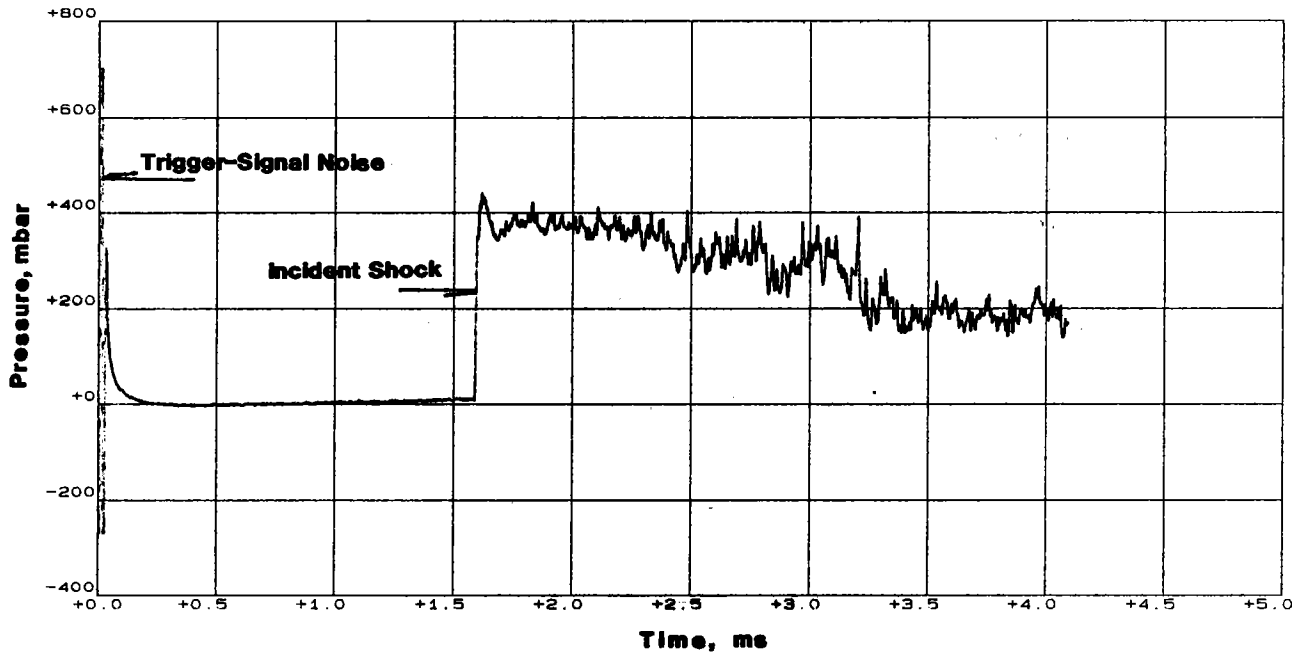

a) Long Time Scale

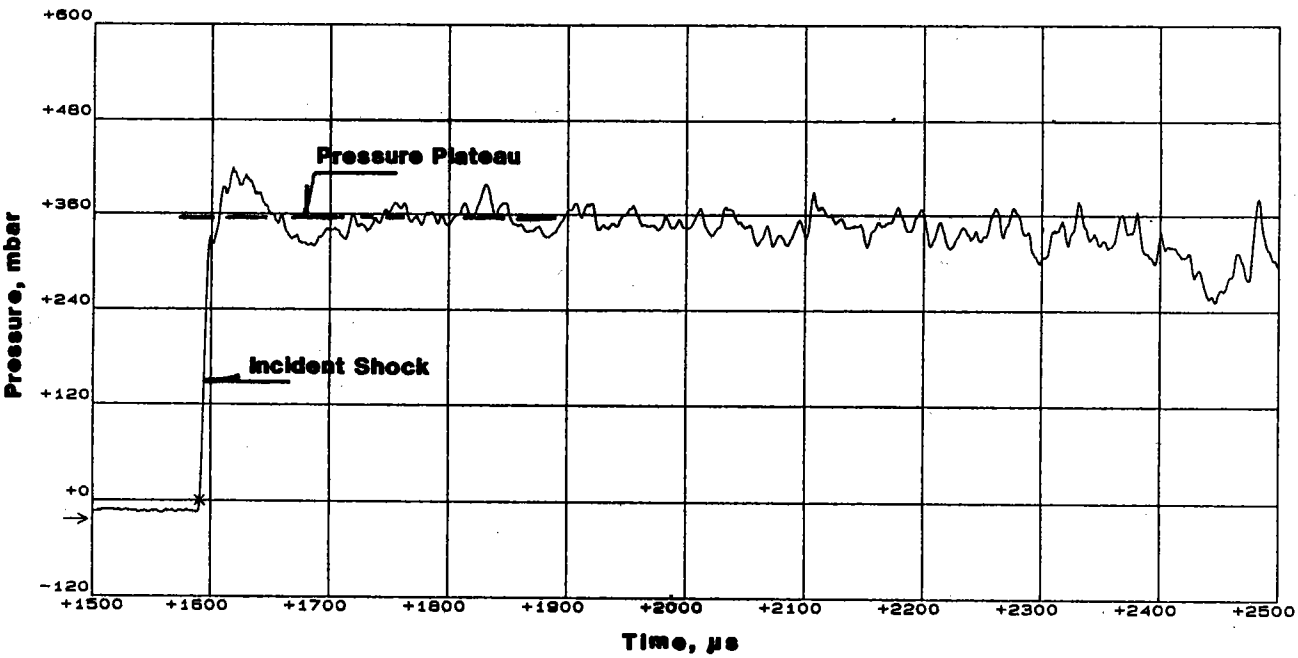

b) Short Time Scale

Figure 14: Static Overpressure History for the 45° Half-Nozzle at Driver Pressure Ratio P_{41} = 80, 860 mm Downstream from the Diaphragm.

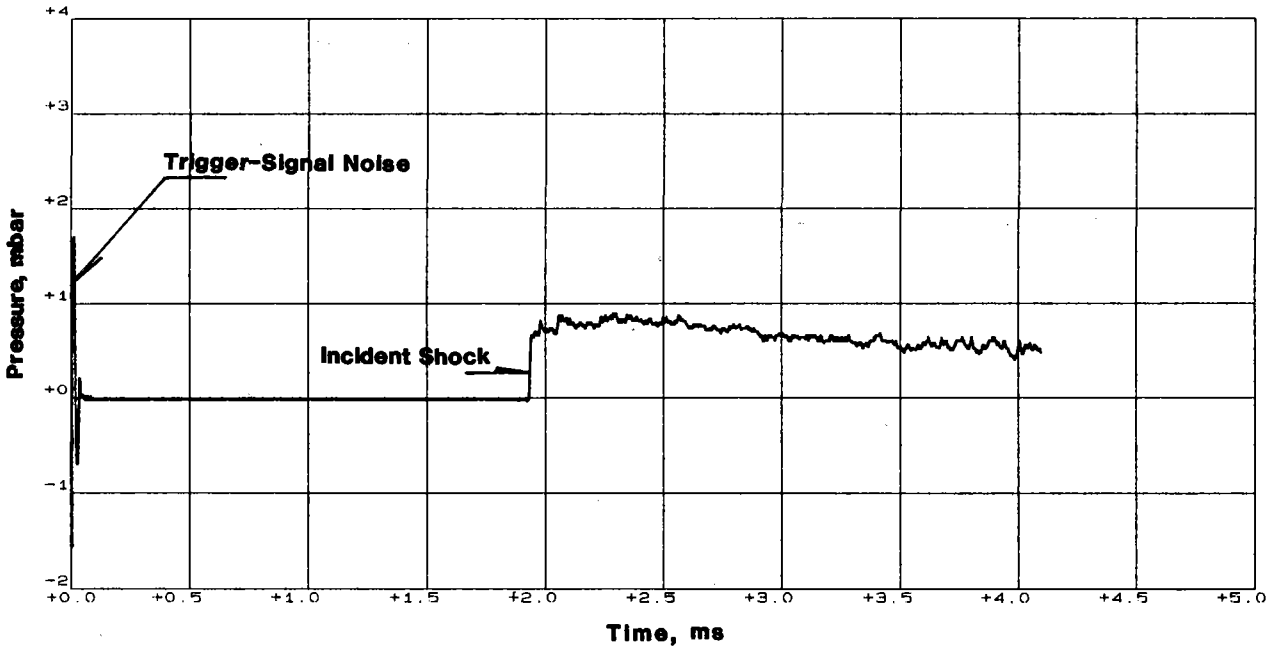

a) Long Time Scale

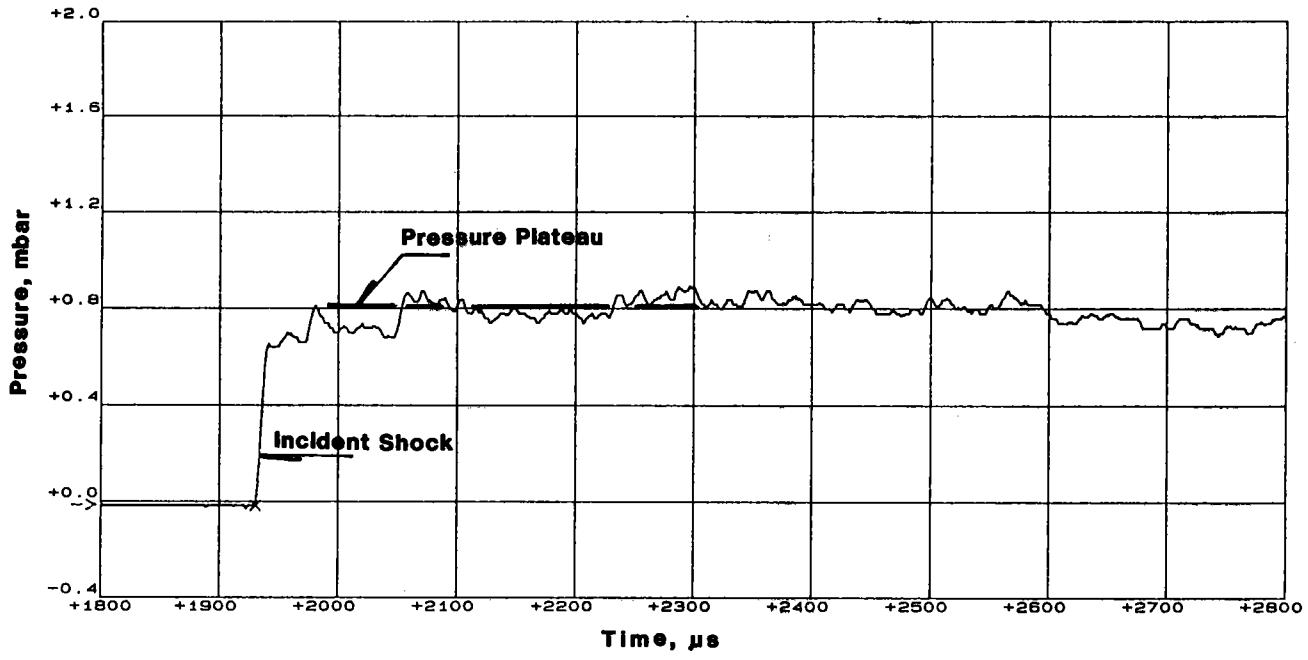

b) Short Time Scale

Figure 15: Static Overpressure History for the 16° Half-Nozzle at Driver Pressure Ratio P_{41} = 14, 860 mm Downstream from the Diaphragm.

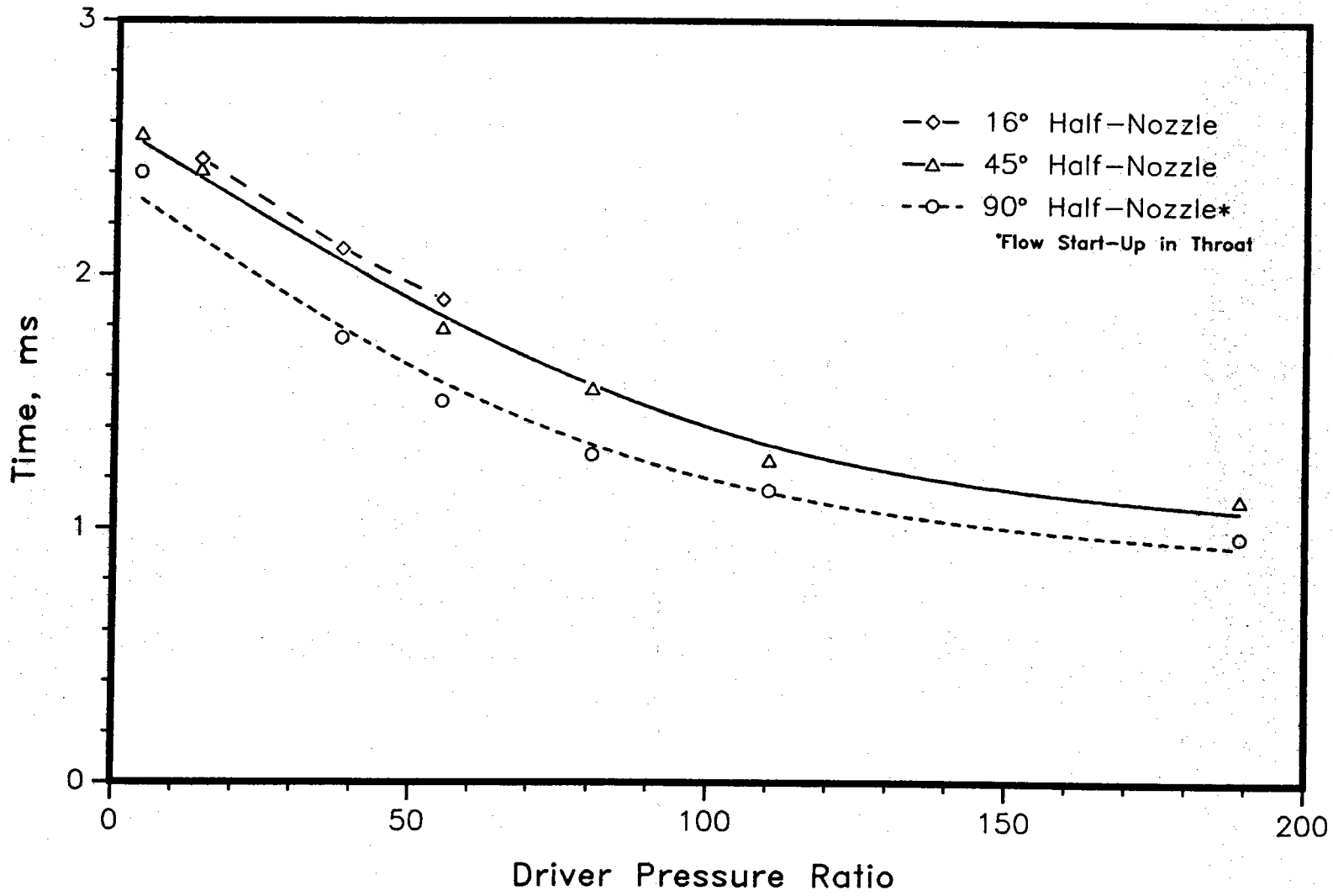

Figure 16: Nozzle Flow Start-up Period.

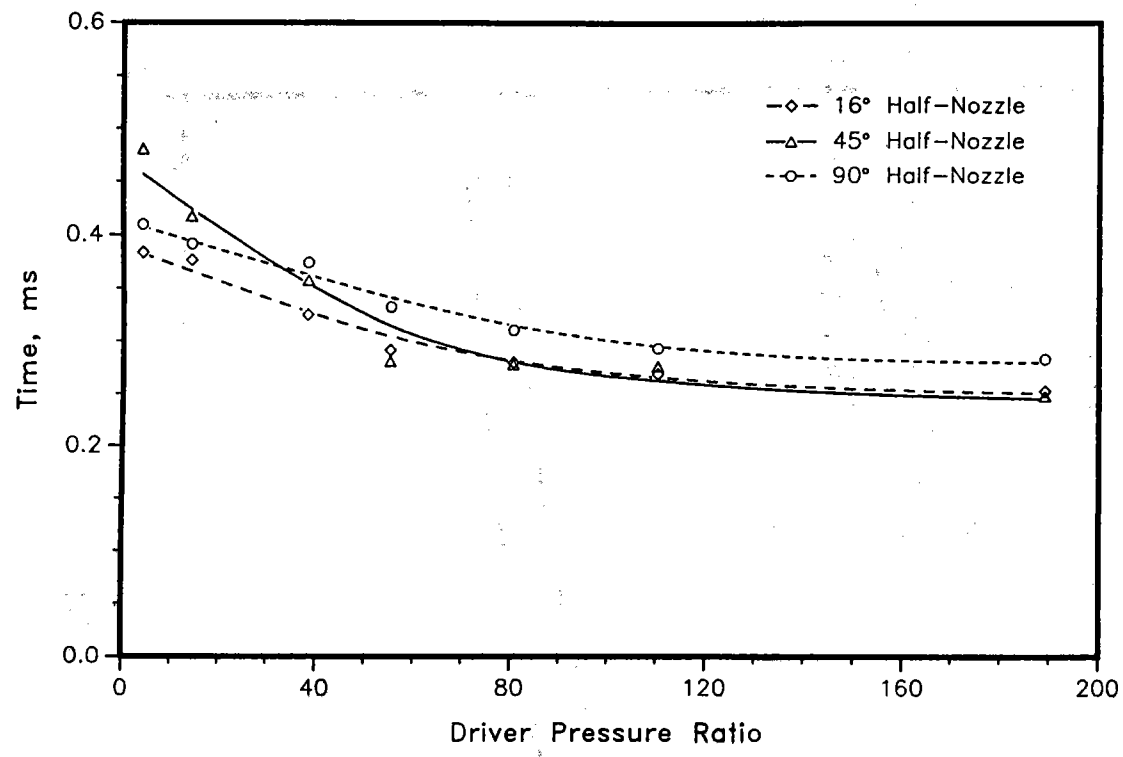

a) Shock Formation Period

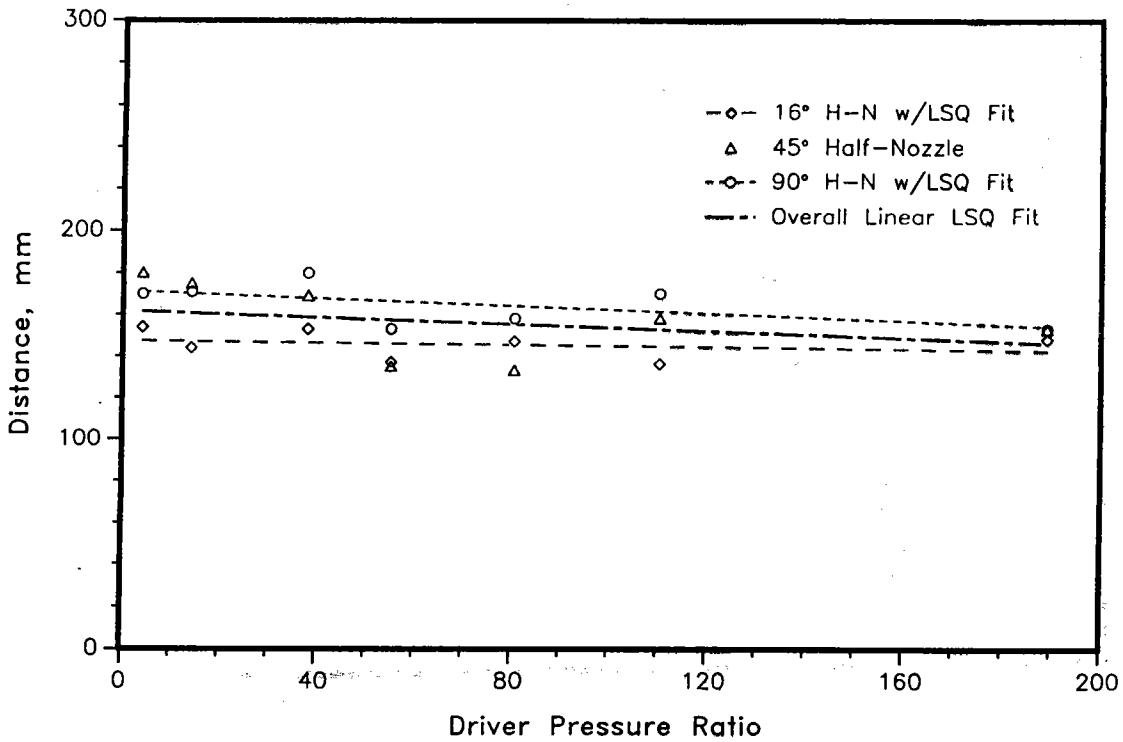

b) Shock Formation Distance

Figure 17: Incident Shock Formation.

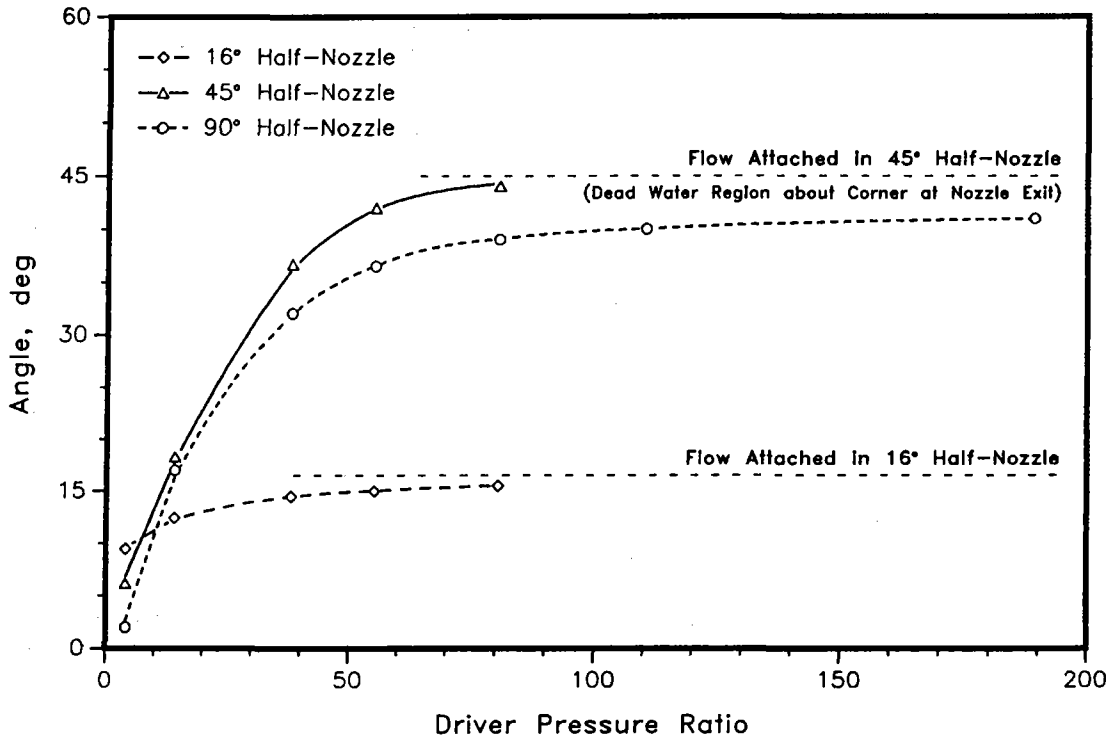

a) Flow Expansion Angle vs. Driver Pressure Ratio

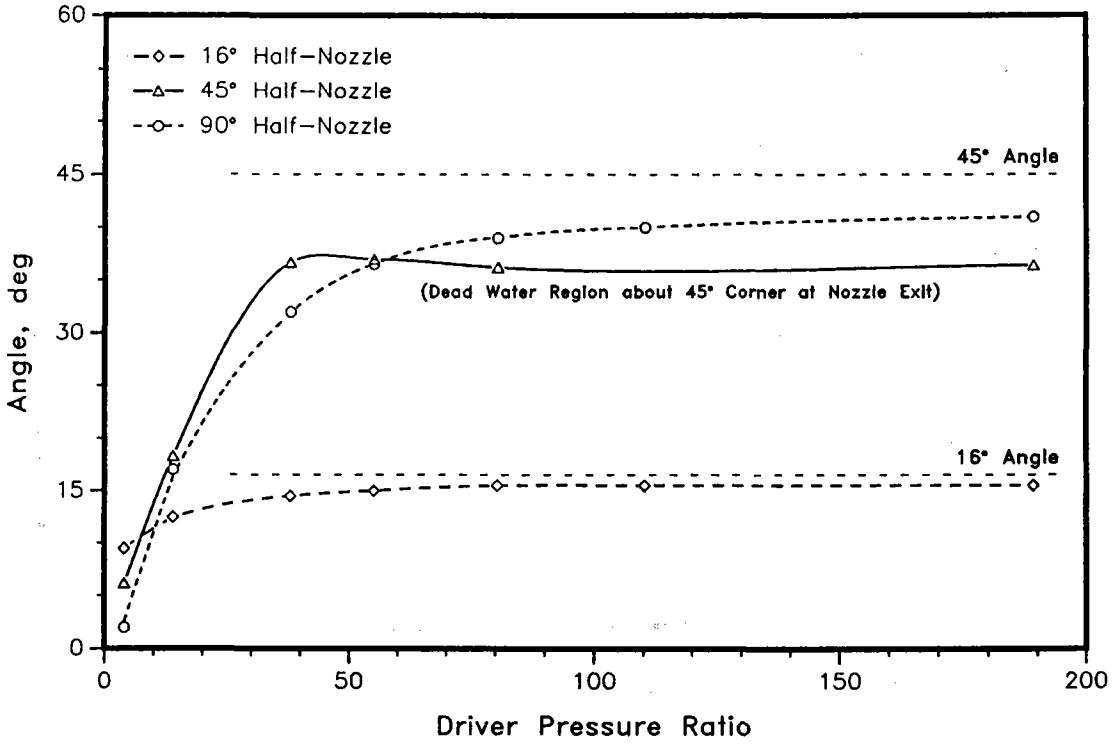

b) Flow Separation Angle vs. Driver Pressure Ratio

Figure 18: Flow Expansion in the 16°, 45°, and 90° Half-Nozzles.

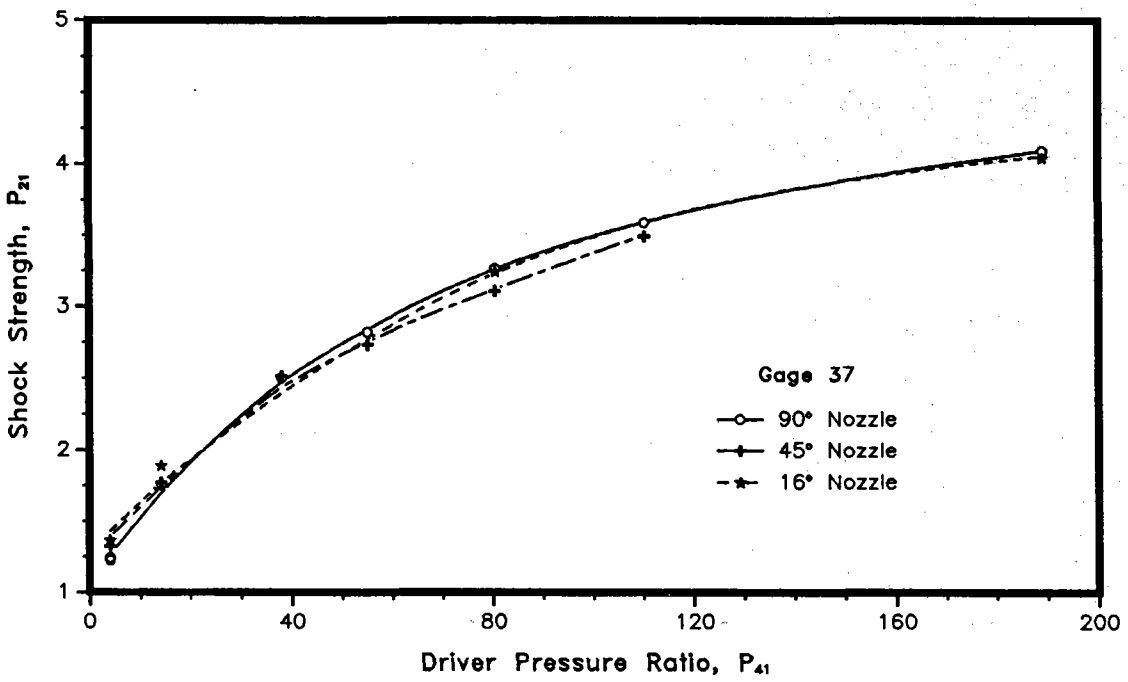

a) Shock Strength vs. Driver Pressure Ratio

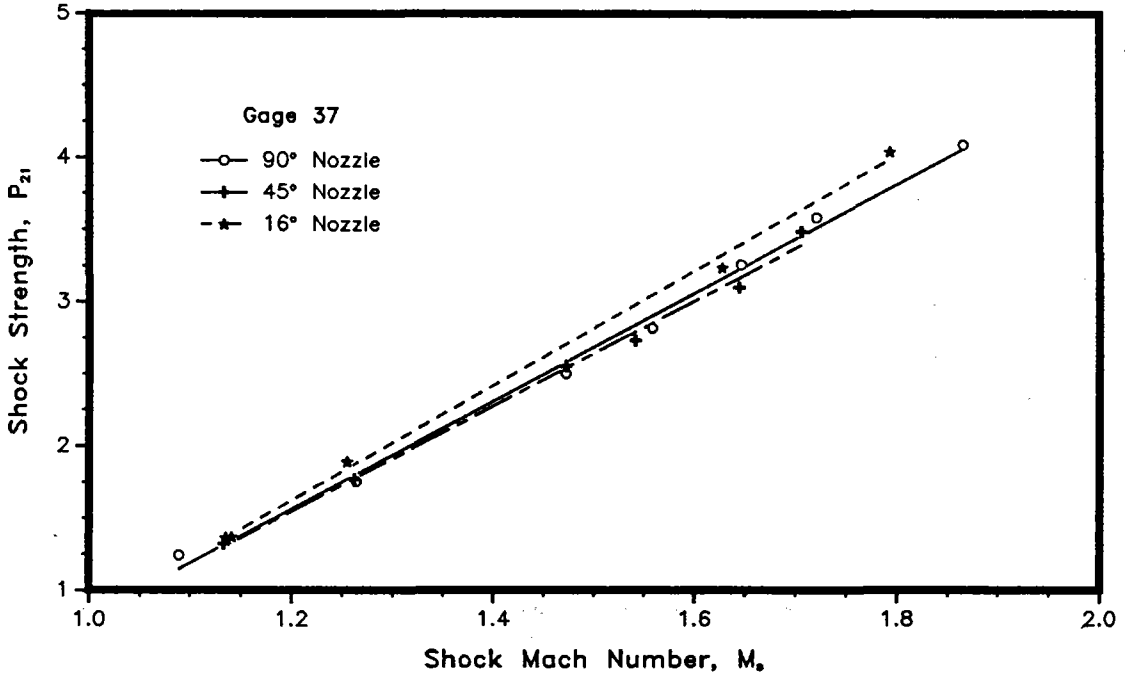

b) Shock Strength vs. Shock Mach Number

Figure 19: Shock Strength at Gage # 37 (370mm from the Diaphragm).

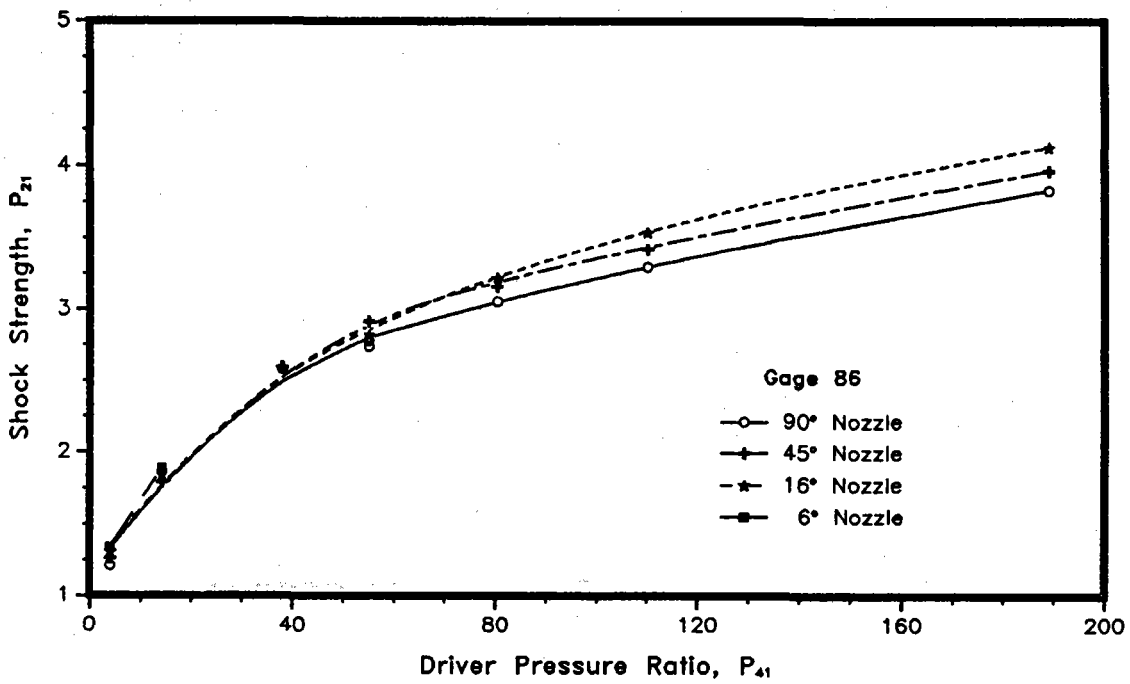

a) Shock Strength vs. Driver Pressure Ratio

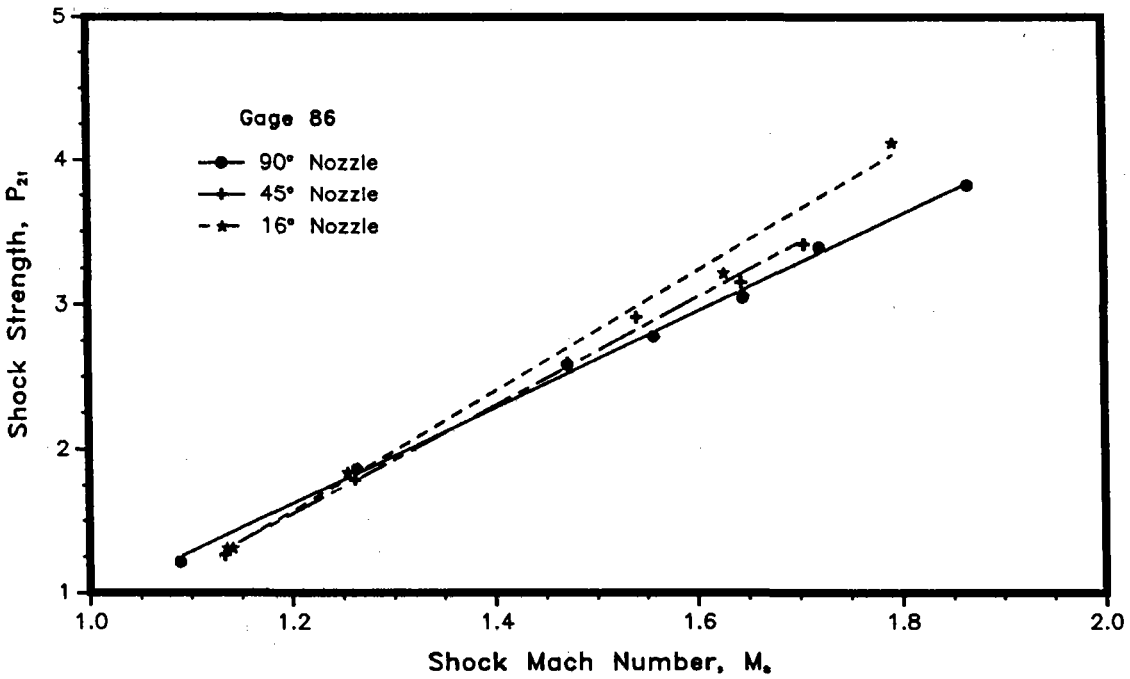

b) Shock Strength vs. Shock Mach Number

Figure 20: Shock Strength at Gage # 86 (860mm from the Diaphragm).

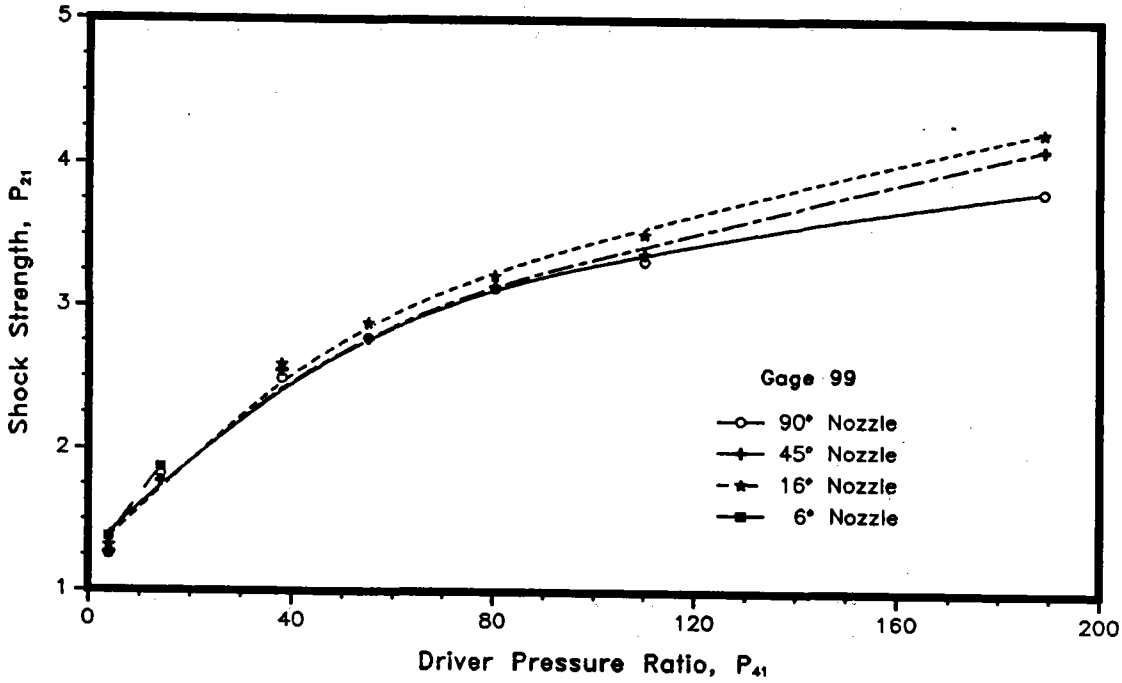

a) Shock Strength vs. Driver Pressure Ratio

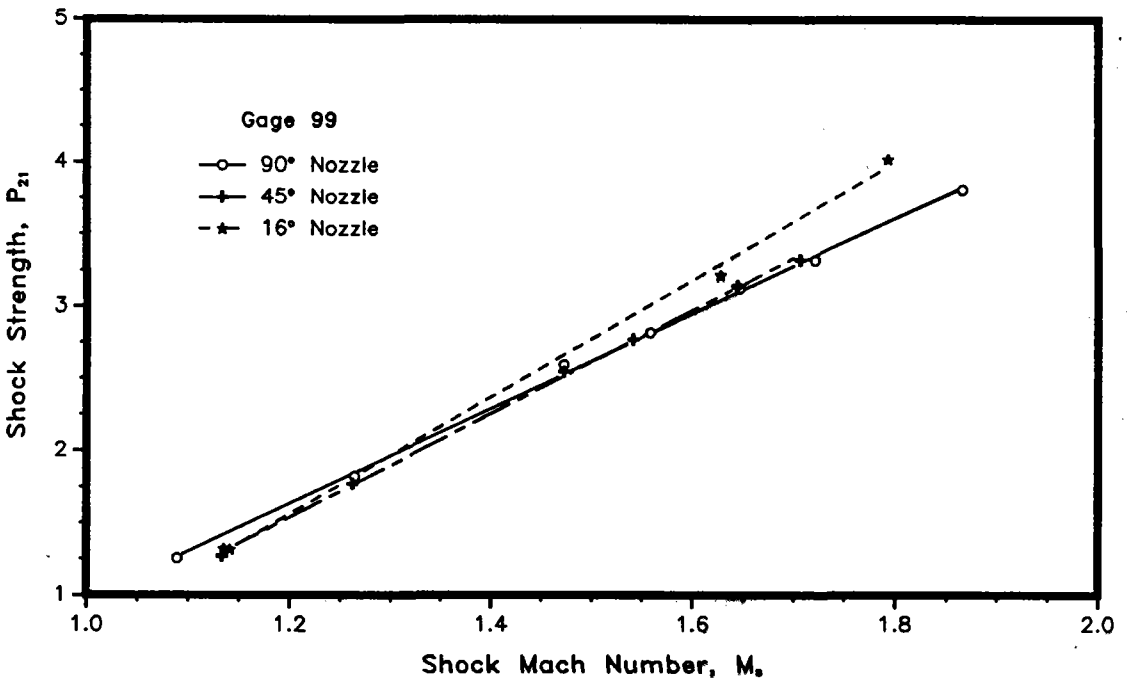

b) Shock Strength vs. Shock Mach Number

Figure 21: Shock Strength at Gage # 99 (989 mm from the Diaphragm).

APPENDIX A: X-t DIAGRAMS OF EXPERIMENTAL DATA

(intentionally left blank)

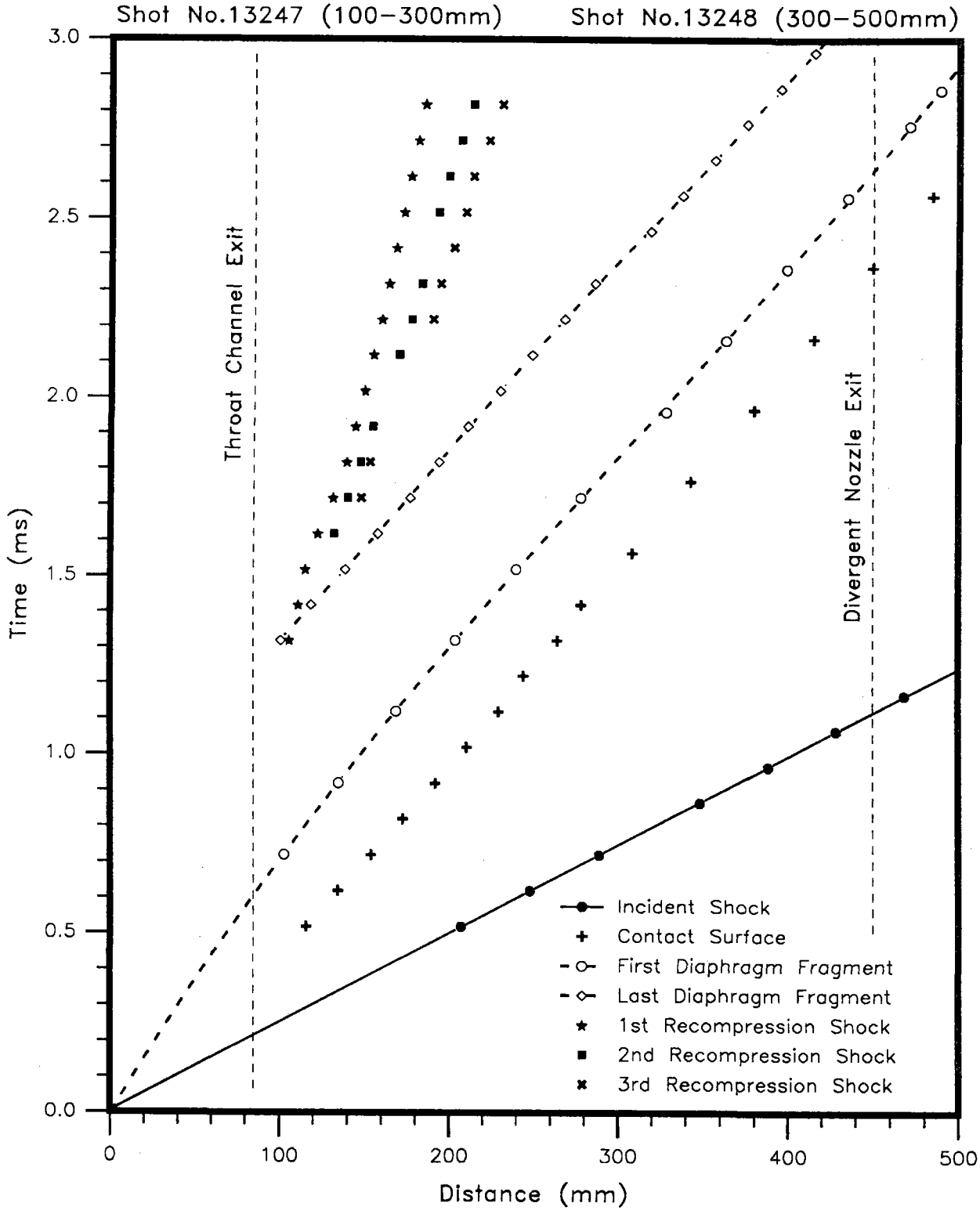

Figure A-1. 6° Nozzle at P_{41}= 4

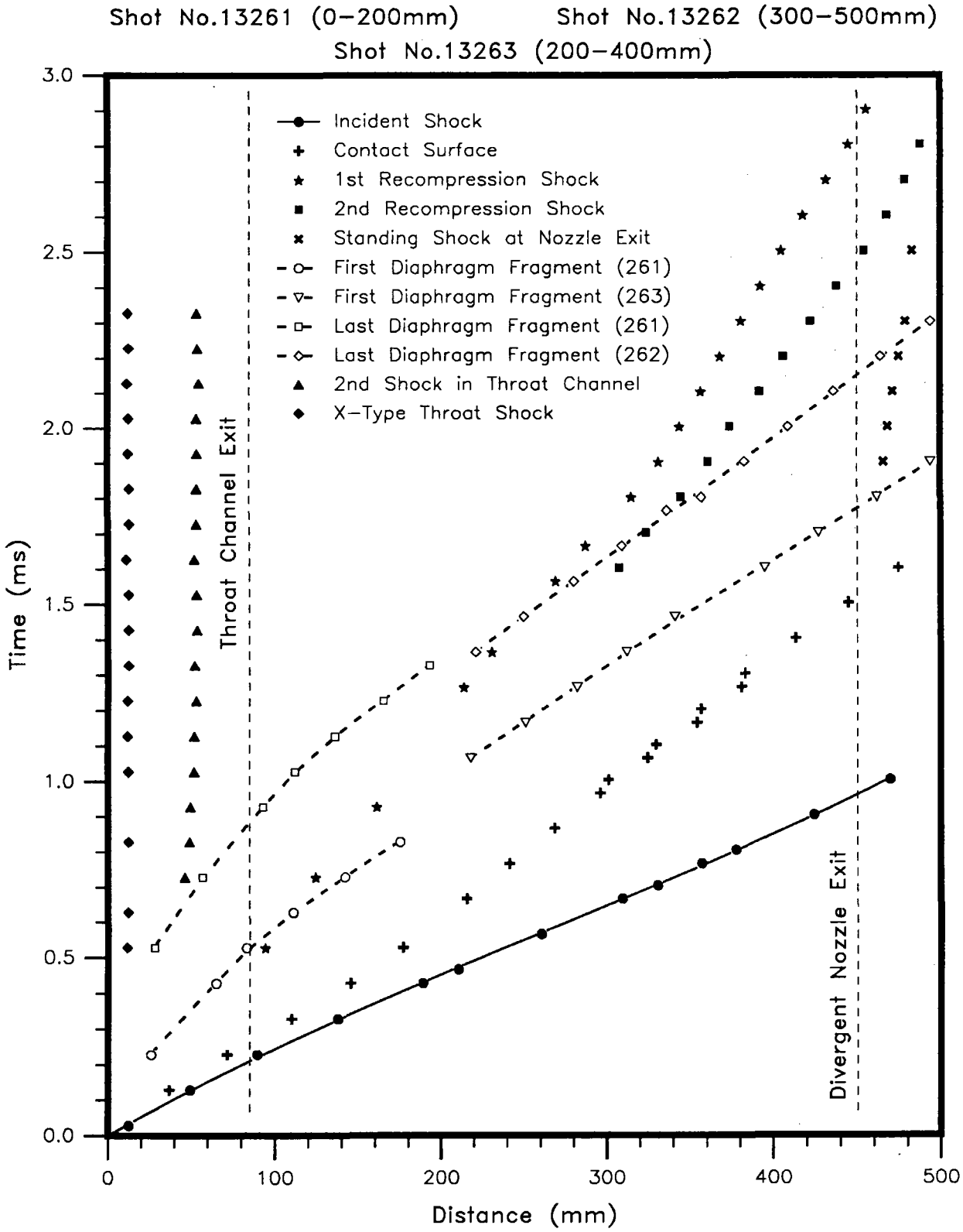

Figure A-2. 6° Nozzle at P_{41}= 14

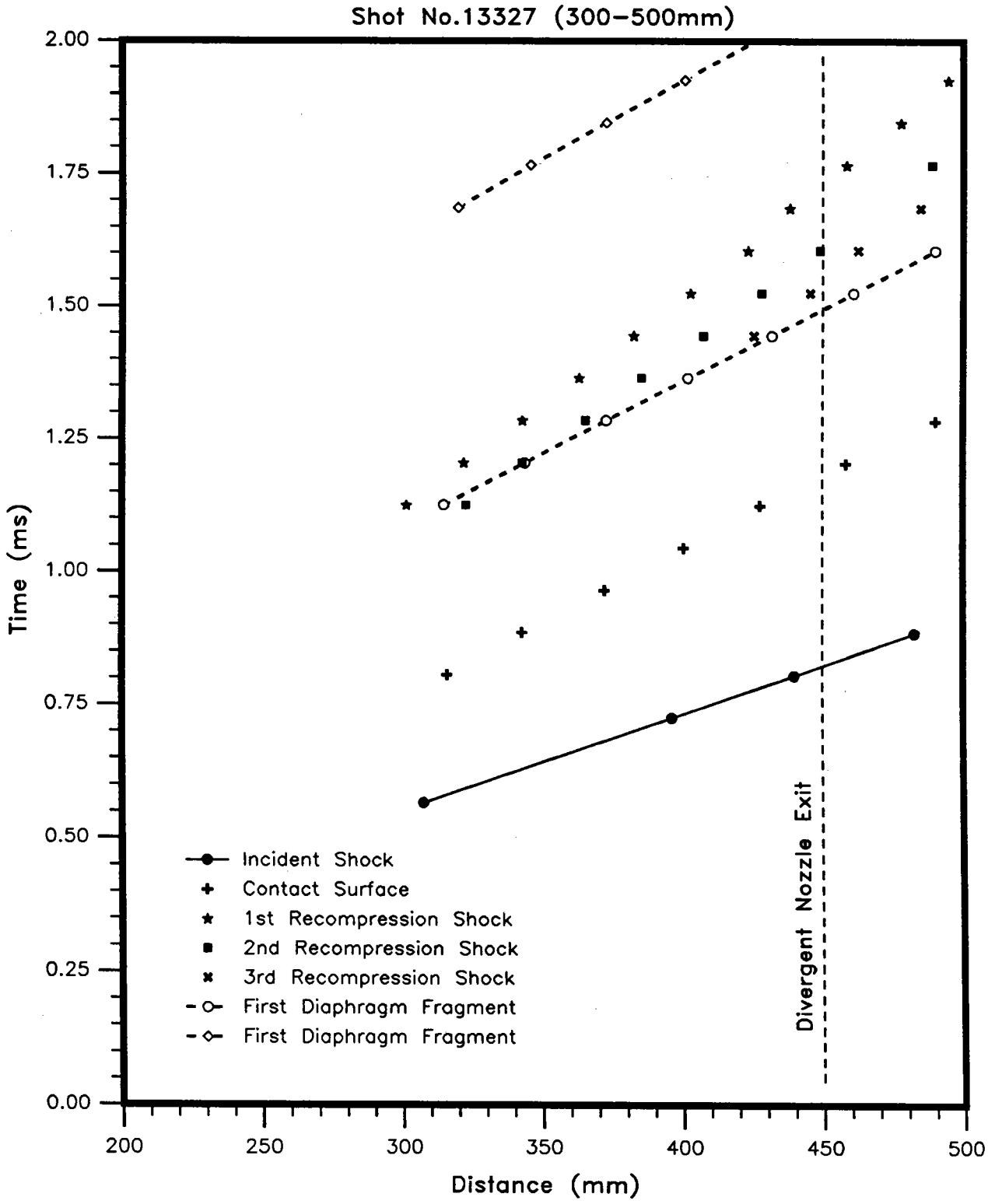

Figure A-3: 6° Nozzle at P_{41}=38.

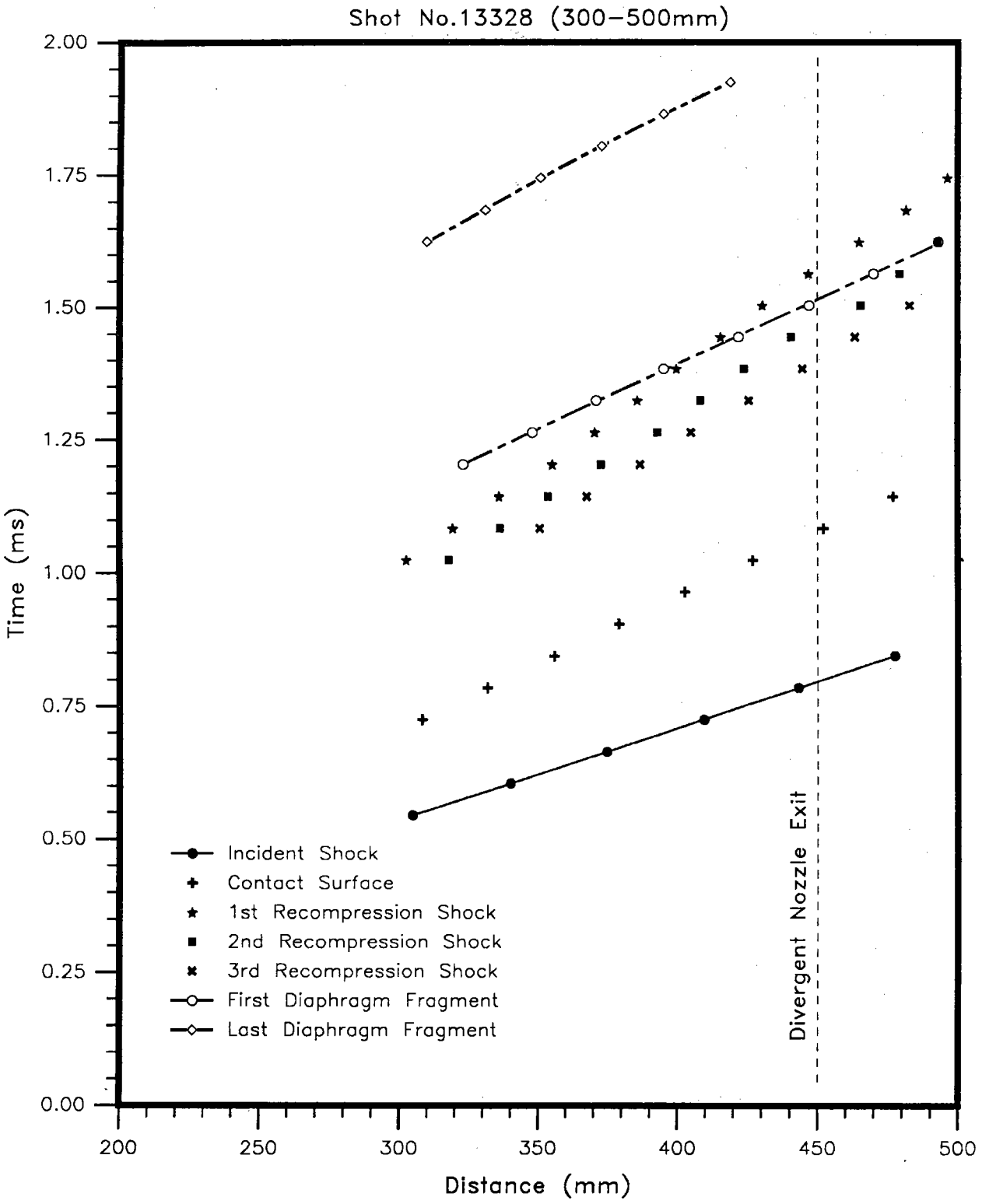

Figure A–4. 6° Nozzle at P_{41}= 55

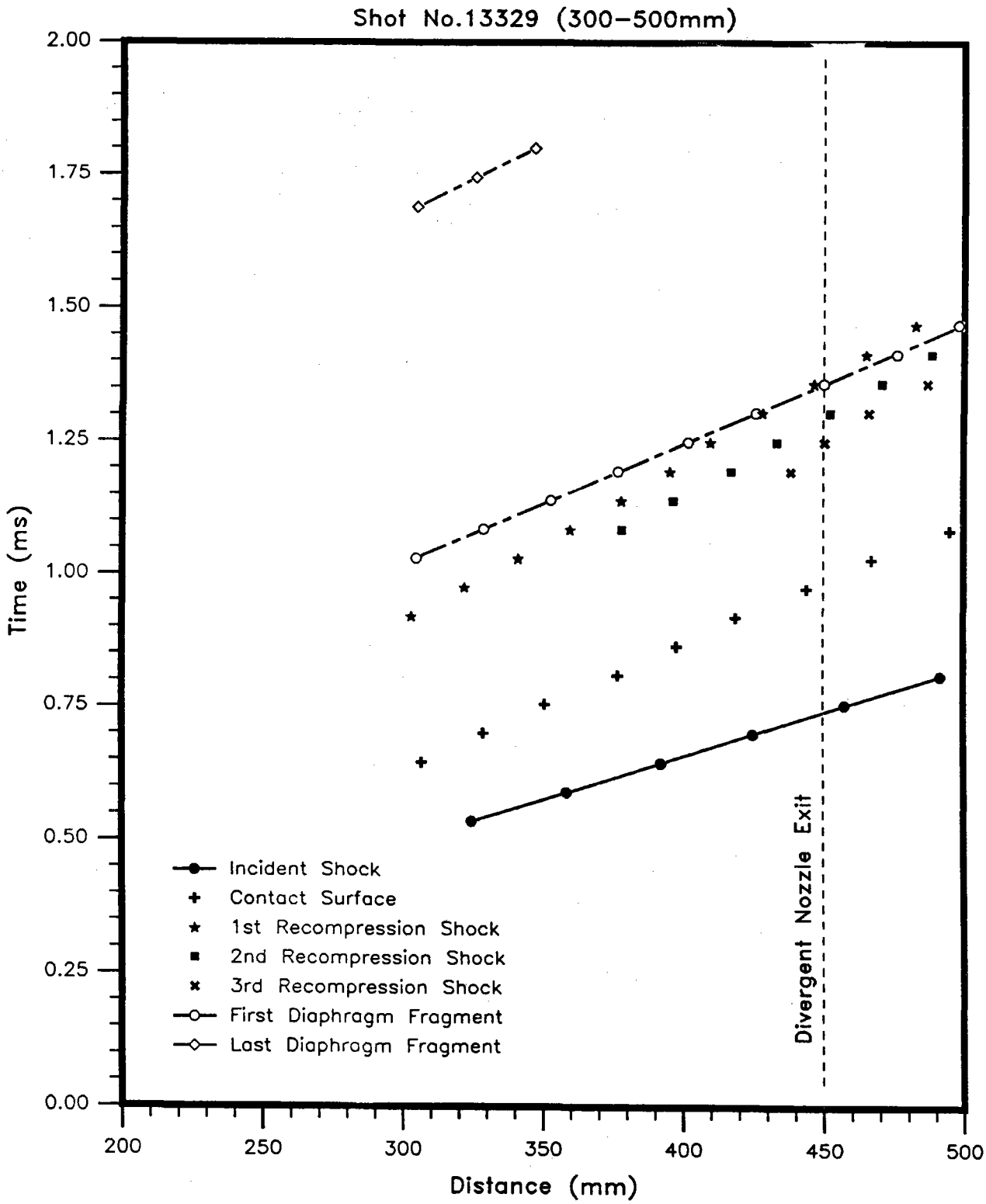

Figure A-5. 6° Nozzle at P_{41}= 80

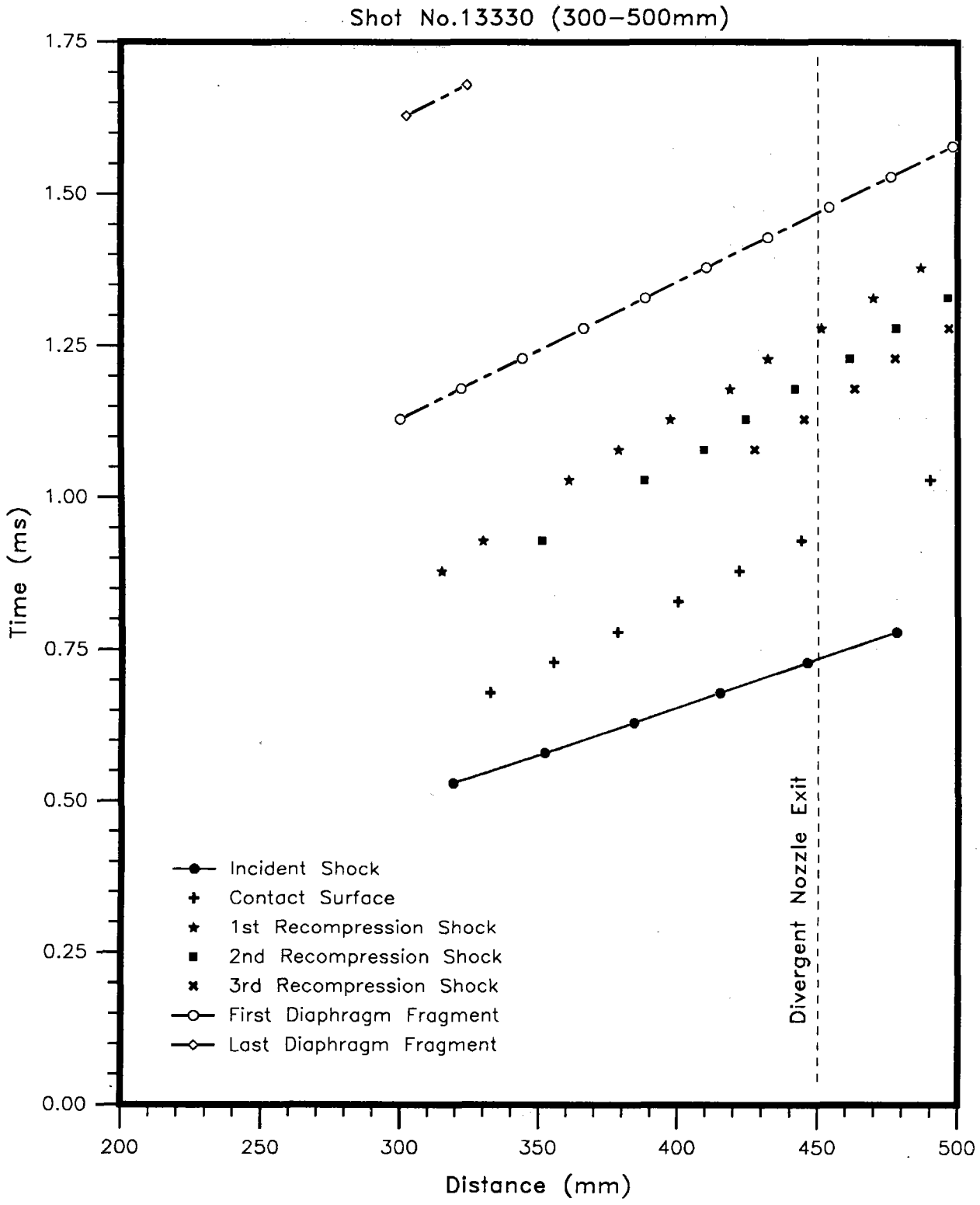

Figure A-6. 6° Nozzle at P_{41}= 110

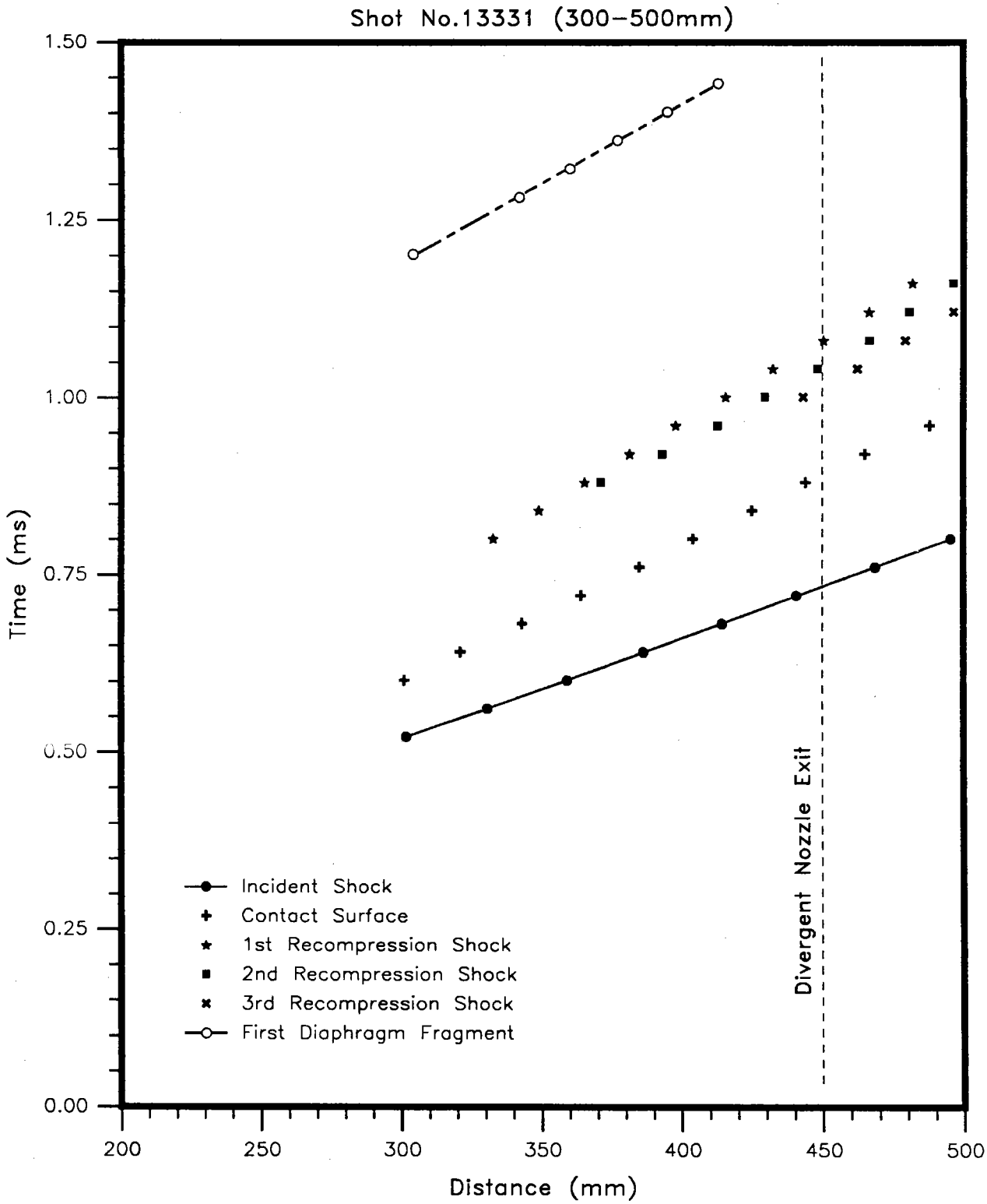

Figure A-7. 6° Nozzle at P_{41}= 188

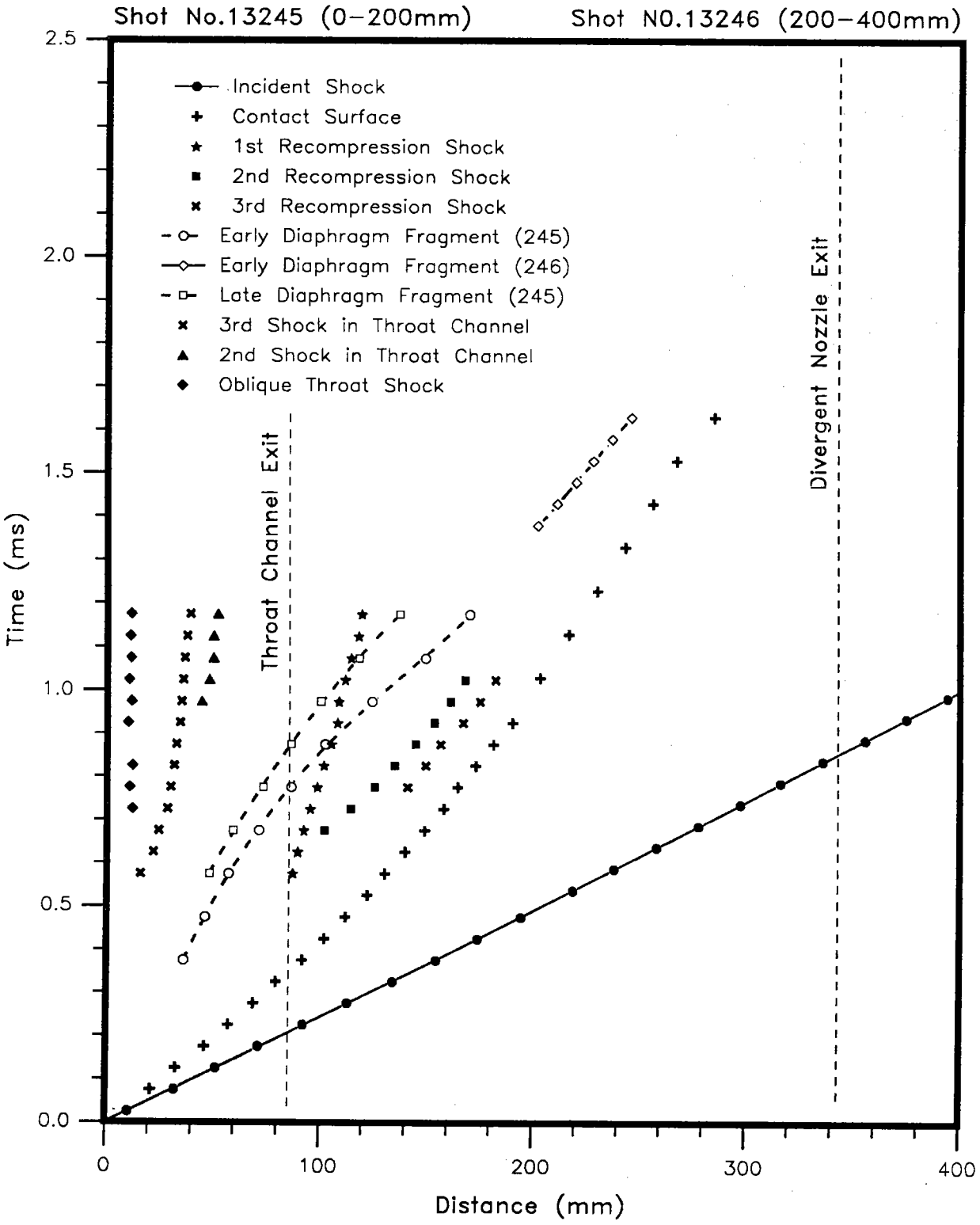

Figure A-8. 16° Nozzle at P_{41}= 4

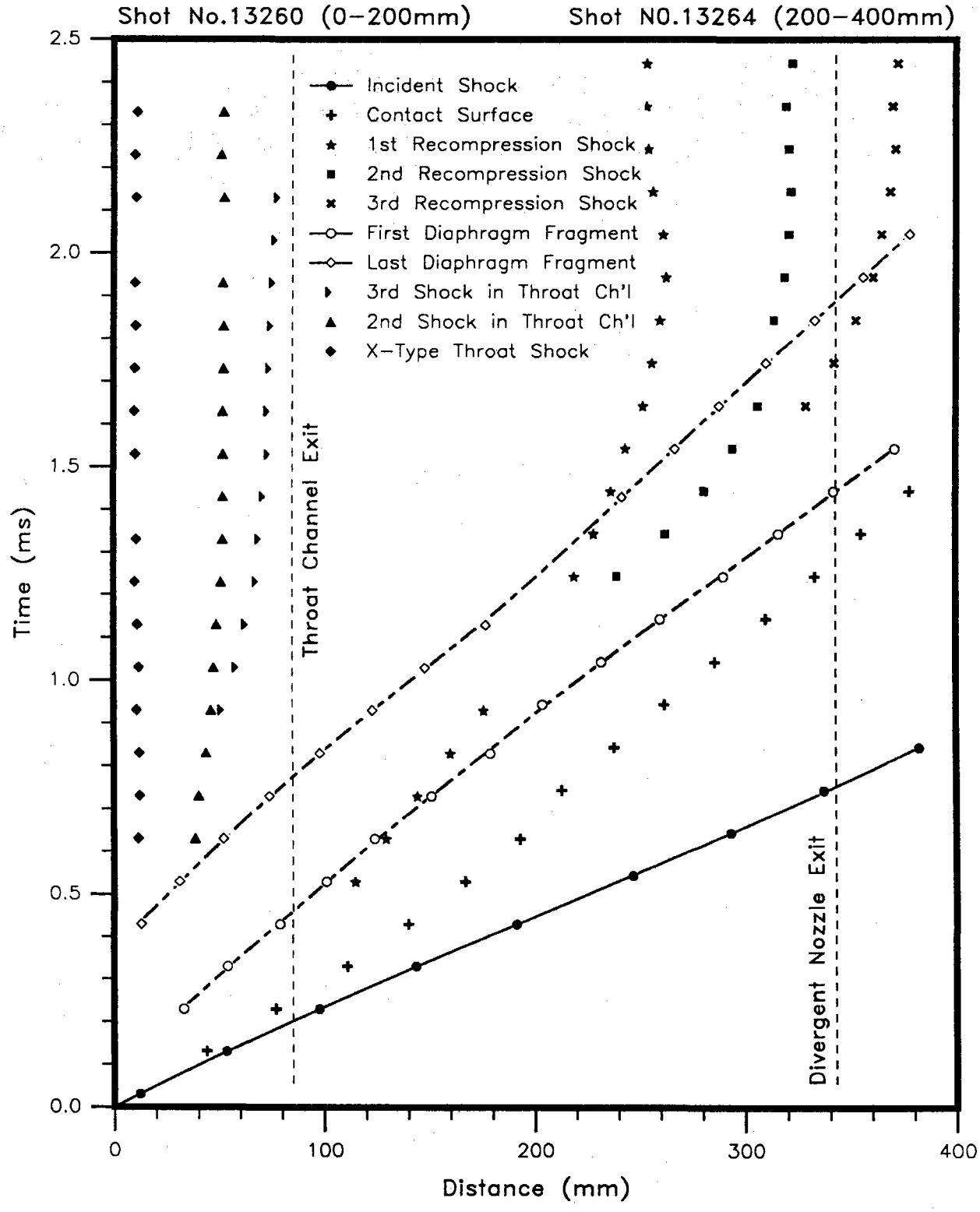

Figure A-9. 16° Nozzle at P_{41}= 14

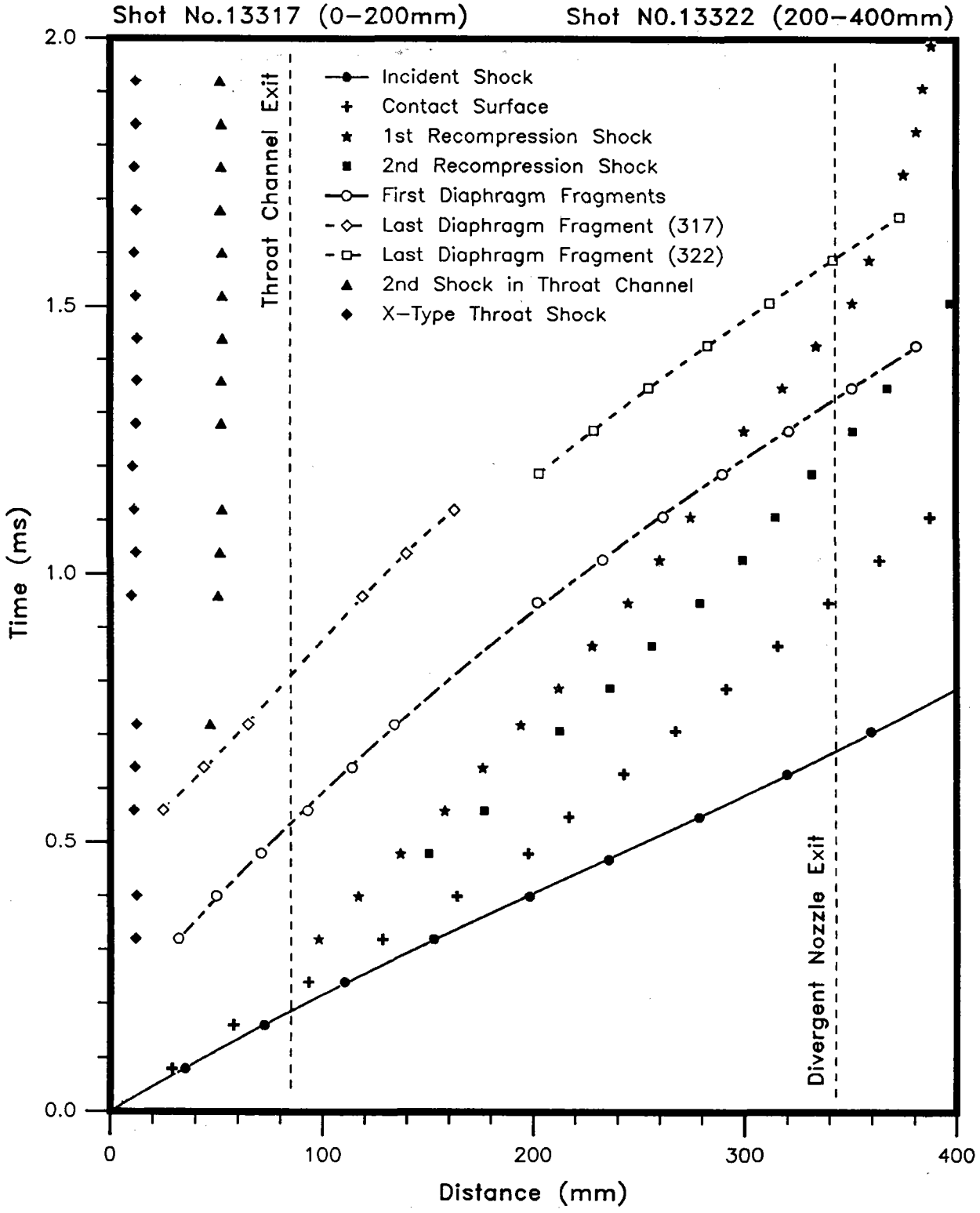

Figure A-10. 16° Nozzle at P_{41}= 38

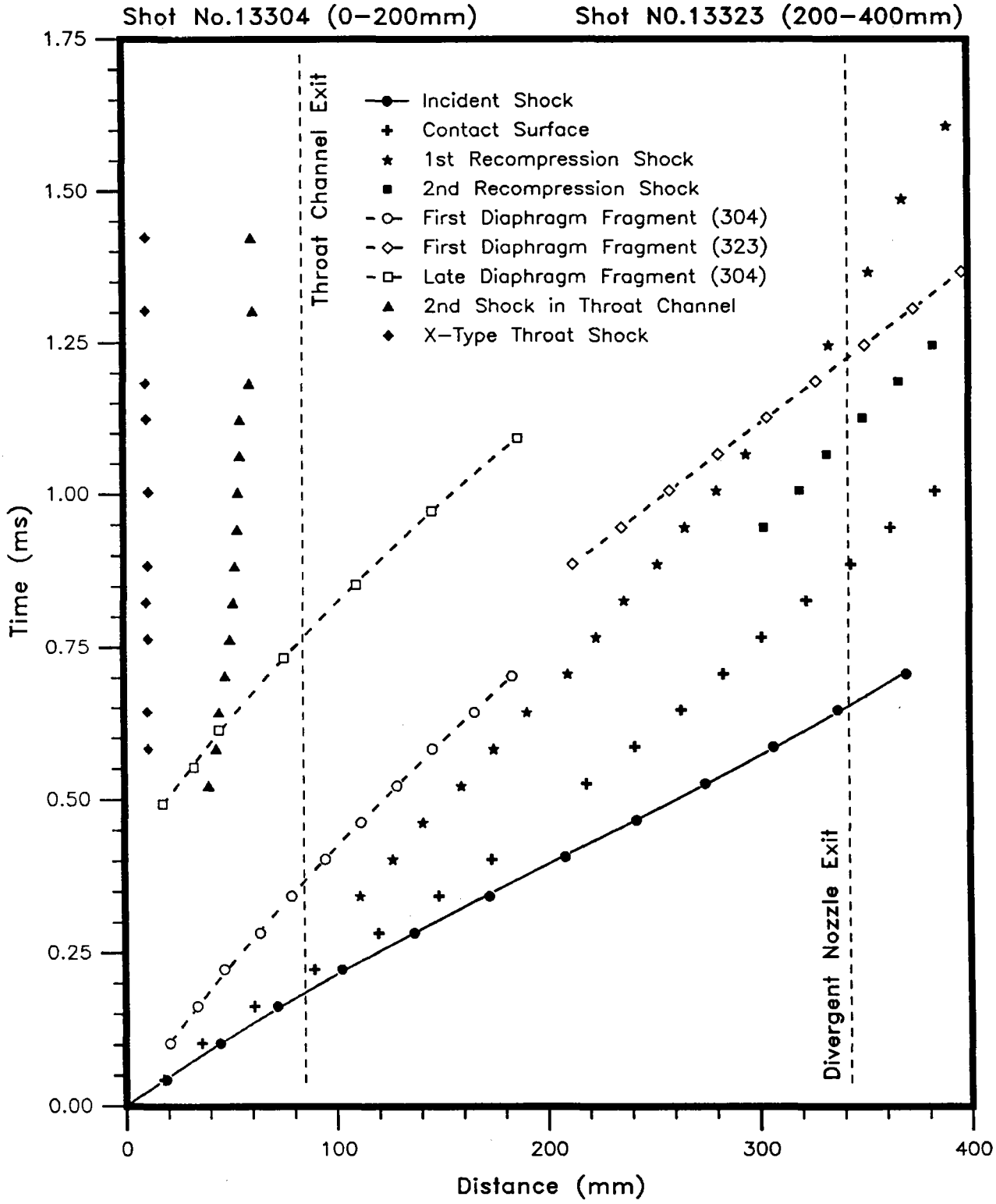

Figure A-11. 16° Nozzle at P_{41}= 55

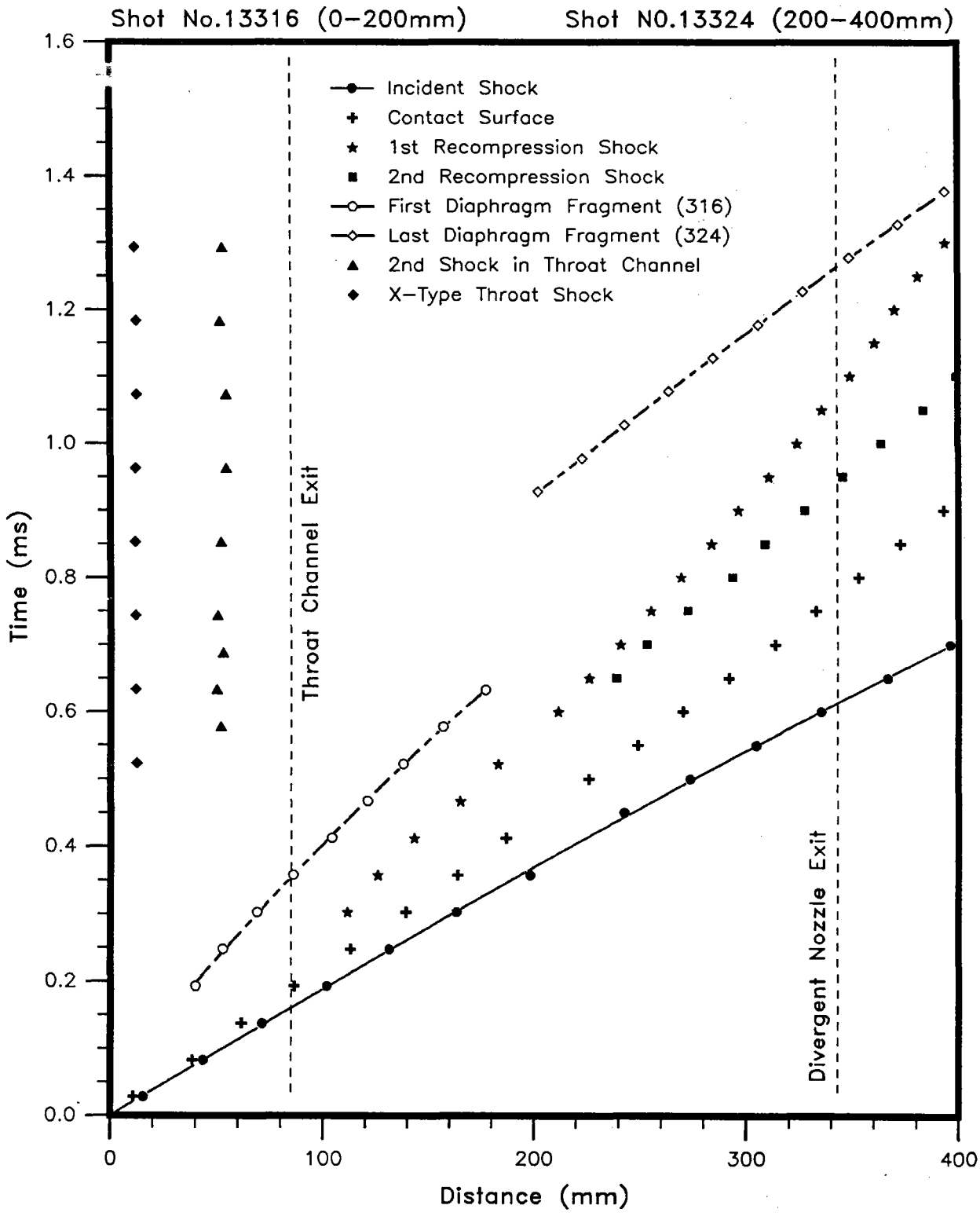

Figure A-12. 16° Nozzle at P_{41}= 80

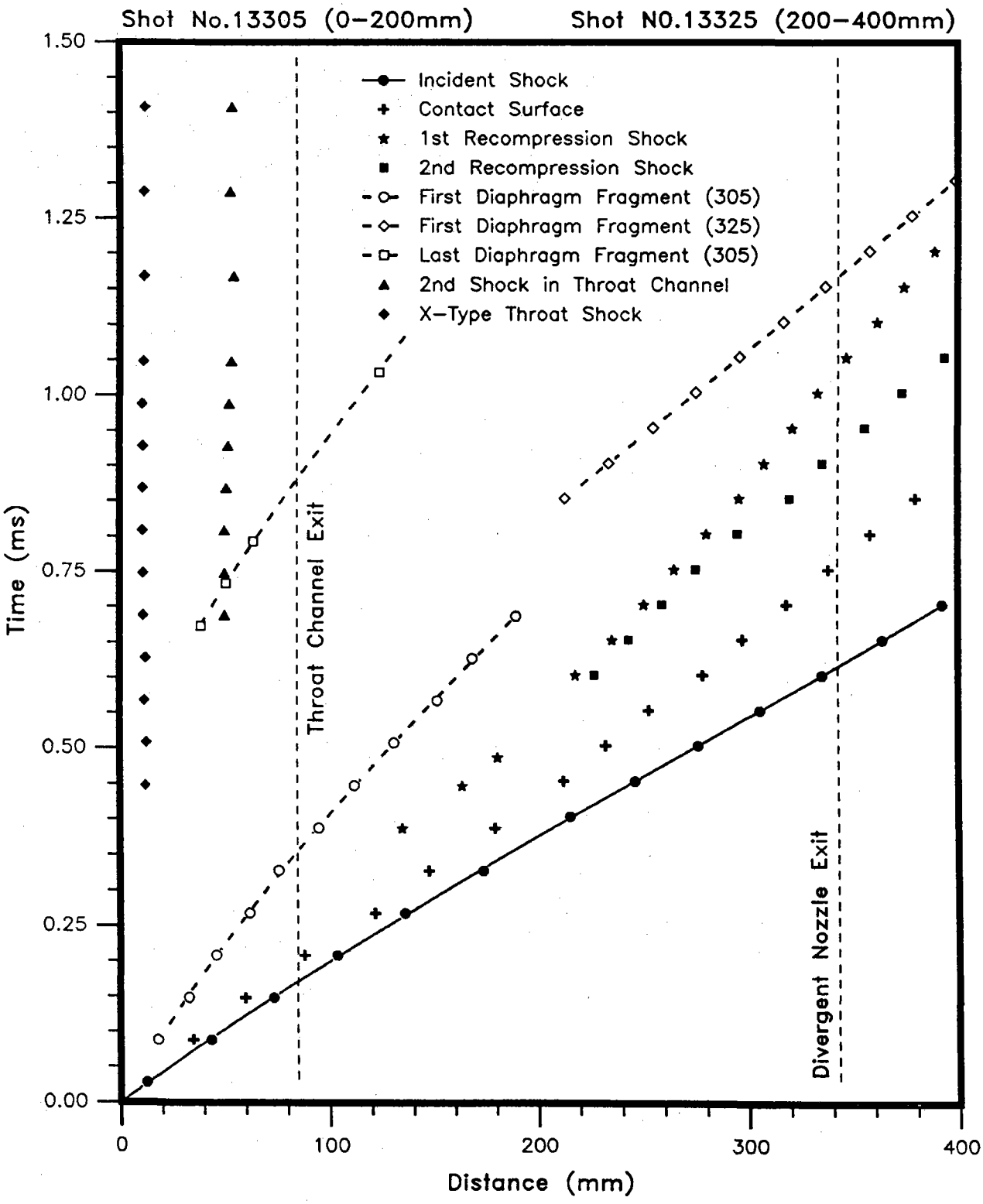

Figure A-13. 16° Nozzle at P_{41}= 110

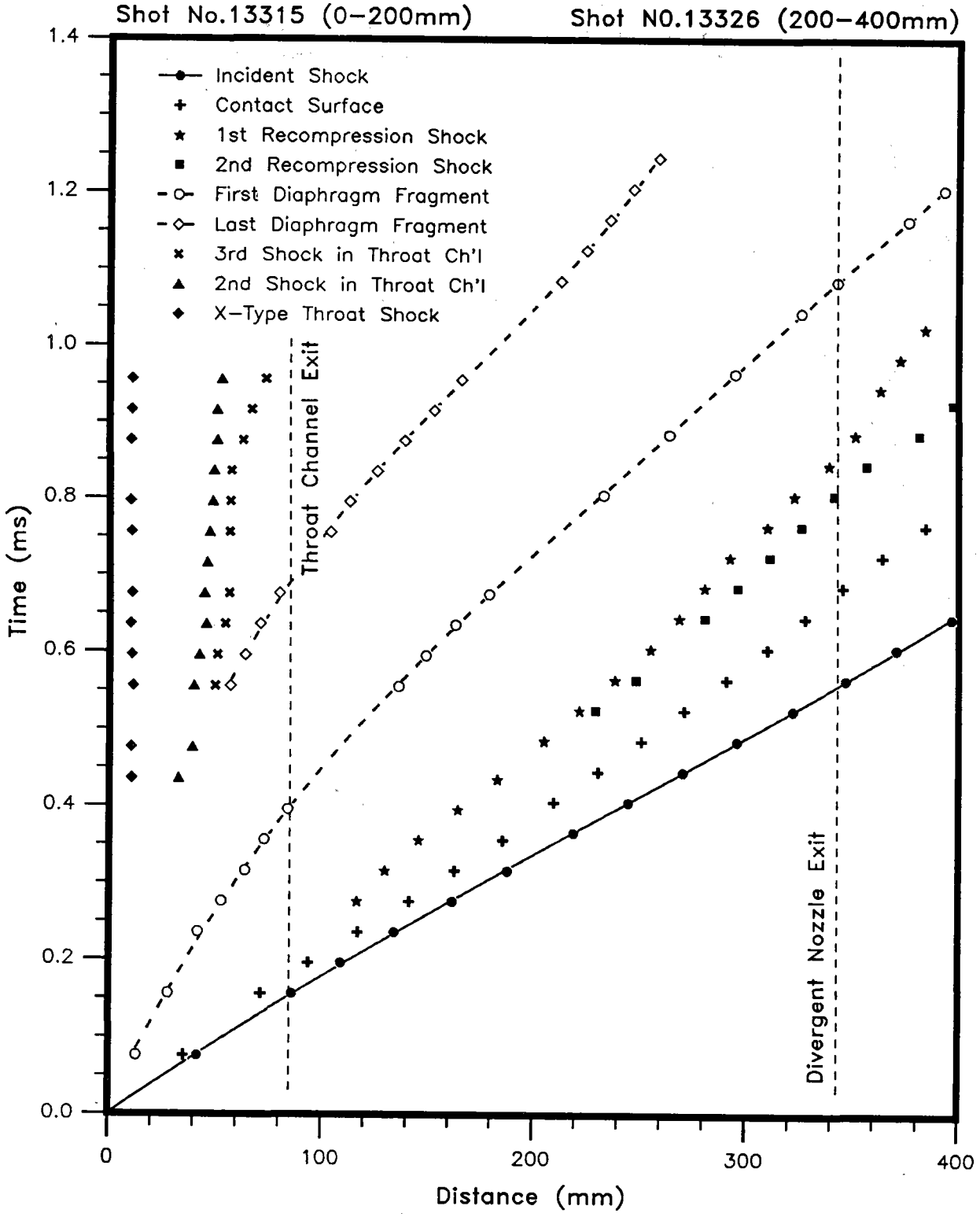

Figure A–14. 16° Nozzle at P_{41}= 188

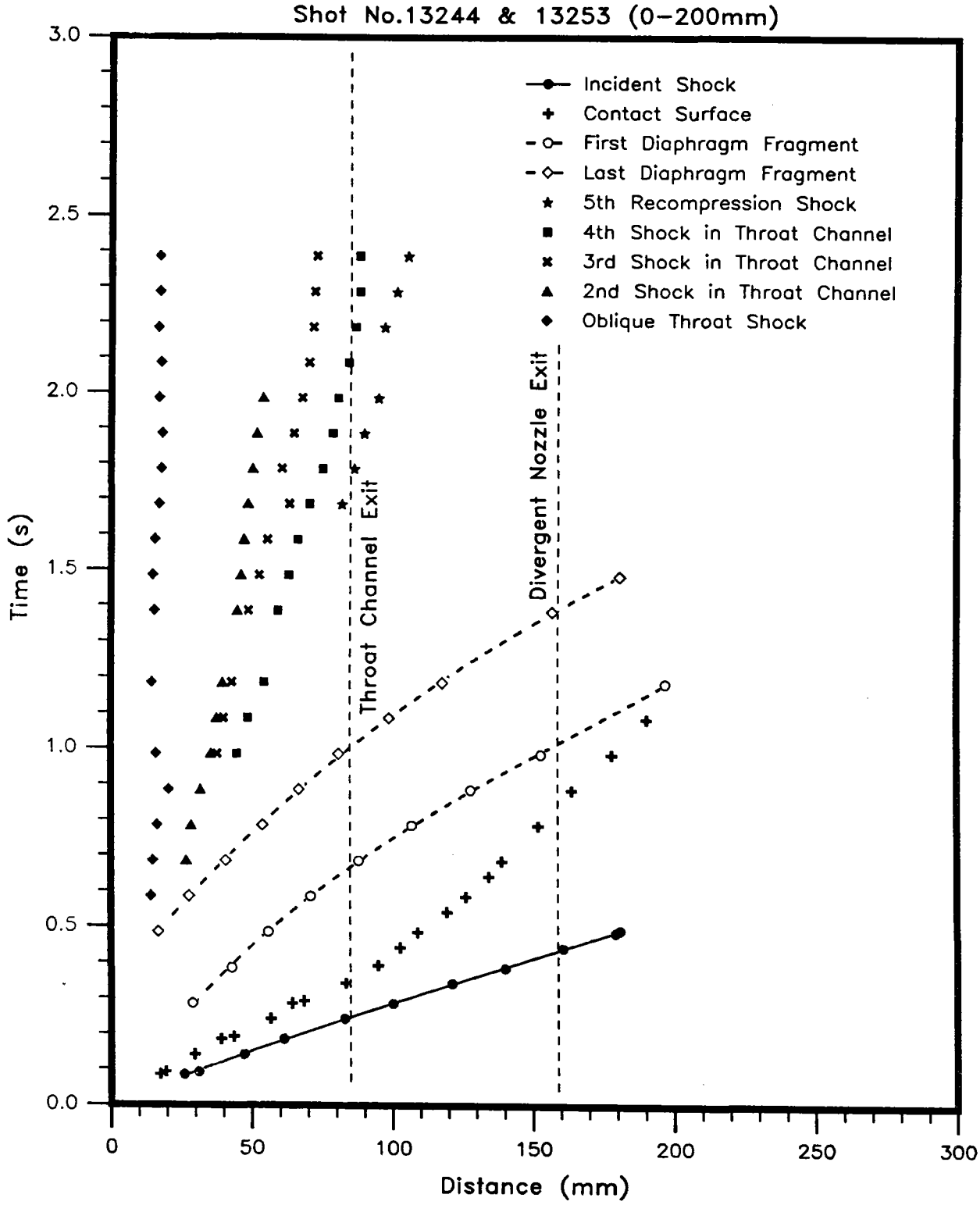

Figure A-15: 45° Nozzle at P_{41}= 4.

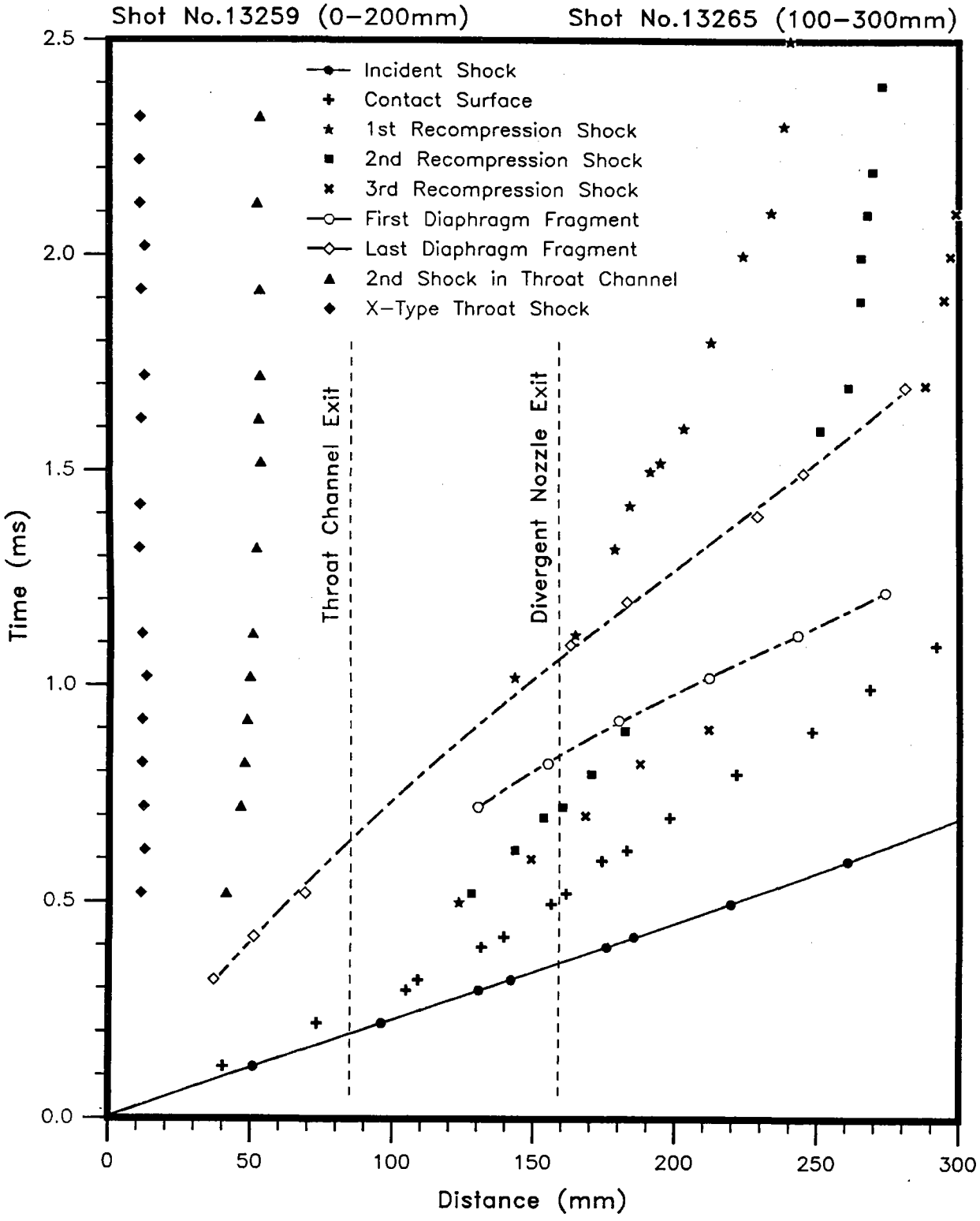

Figure A-16. 45° Nozzle at P_{41}= 14

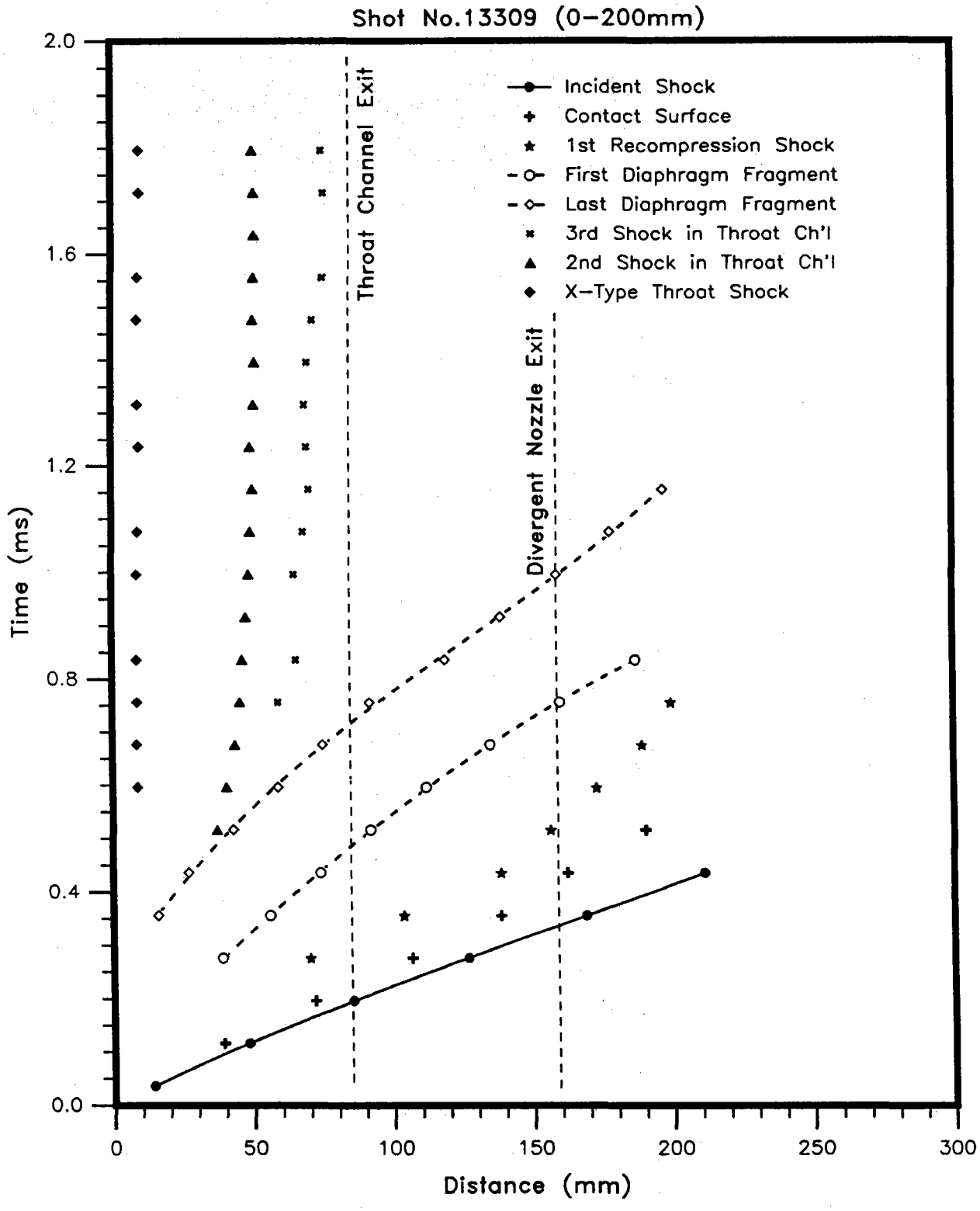

Figure A-17: 45° Nozzle at P_{41}=38.

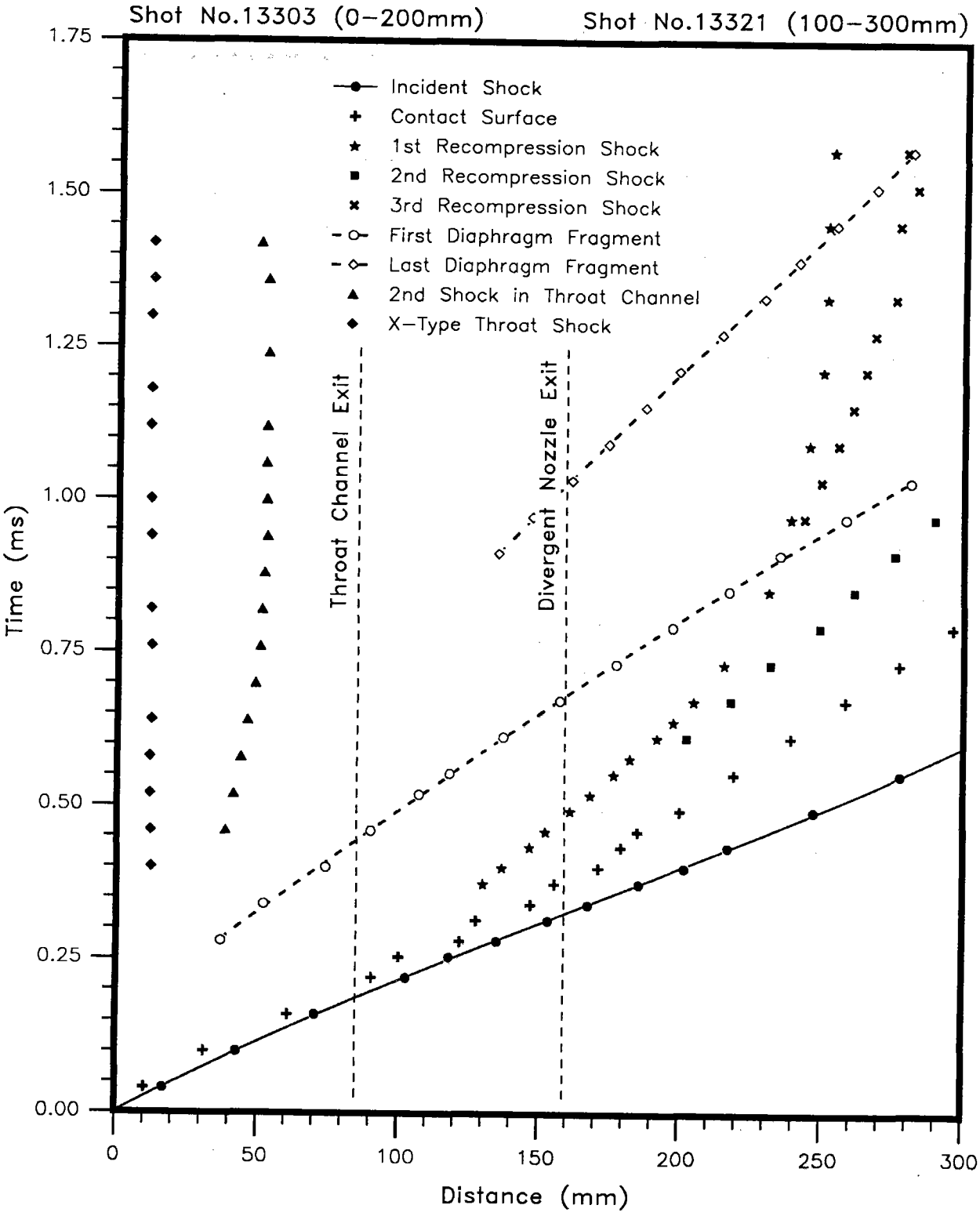

Figure A-18. 45° Nozzle at P_{41}= 55

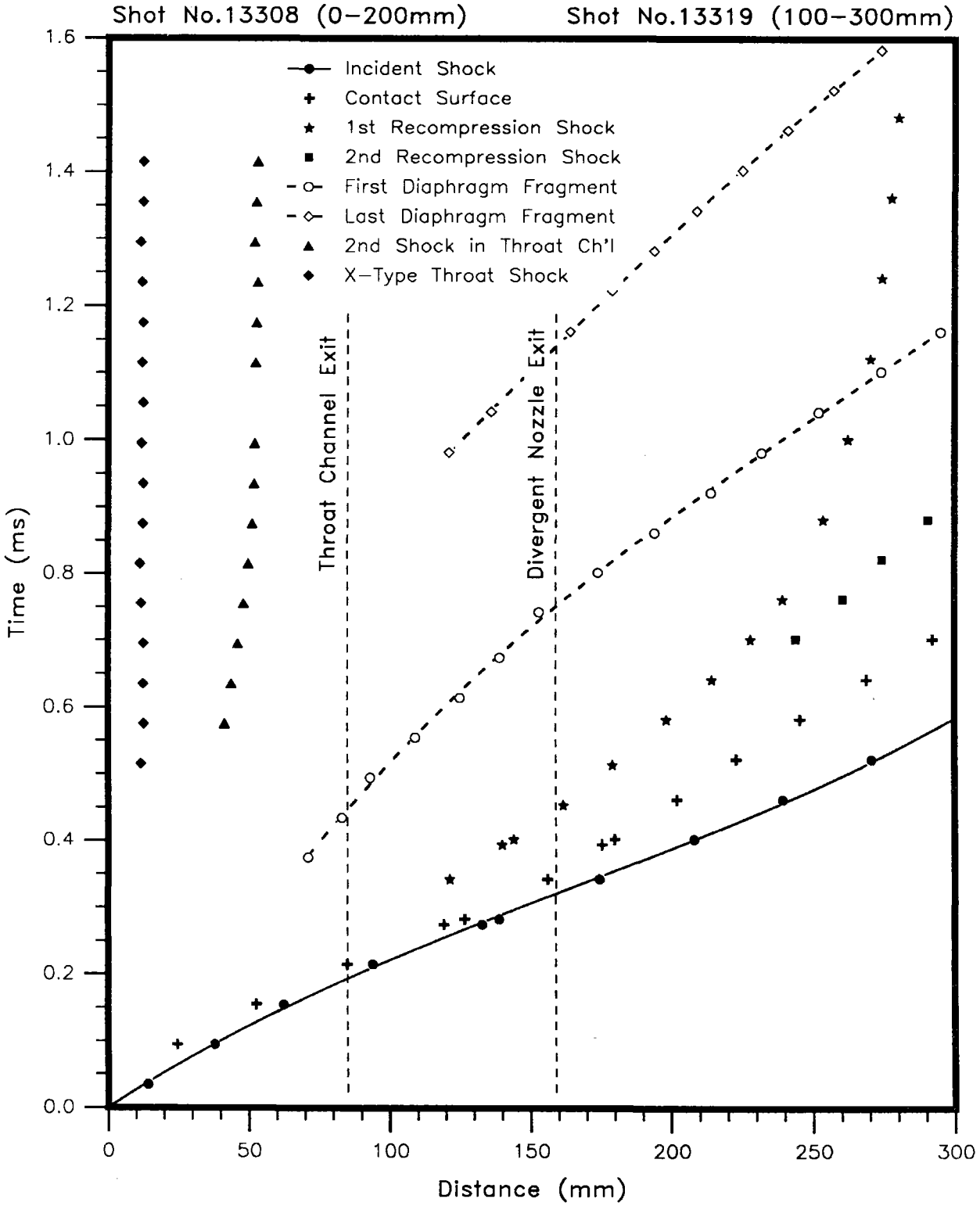

Figure A-19. 45° Nozzle at P_{41}= 80

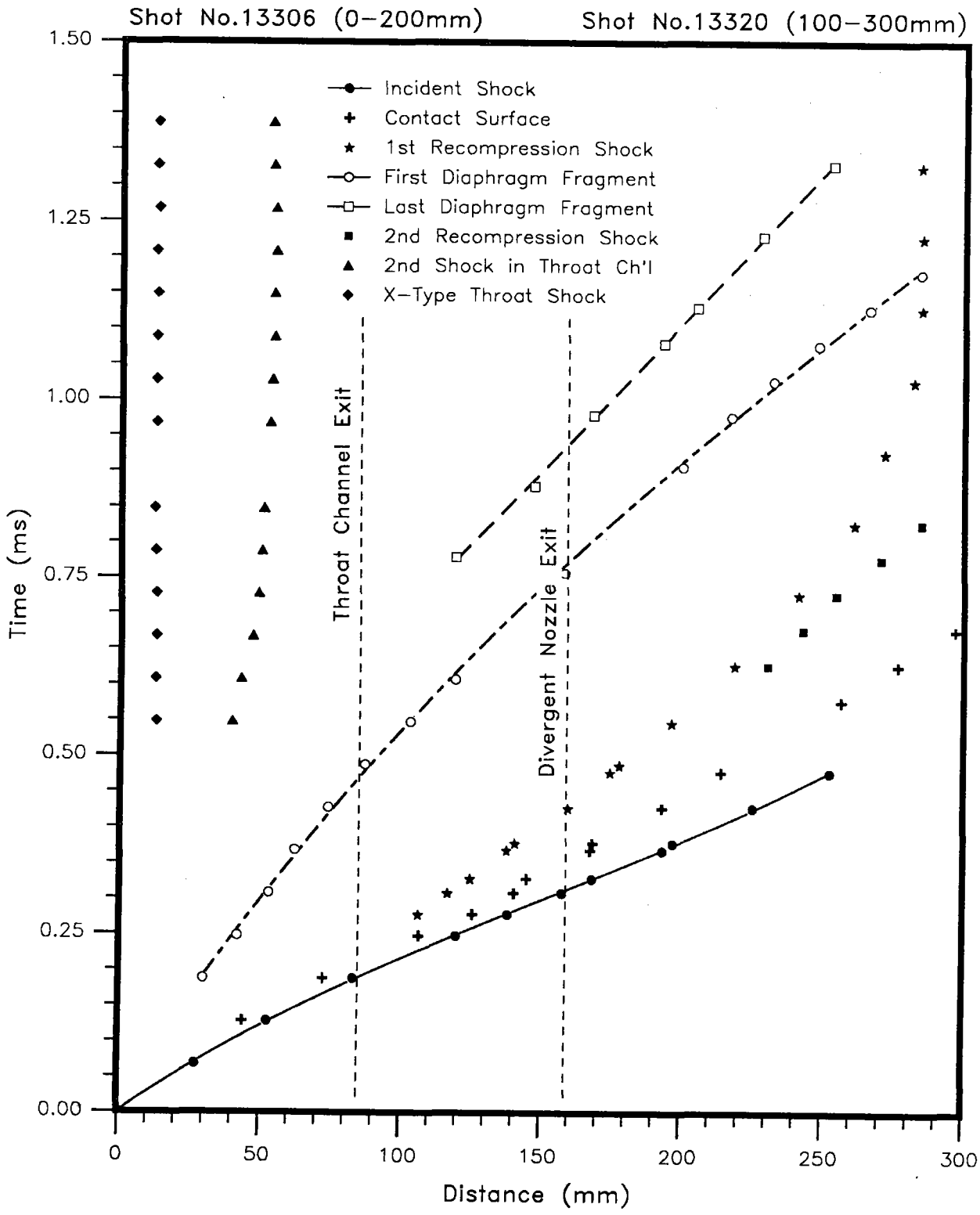

Figure A-20. 45° Nozzle at P_{41}= 110

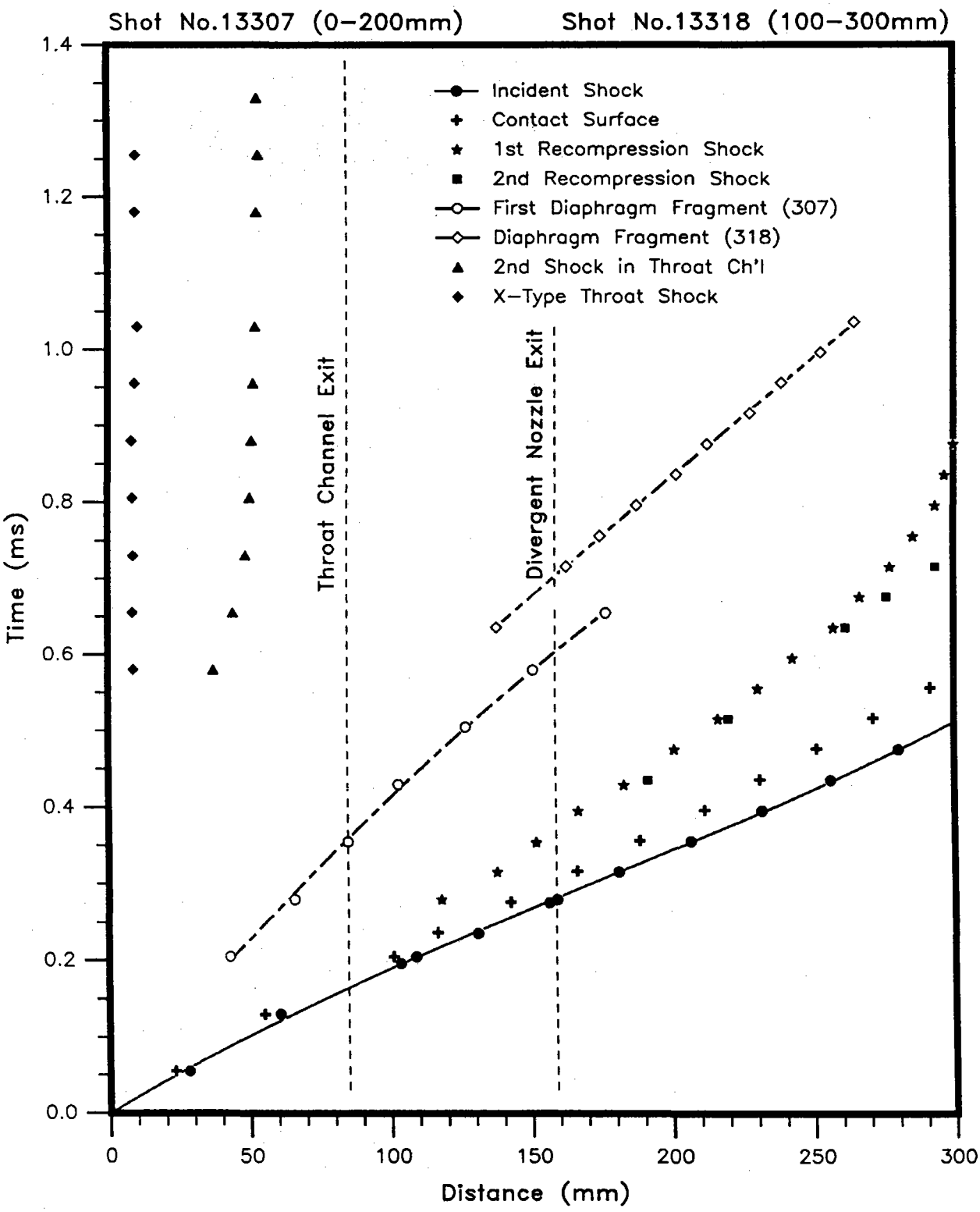

Figure A-21. 45° Nozzle at P_{41}= 188

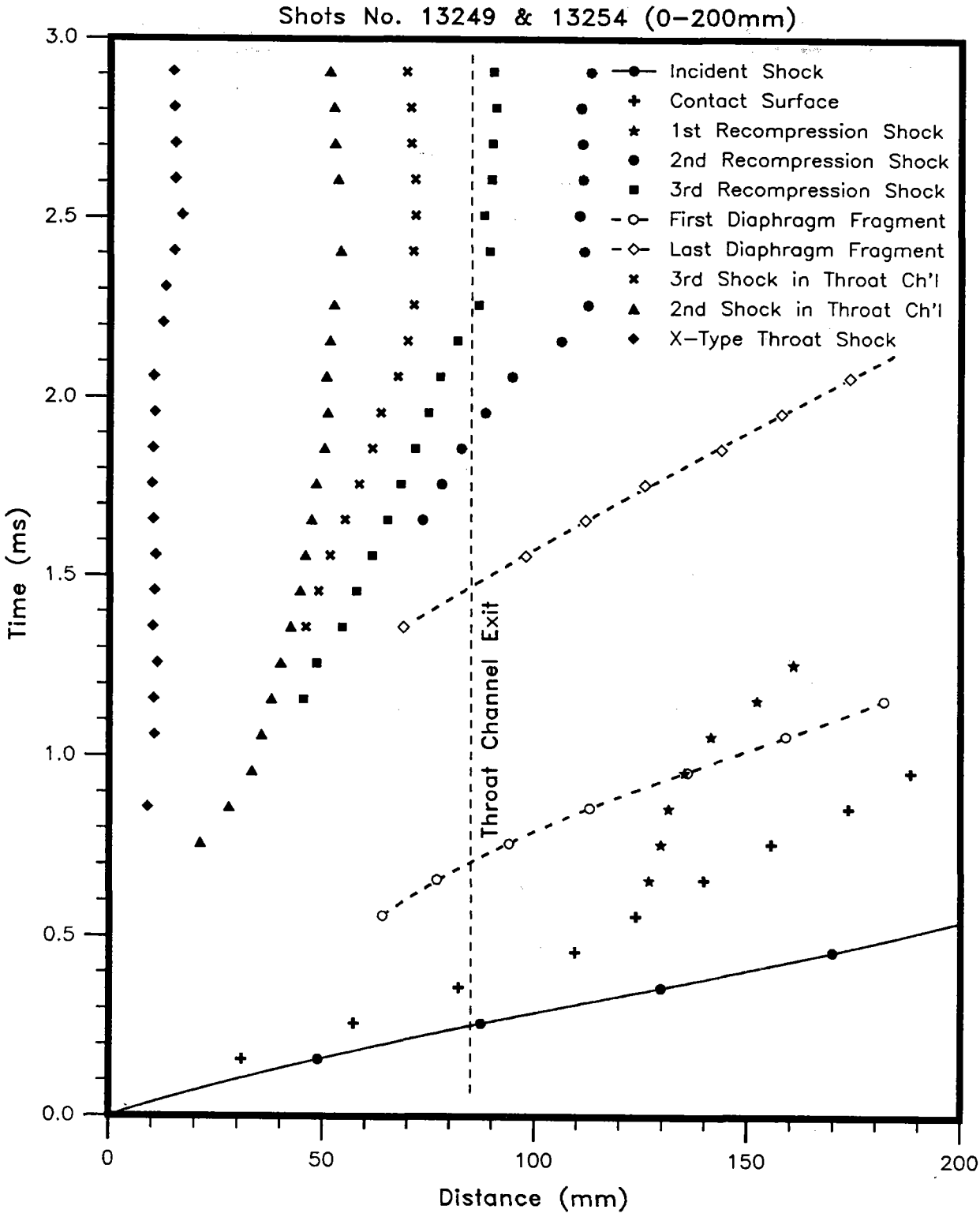

Figure A-22. 90° Nozzle at P_{41}= 4

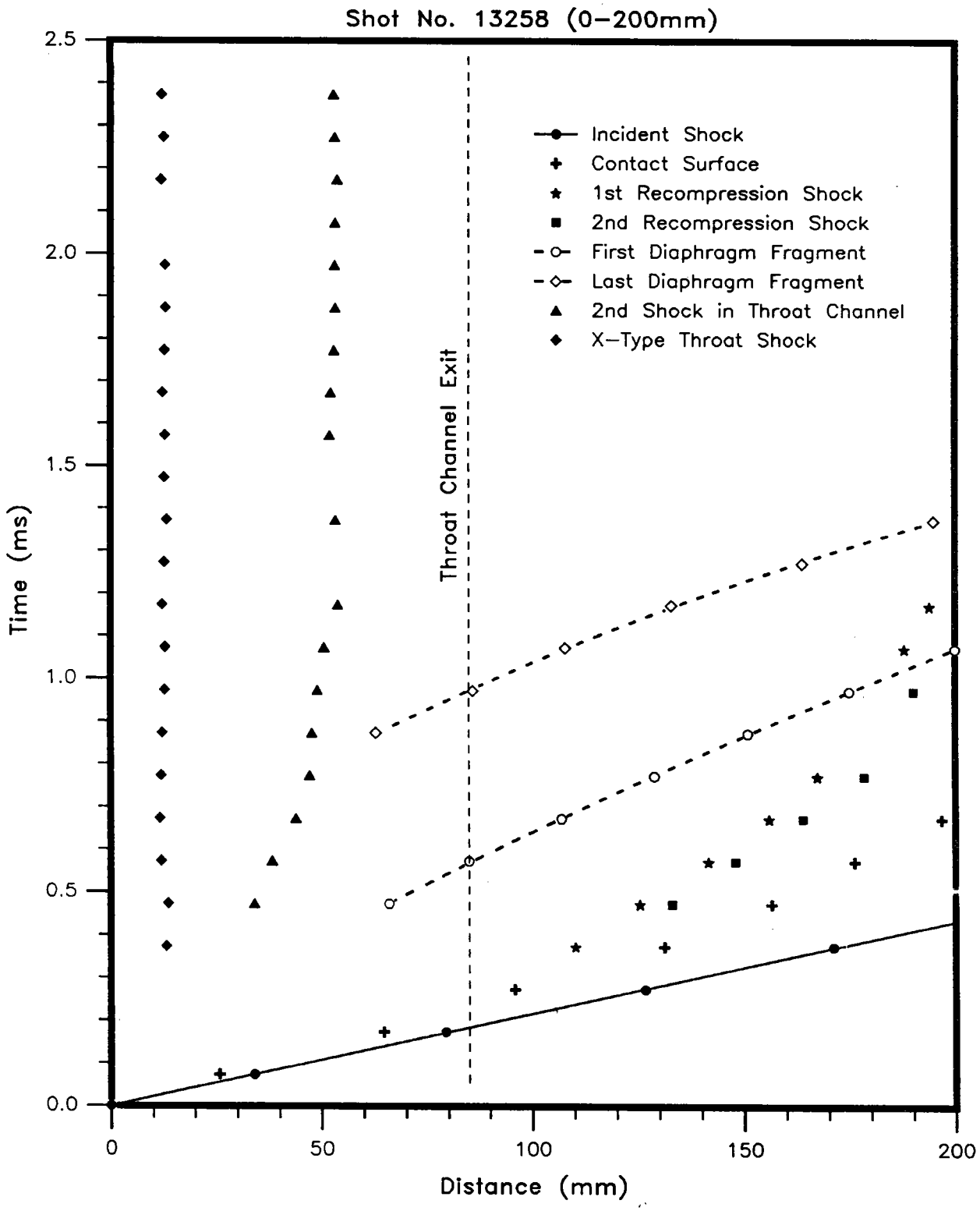

Figure A-23. 90° Nozzle at P_{41}= 14

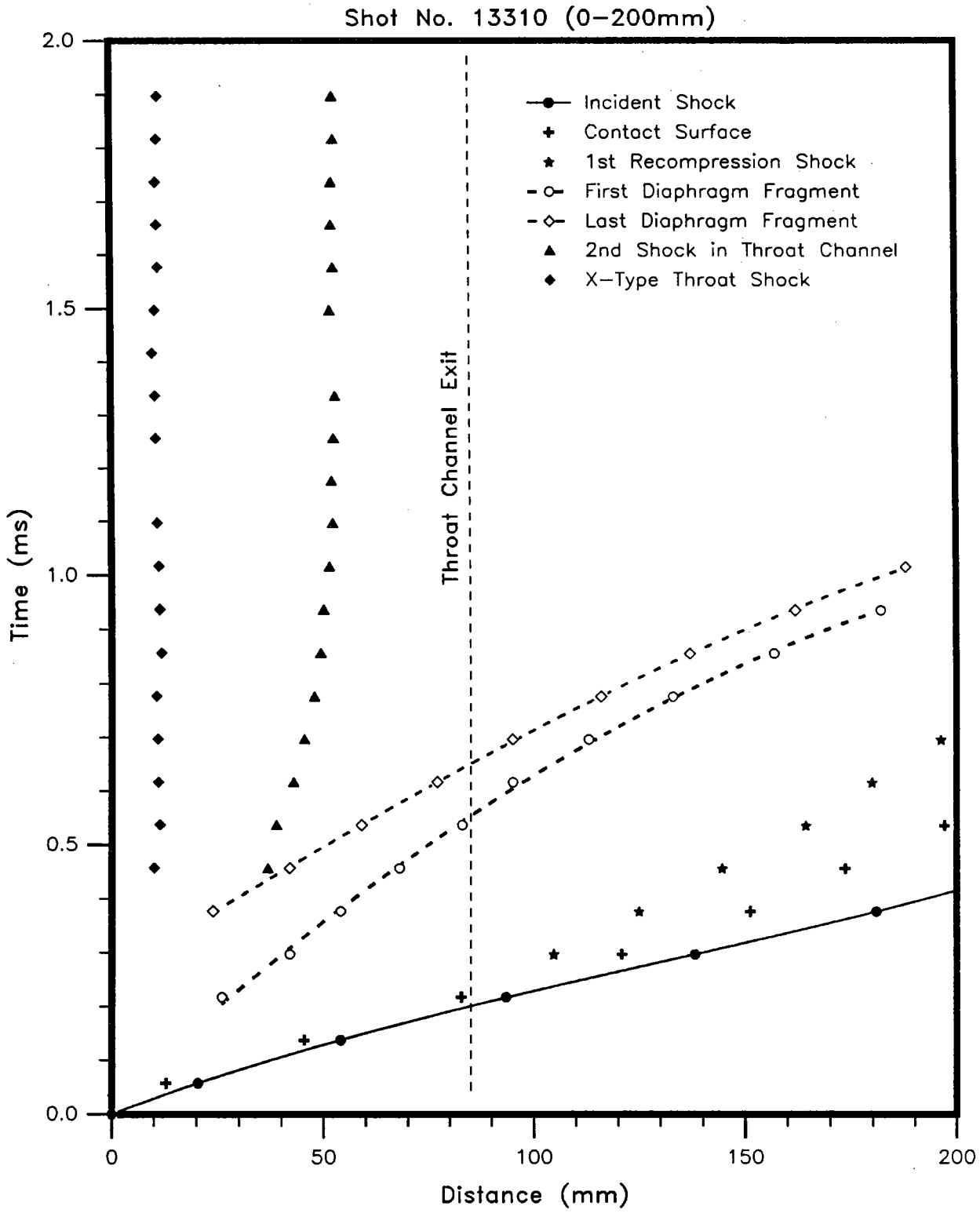

Figure A–24: 90° Nozzle at P_{41}=38.

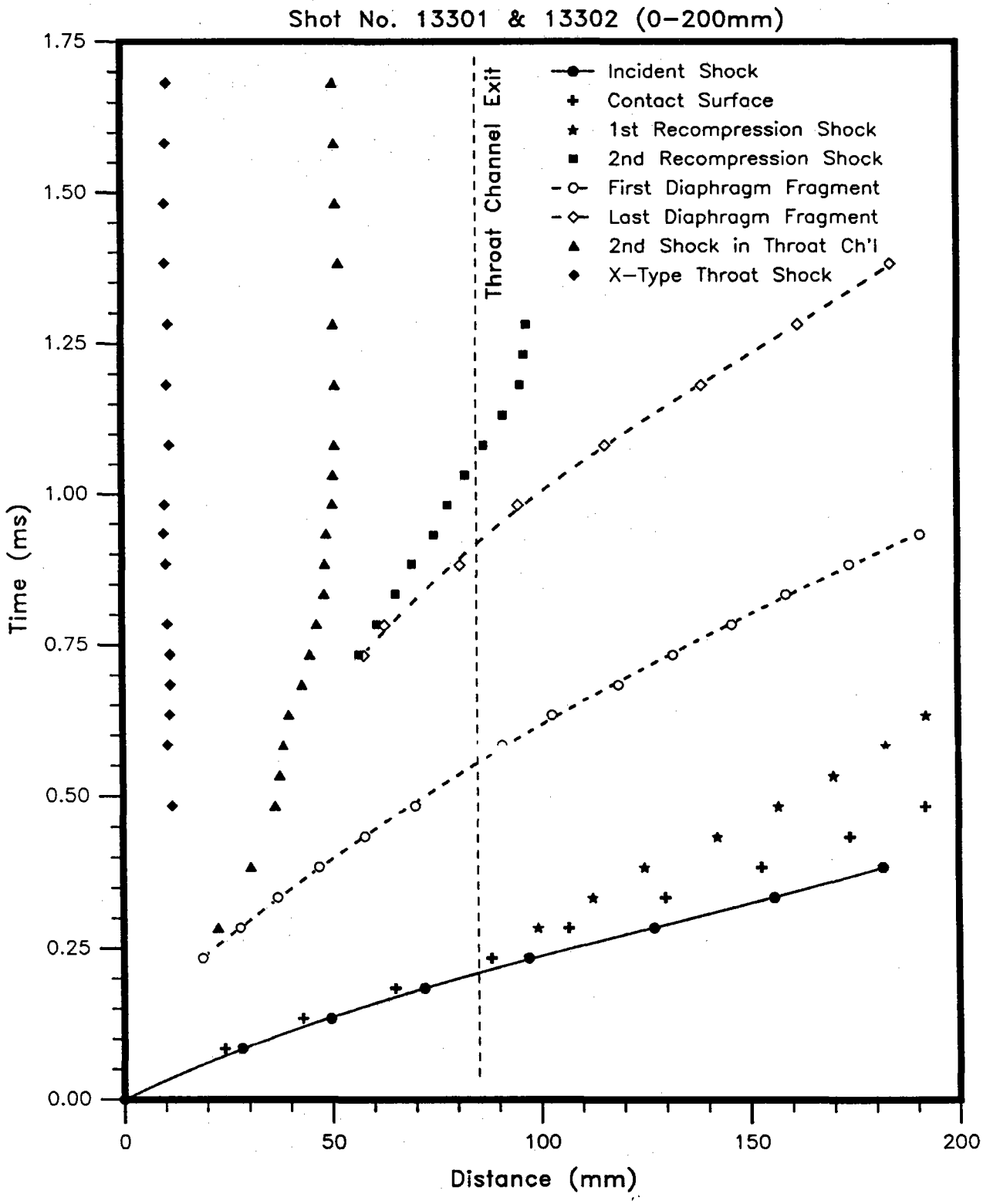

Figure A-25. 90° Nozzle at P_{41}= 55

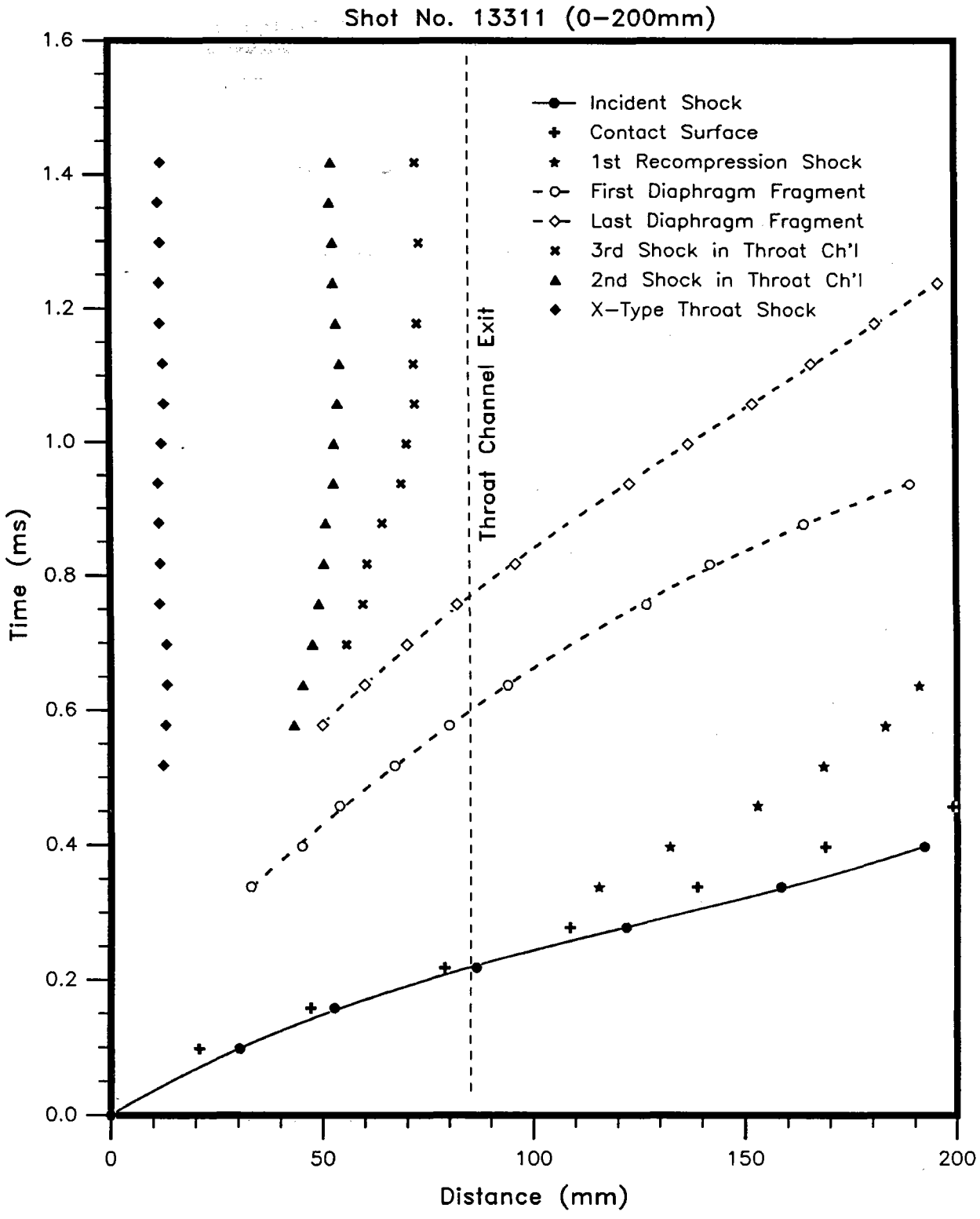

Figure A-26: 90° Nozzle at P_{41}=80.

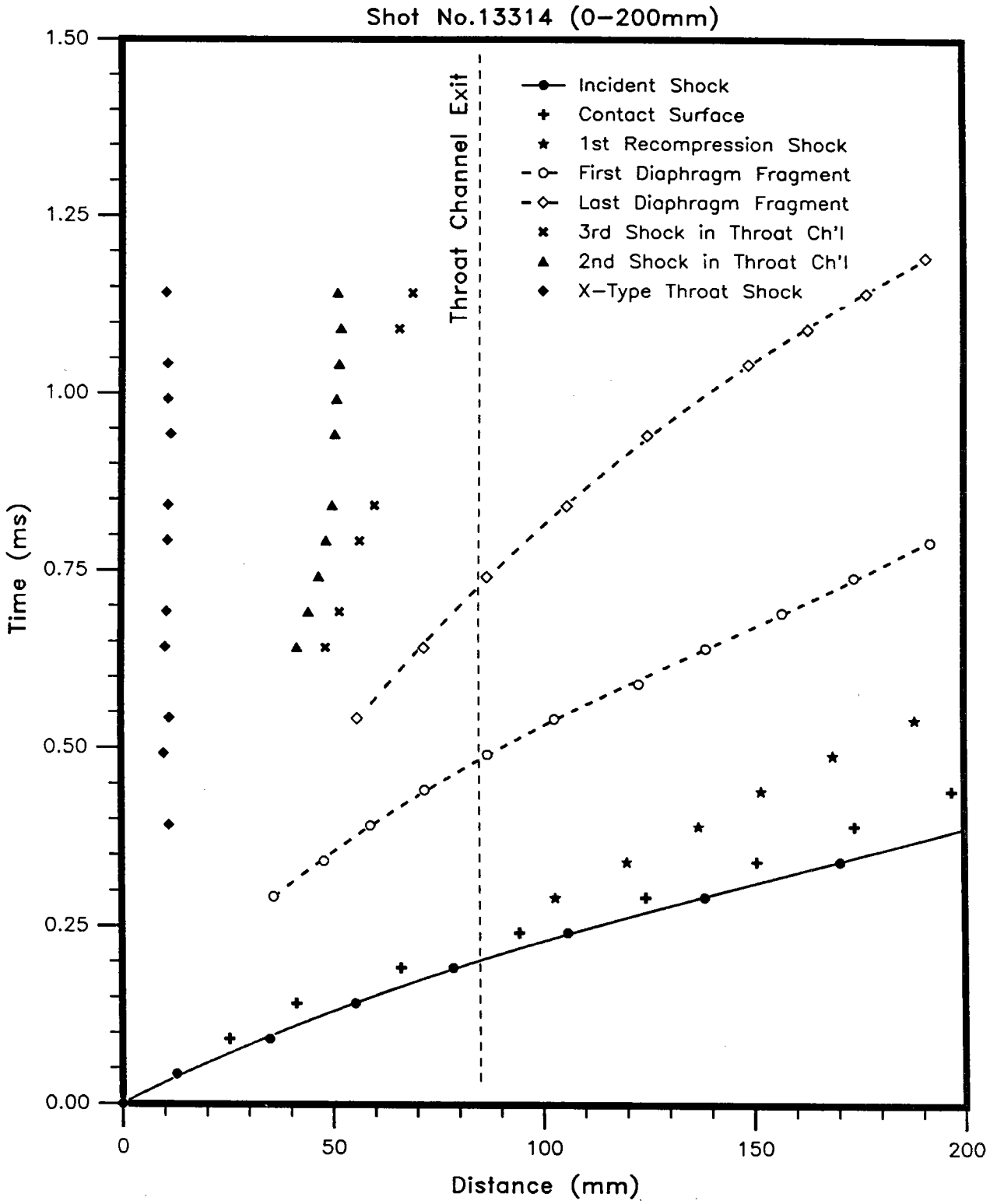

Figure A-27: 90° Nozzle at P_{41}=110.

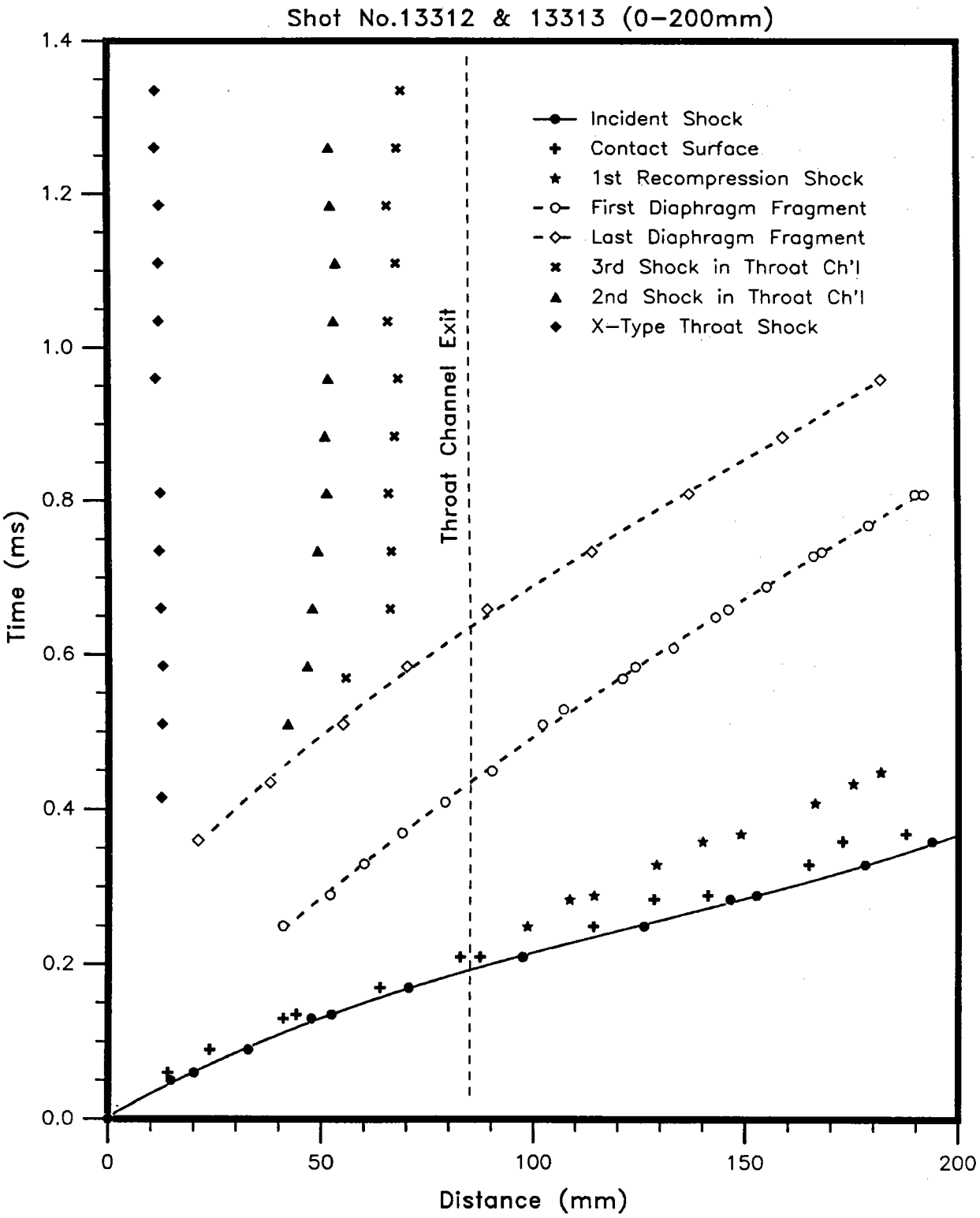

Figure A-28: 90° Nozzle at P_{41}=188.

APPENDIX B: X-t DIAGRAMS WITH Q1D COMPARISONS

(intentionally left blank)

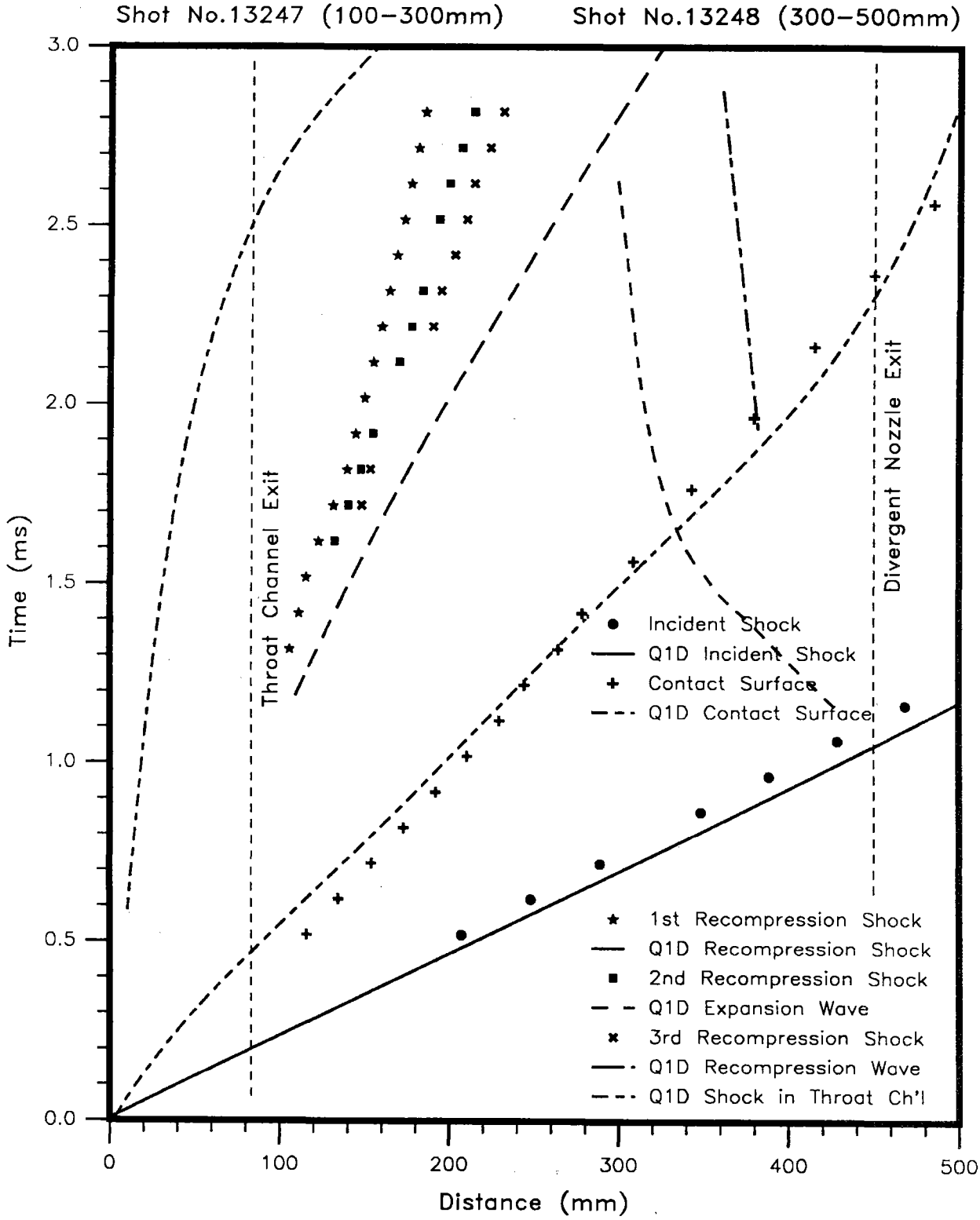

Figure B–1: Case N06/004

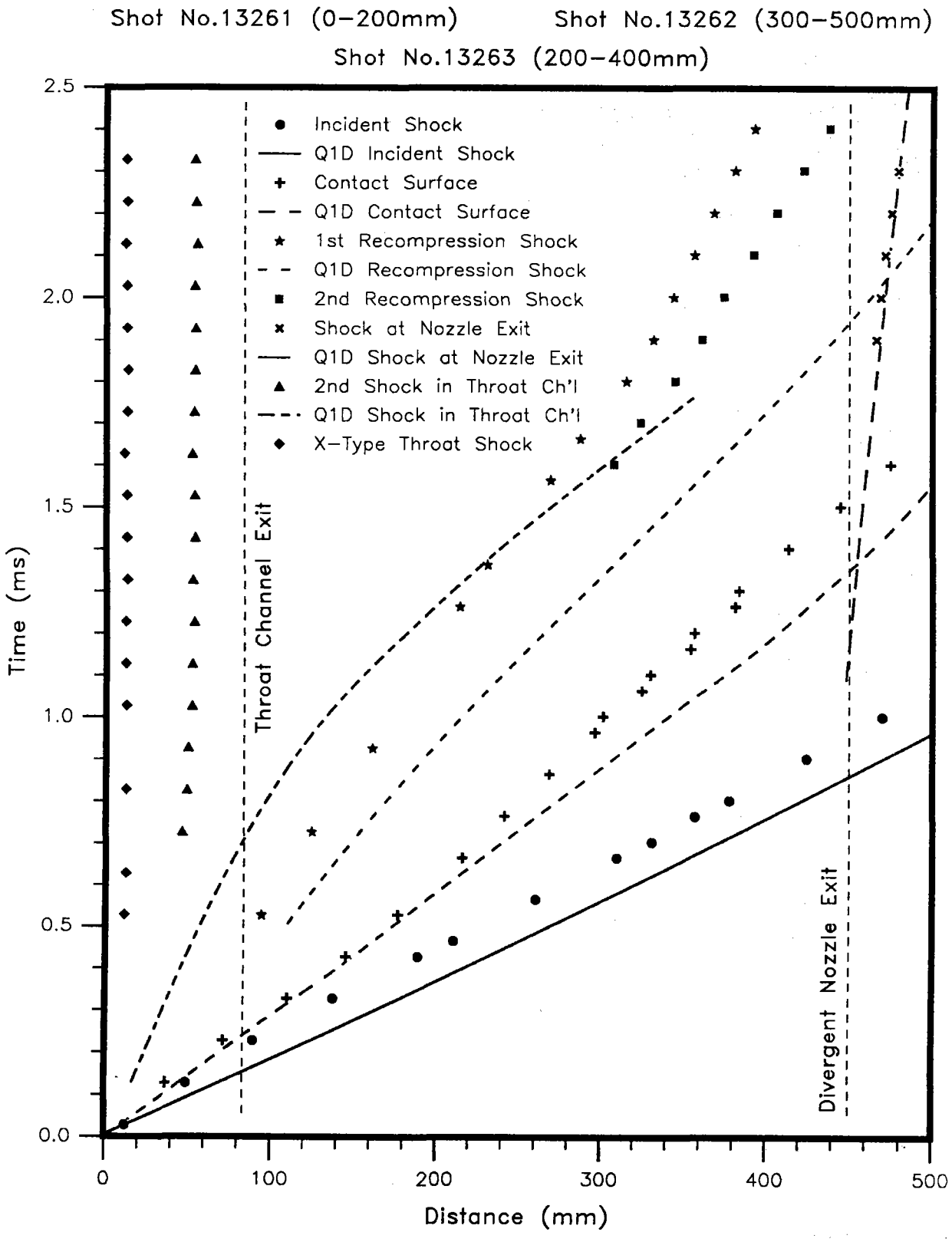

Figure B–2: Case N06/014

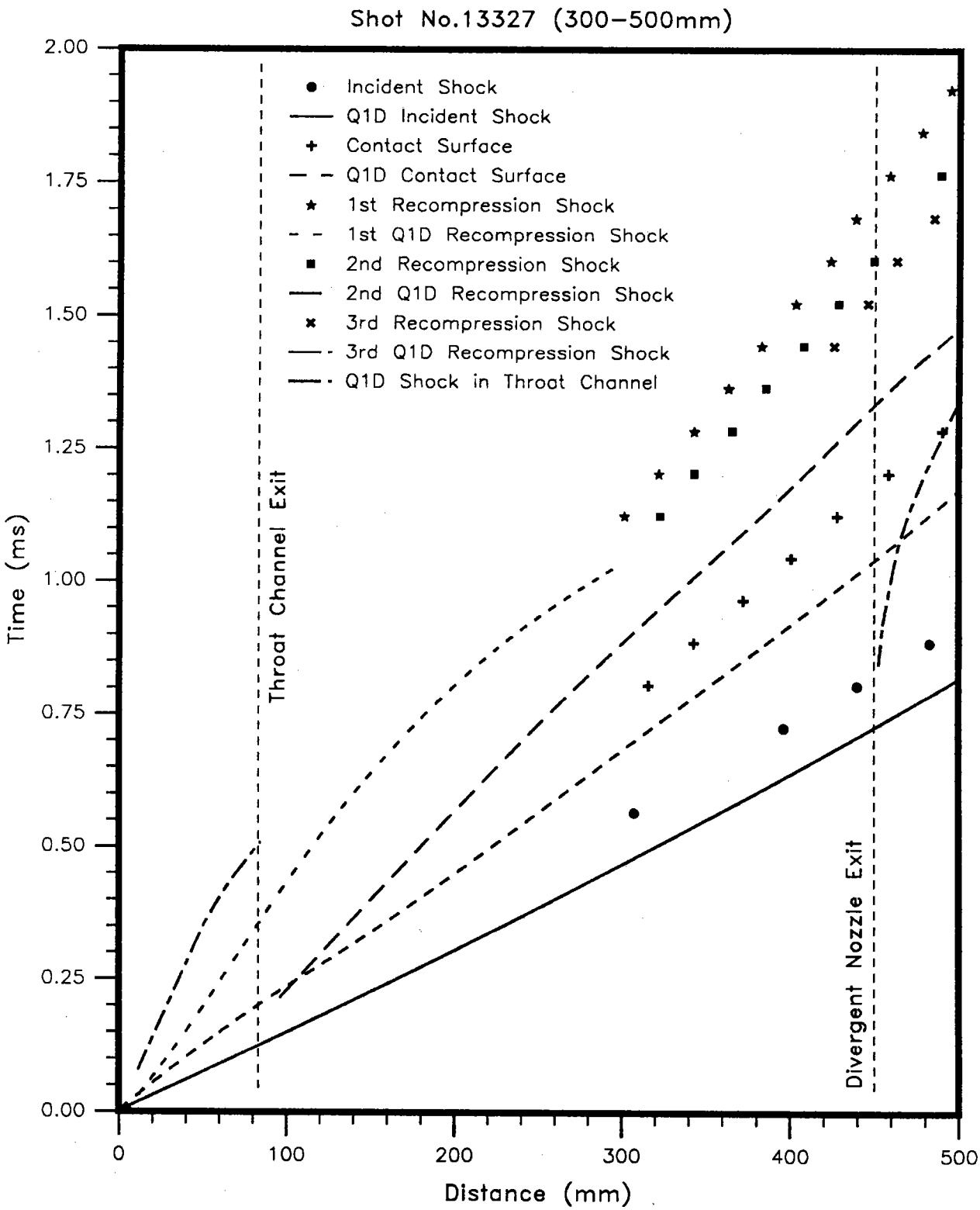

Figure B–3: Case N06/038

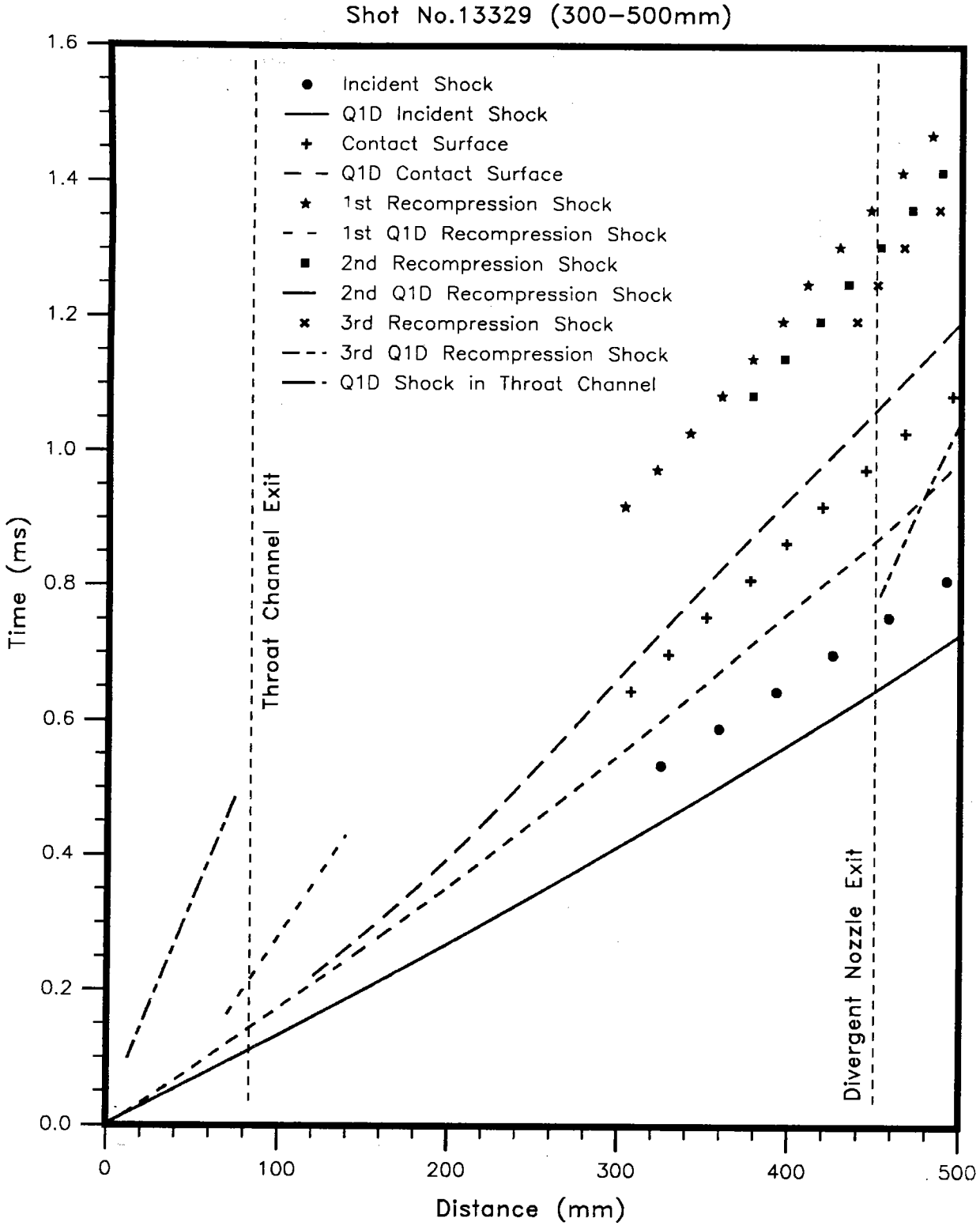

Figure B–4: Case N06/080

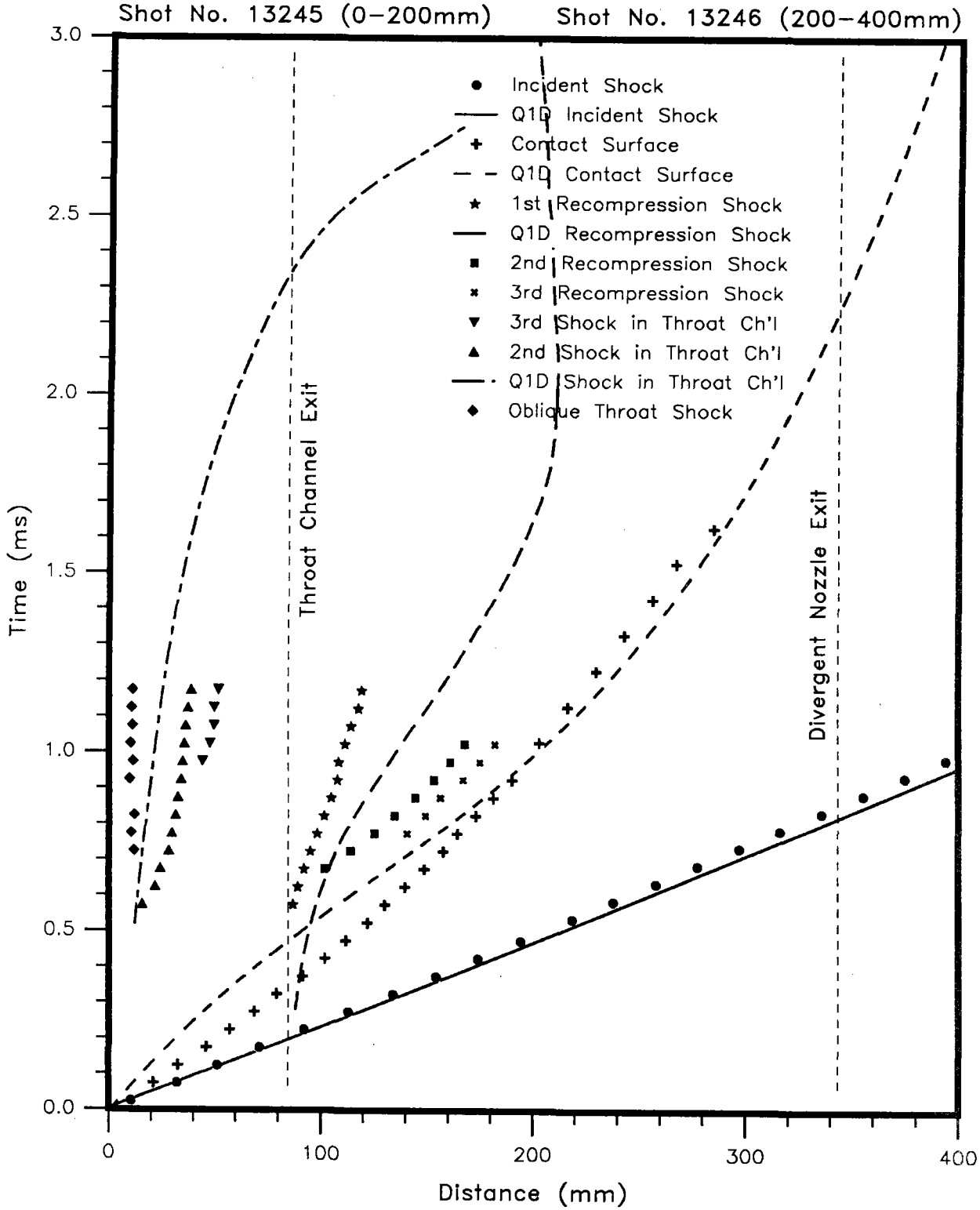

Figure B–5: Case N16/004

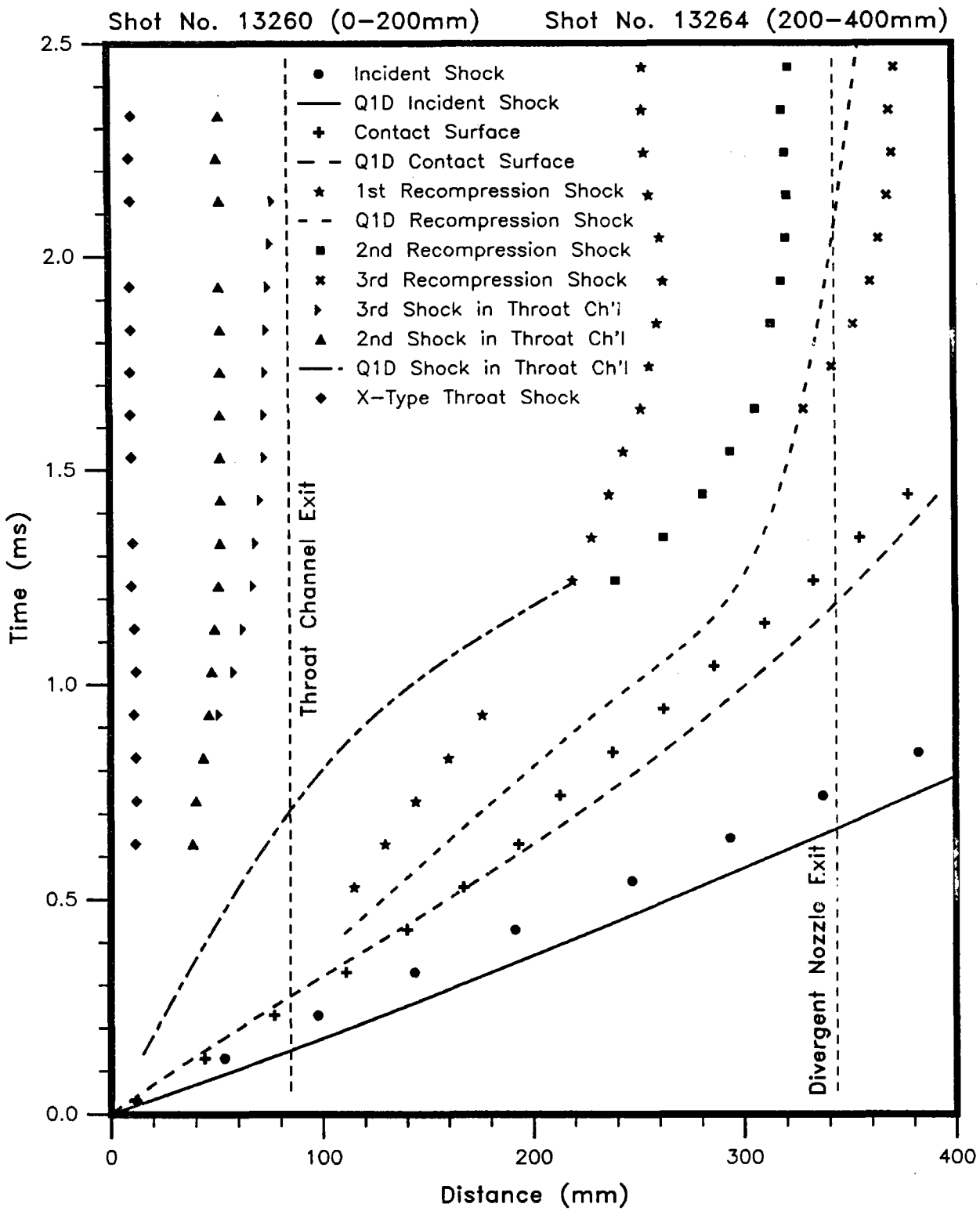

Figure B–6: Case N16/014.

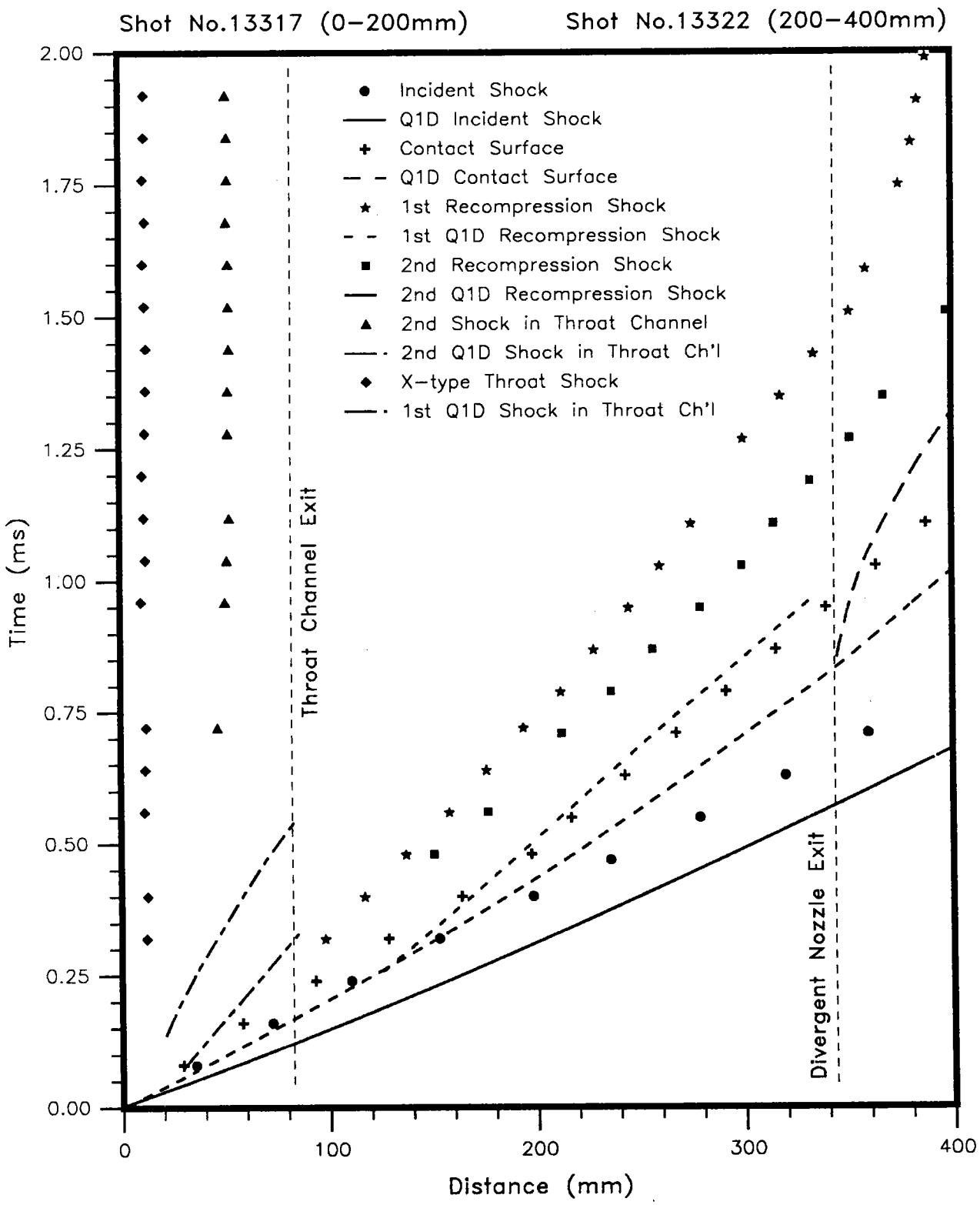

Figure B–7: Case N16/038

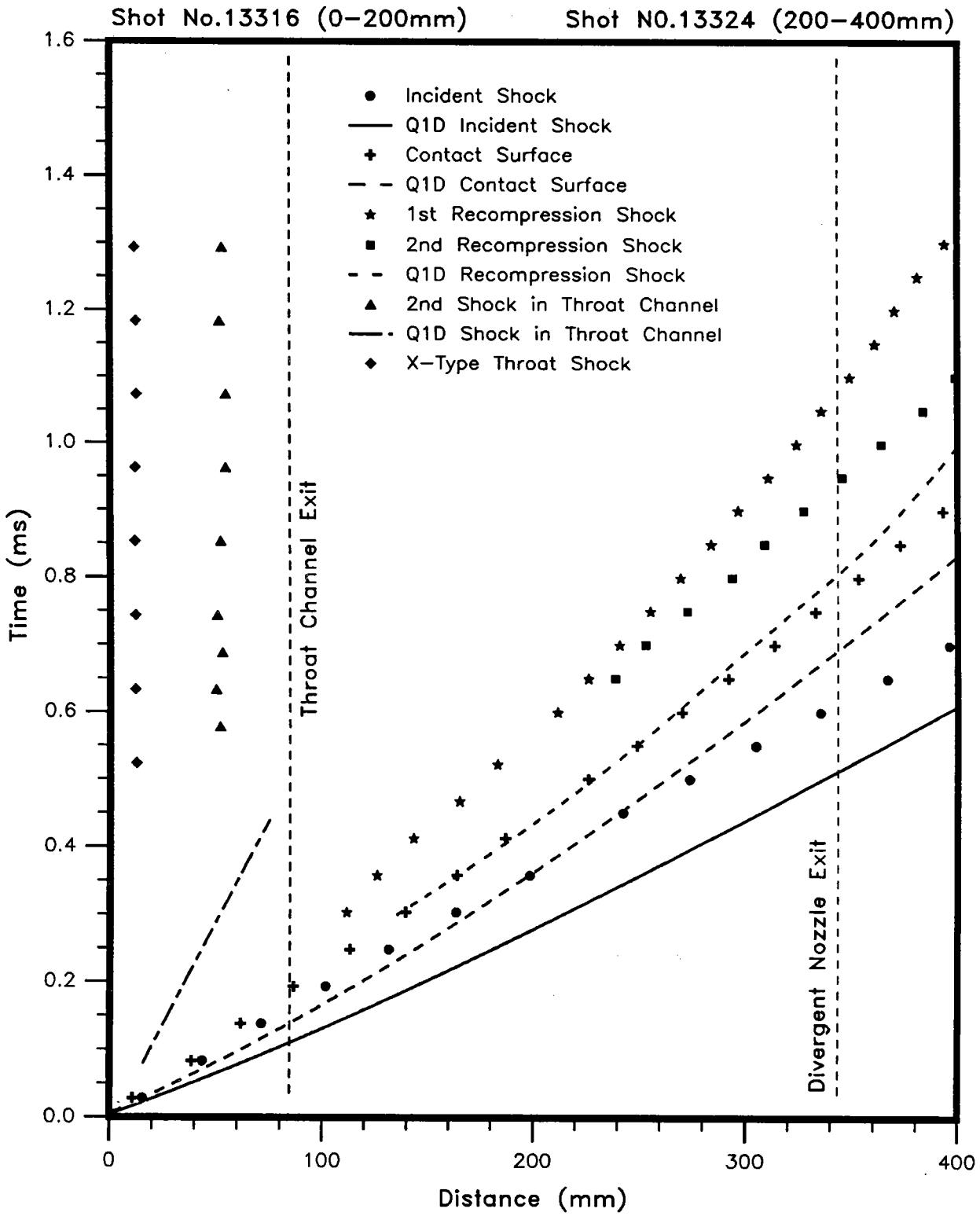

Figure B-8: Case N16/080.

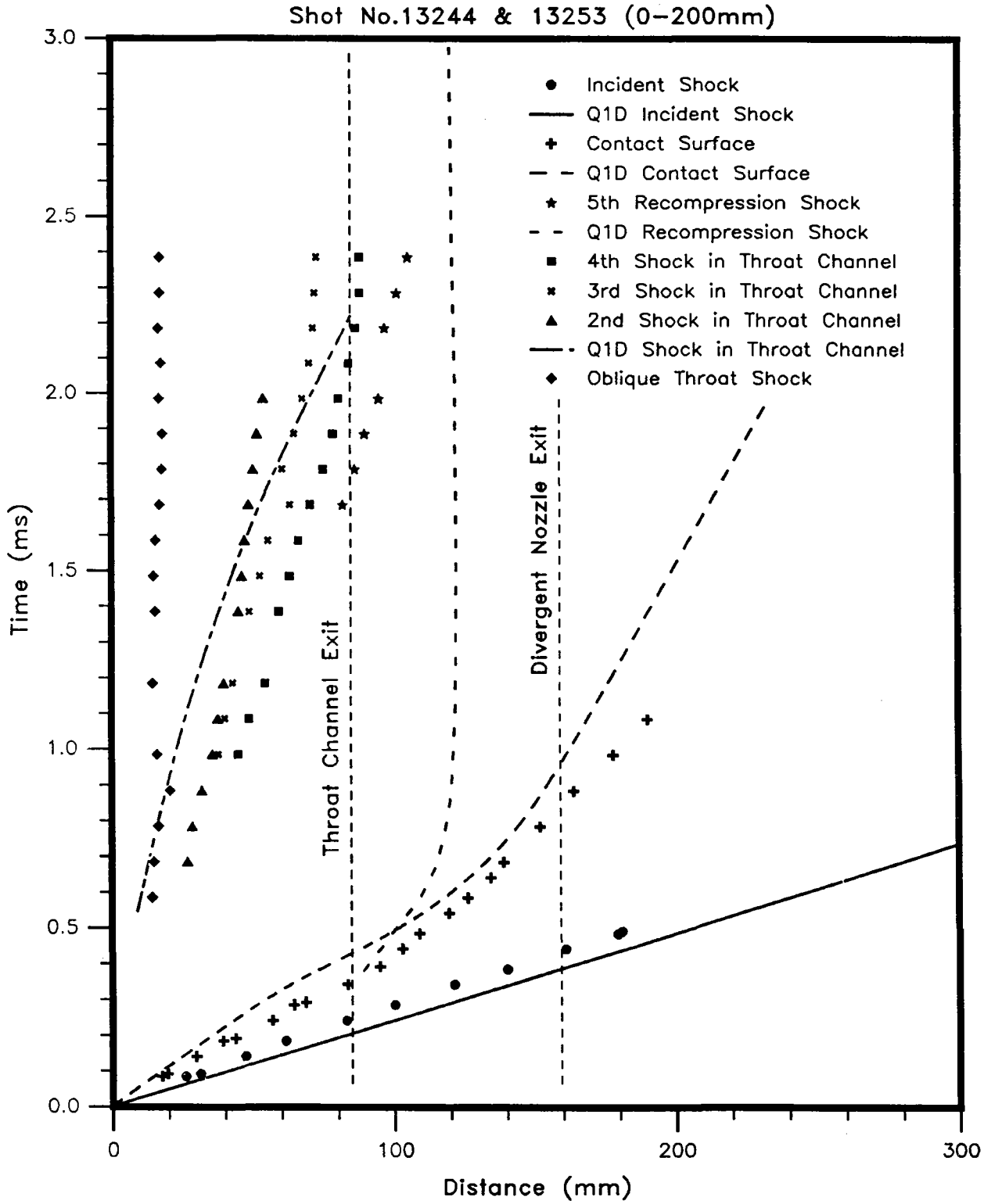

Figure B-9: Case N45/004.

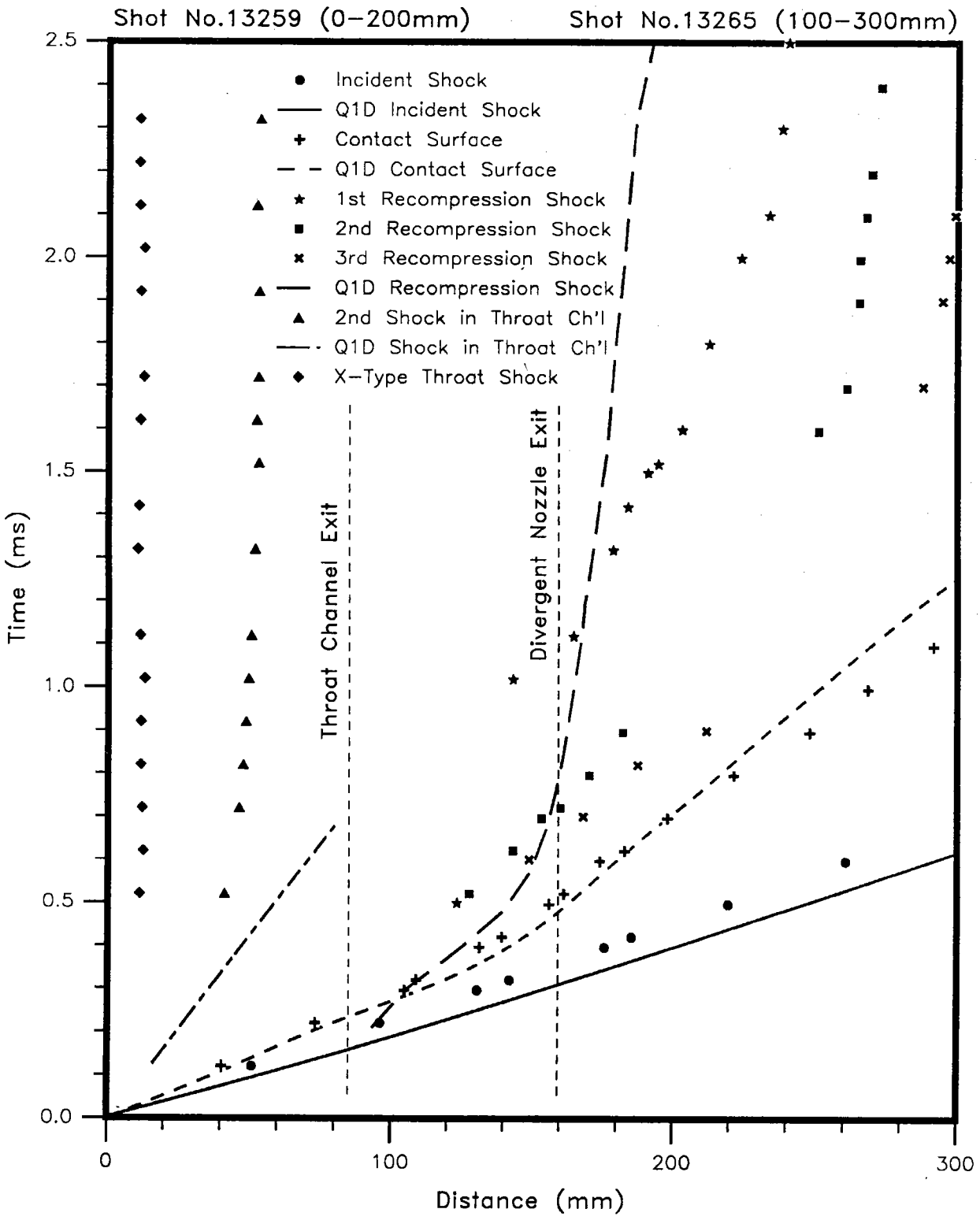

Figure B–10: Case N45/014

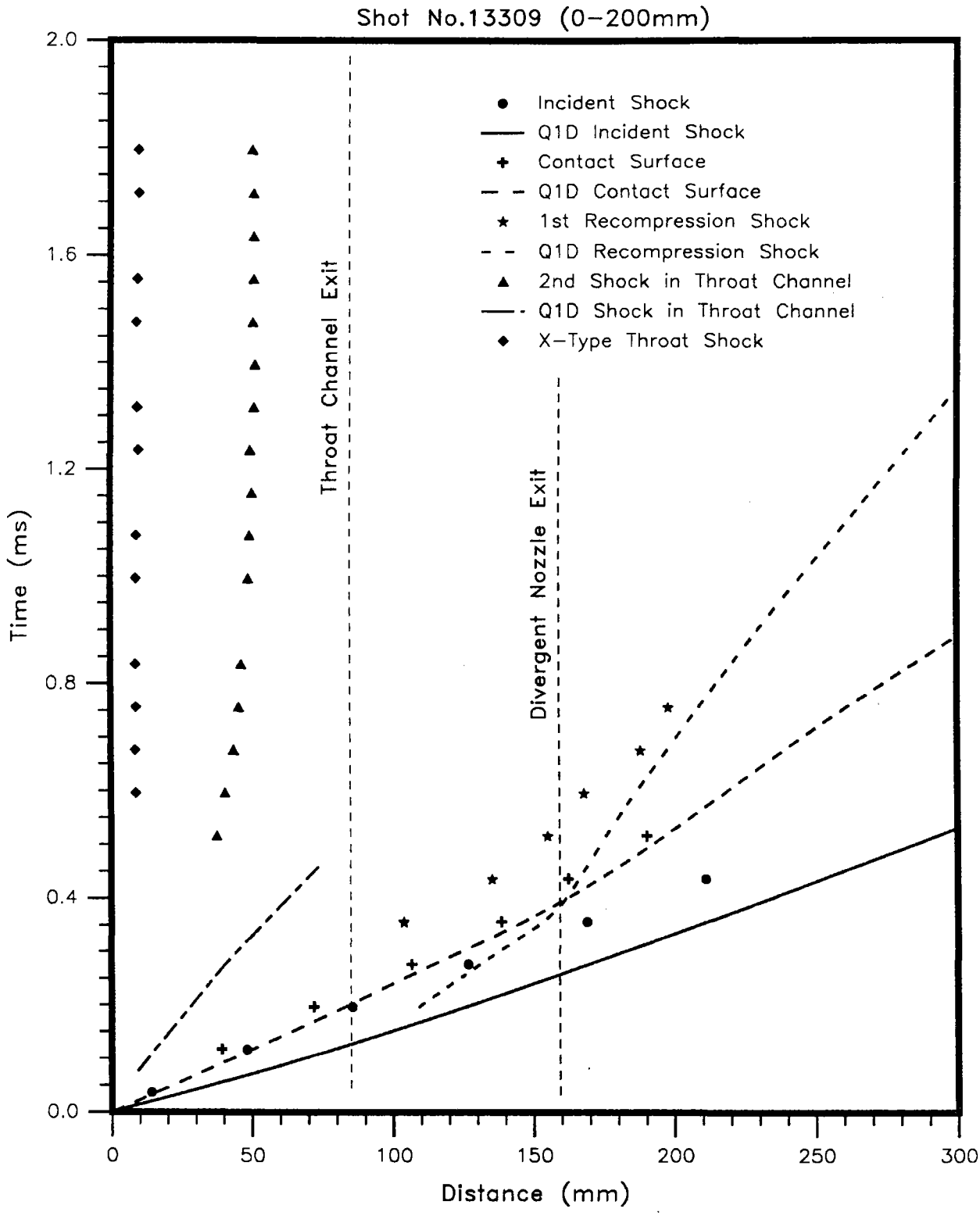

Figure B-11: Case N45/038

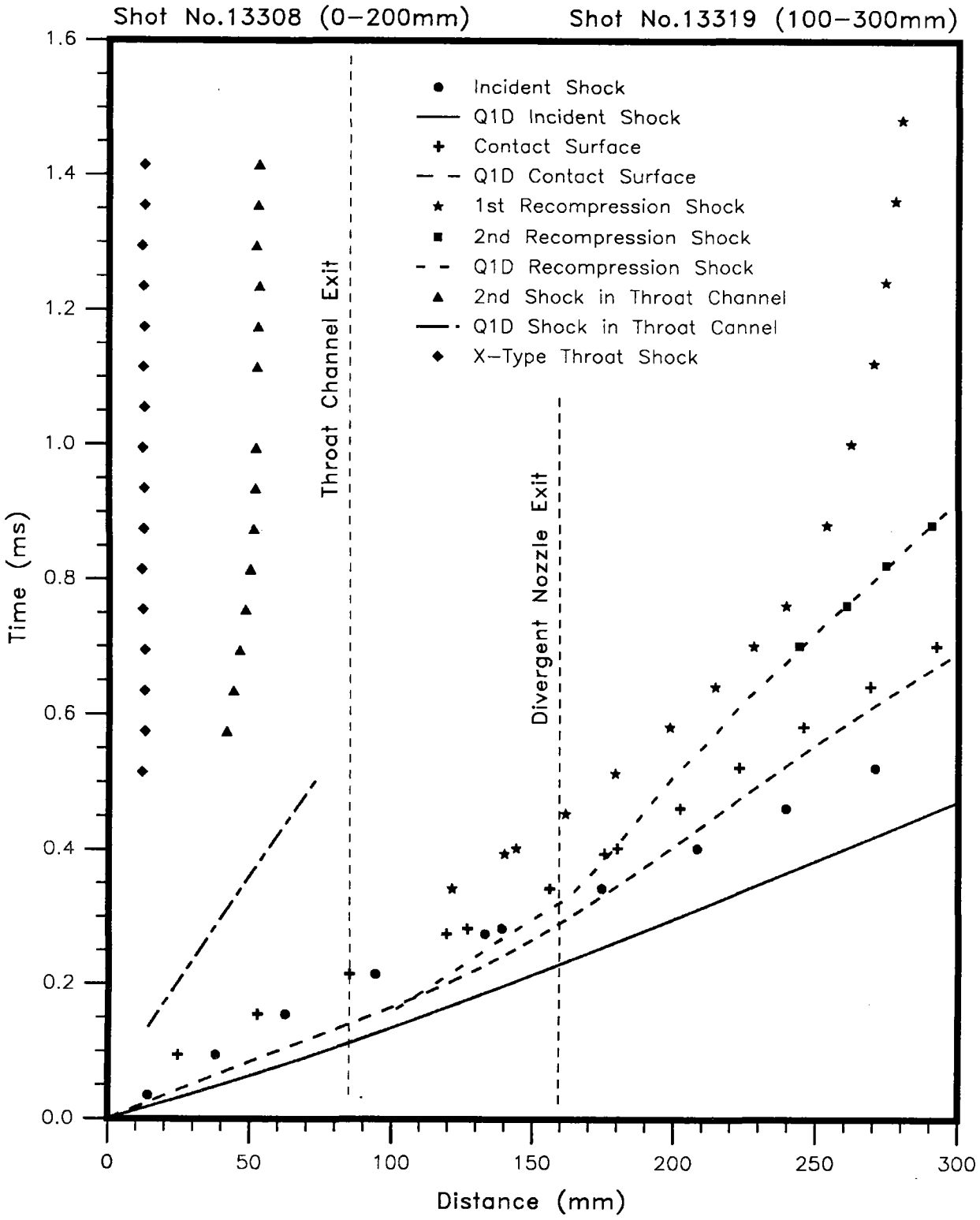

Figure B-12: Case N45/080

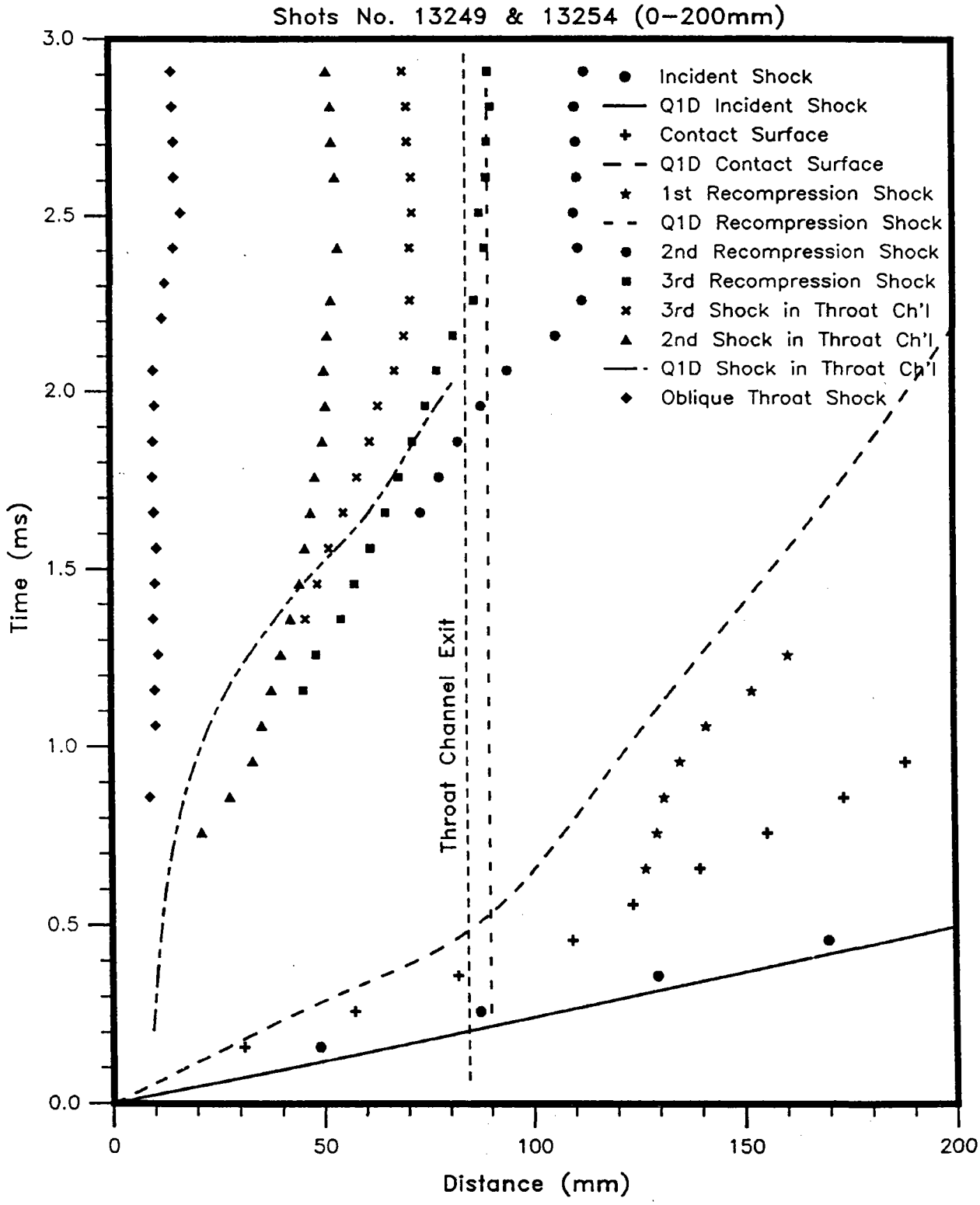

Figure B-13: Case N90/004

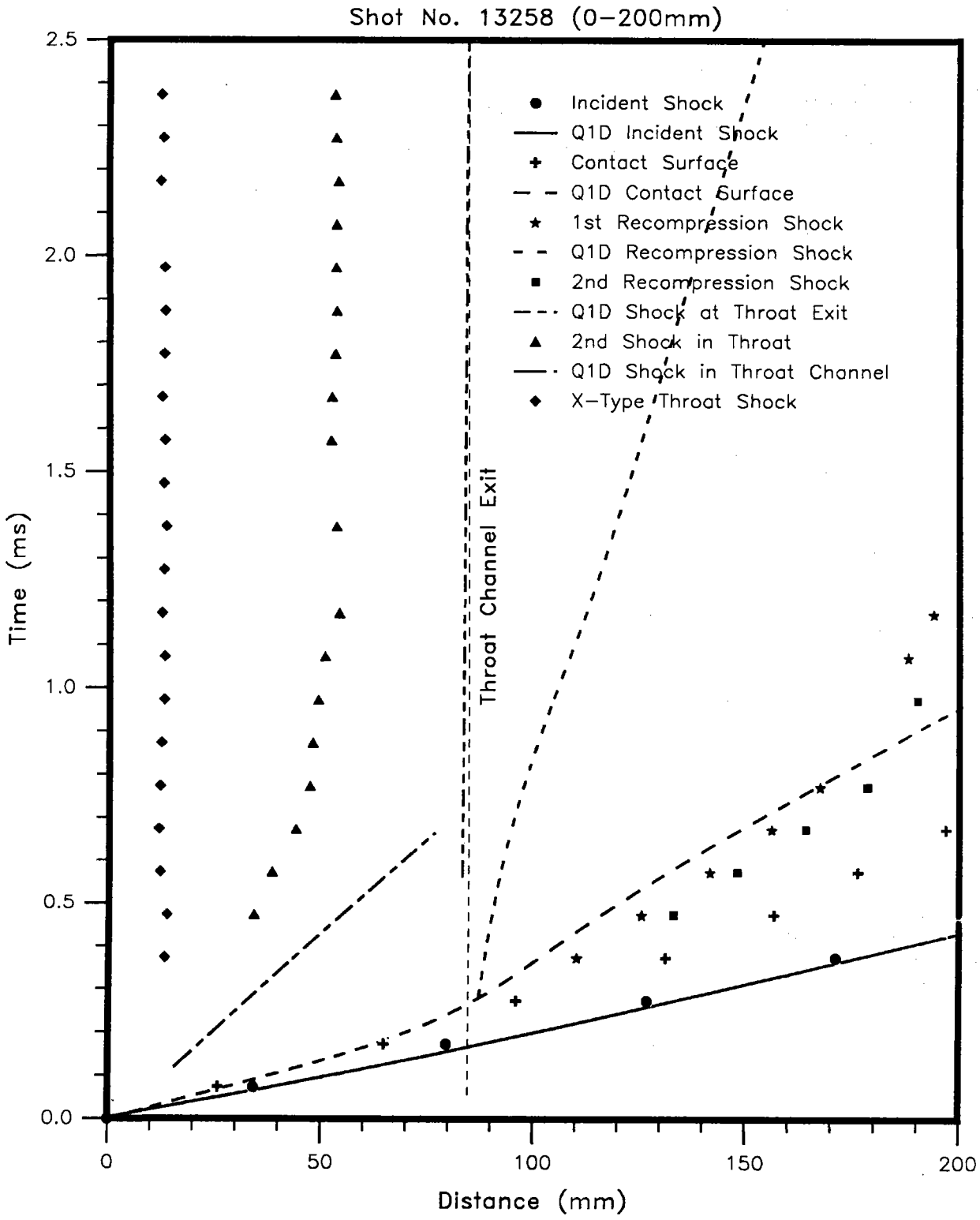

Figure B–14: Case N90/014

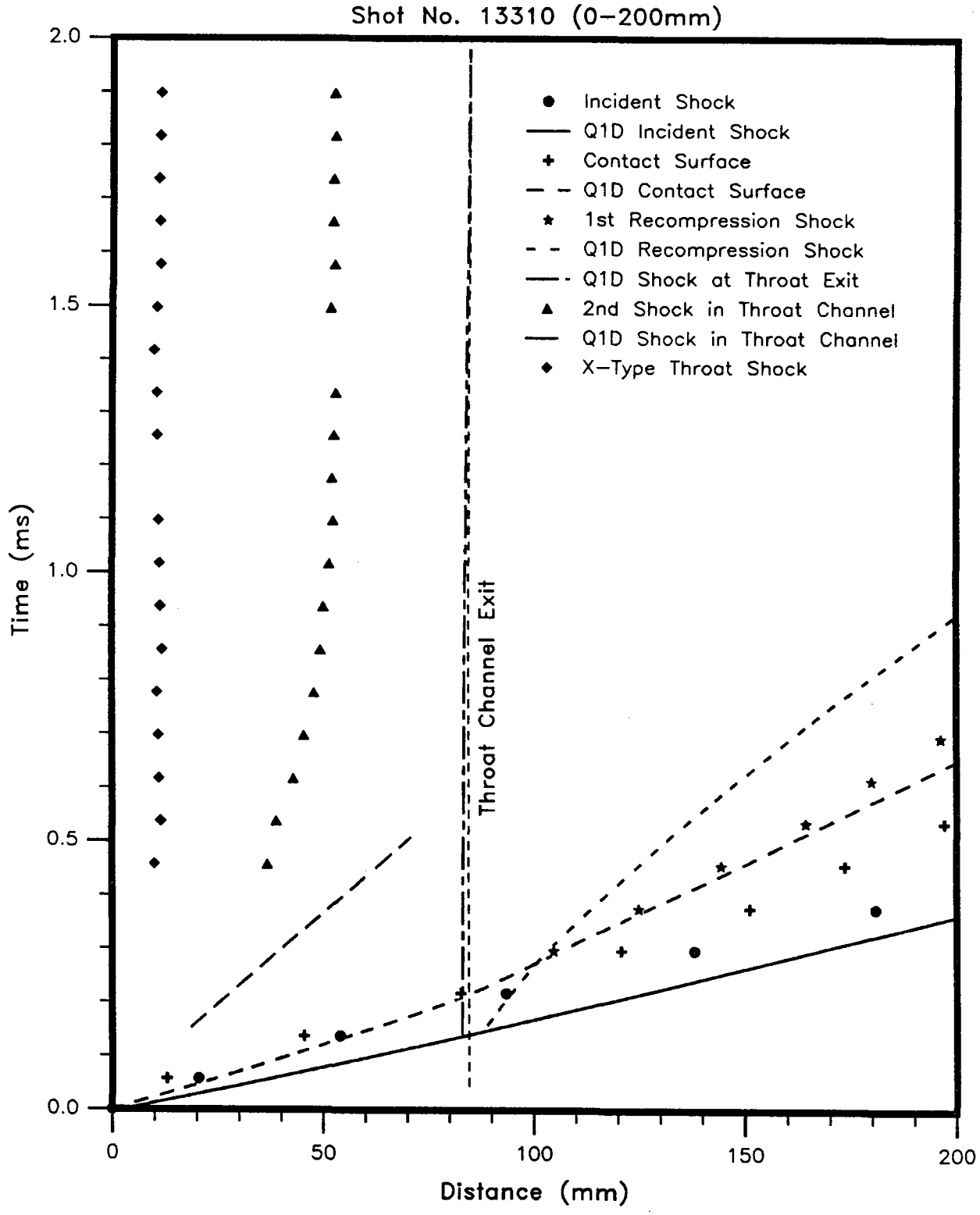

Figure B–15: Case N90/038.

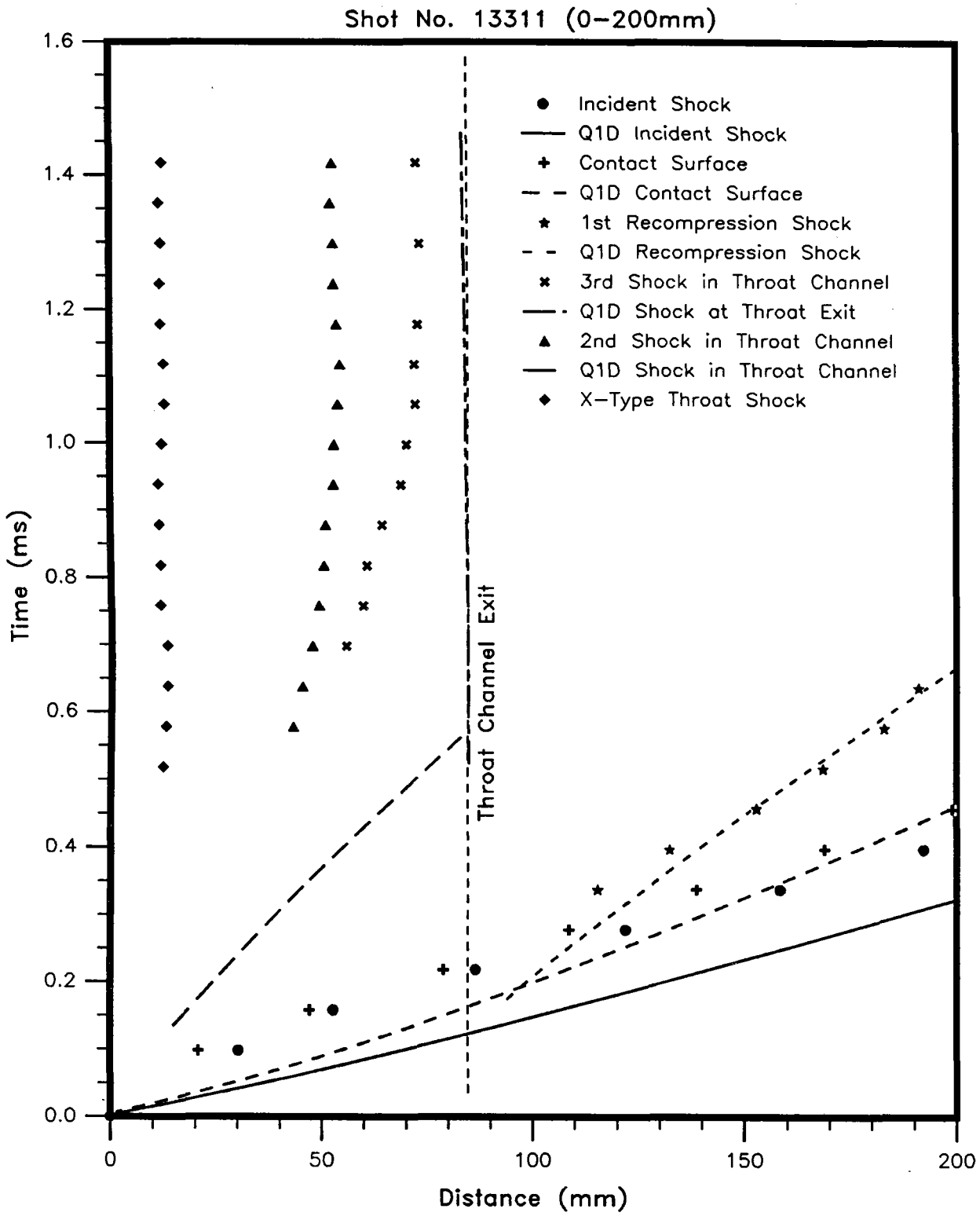

Figure B-16: Case N90/080.

No of Copies	Organization
2	Administrator Defense Technical Info Center ATTN: DTIC-DDA Cameron Station Alexandria, VA 22304-6145
1	HQDA (SARD-TR) WASH DC 20310-0001
1	Commander U.S. Army Materiel Command ATTN: AMCDRA-ST 5001 Eisenhower Avenue Alexandria, VA 22333-0001
1	Commander U.S. Army Laboratory Command ATTN: AMSLC-DL 2800 Powder Mill Road Adelphi, MD 20783-1145
2	Commander U.S. Army Armament Research, Development, and Engineering Center ATTN: SMCAR-IMI-I Picatinny Arsenal, NJ 07806-5000
2	Commander U.S. Army Armament Research, Development, and Engineering Center ATTN: SMCAR-TDC Picatinny Arsenal, NJ 07806-5000
1	Director Benet Weapons Laboratory U.S. Army Armament Research, Development, and Engineering Center ATTN: SMCAR-CCB-TL Watervliet, NY 12189-4050
1	Commander U.S. Army Armament, Munitions and Chemical Command ATTN: SMCAR-ESP-L Rock Island, IL 61299-5000
1	Director U.S. Army Aviation Research and Technology Activity ATTN: SAVRT-R (Library) M/S 219-3 Ames Research Center Moffett Field, CA 94035-1000

No of Copies	Organization
1	Commander U.S. Army Missile Command ATTN: AMSMI-RD-CS-R (DOC) Redstone Arsenal, AL 35898-5010
1	Commander U.S. Army Tank-Automotive Command ATTN: AMSTA-TSL (Technical Library) Warren, MI 48397-5000
1	Director U.S. Army TRADOC Analysis Command ATTN: ATRC-WSR White Sands Missile Range, NM 88002-5502
(Class. only)†	Commandant U.S. Army Infantry School ATTN: ATSH-CD (Security Mgr.) Fort Benning, GA 31905-5660
(Unclass. only)†	Commandant U.S. Army Infantry School ATTN: ATSH-CD-CSO-OR Fort Benning, GA 31905-5660
1	Air Force Armament Laboratory ATTN: AFATL/DLODL Eglin AFB, FL 32542-5000
	Aberdeen Proving Ground
2	Dir, USAMSAA ATTN: AMXSY-D AMXSY-MP, H. Cohen
1	Cdr, USATECOM ATTN: AMSTE-TD
3	Cdr, CRDEC, AMCCOM ATTN: SMCCR-RSP-A SMCCR-MU SMCCR-MSI
1	Dir, VLAMO ATTN: AMSLC-VL-D
10	Dir, BRL ATTN: SLCBR-DD-T

No. of Copies | Organization

1 Director of Defense Research & Engineering
ATTN: DD/TWP
Washington, DC 20301

1 Assistant Secretary of Defense (Atomic Energy)
ATTN: Document Control
Washington, DC 20301

1 Chairman
Joint Chiefs of Staff
ATTN: J-5, R&D Division
Washington, DC 20301

2 Deputy Chief of Staff for Operations and Plans
ATTN: Technical Library
Director of Chemical and Nuclear Operations
Department of the Army
Washington, DC 20310

1 European Research Office
USARDSG (UK)
ATTN: Dr. R. Reichenbach
Box 65
FPO New York 09510-1500

1 Director
Defense Advanced Research Projects Agency
ATTN: Tech Lib
1400 Wilson Boulevard
Arlington, VA 22209

2 Director
Federal Emergency Management Agency
ATTN: Public Relations Office
Technical Library
Washington, DC 20472

1 Chairman
DOD Explosives Safety Board
Room 856-C
Hoffman Bldg. 1
2461 Eisenhower Avenue
Alexandria, VA 22331-0600

No. of Copies | Organization

1 Director
Defense Intelligence Agency
ATTN: DT-2/Wpns & Sys Div
Washington, DC 20301

1 Director
National Security Agency
ATTN: R15, E. F. Butala
Ft. George G. Meade, MD 20755

7 Director
Defense Nuclear Agency
ATTN: CSTI, Tech Lib
DDIR
DFSP, Ullrich
NANS
OPNA
SPSD
SPTD
Washington, DC 20305

3 Commander
Field Command, DNA
ATTN: FCPR
FCTMOF
NMHE, CDR Lund
Kirtland AFB, NM 87115

10 Central Intelligence Agency
DIR/DB/Standard
ATTN: GE-47 HQ
Washington, DC 20505

5 Director
US Army Harry Diamond Laboratories
ATTN: SLCHD-NW-RA,
L. Belliveau
SLCHD-NW-P,
Patnaik
Abe
Corrigan
SLCHD-TA-L, Tech Lib
2800 Powder Mill Road
Adelphi, MD 20783-1197

2 Commander, USACECOM
ATTN: AMSEL-RD
AMSEL-RO-TPPO-P
Fort Monmouth, NJ 07703-5301

No. of Copies | Organization

1 Commander, USACECOM
R&D Technical Library
ATTN: ASQNC-ELC-I-T, Myer Center
Fort Monmouth, NJ 07703-5301

1 Director
US Army Missile and Space Intelligence Center
ATTN: AIAMS-YDL
Redstone Arsenal, AL 35898-5500

1 Commander
US Army Foreign Science and Technology Center
ATTN: Research & Data Branch
220 7th Street, NE
Charlottesville, VA 22901

1 Director
US Army TRAC - Ft. Lee
ATTN: ATRC-L, R. Cameron
Fort Lee, VA 23801-6140

1 Commander
US Army Materials Technology Laboratory
ATTN: AMXMR-ATL
Watertown, MA 02172-0001

2 Commander
US Army Strategic Defense Command
ATTN: CSSD-H-MPL, Tech Lib
CSSD-H-XM, Dr. Davies
PO Box 1500
Huntsville, AL 35807

2 Commander
US Army Natick Research and Development Center
ATTN: AMDNA-D, Dr. D. Sieling
STRNC-UE, J. Calligeros
Natick, MA 01762

1 Commander
US Army Engineer Division
ATTN: HNDED-FD
PO Box 1500
Huntsville, AL 35807

No. of Copies | Organization

3 Commander
US Army Corps of Engineers
Waterways Experiment Station
ATTN: CAWES-SS-R, J. Watt
CAWES-SE-R, J. Ingram
CAWES-TL, Tech Lib
PO Box 631
Vicksburg, MS 39180-0631

1 Commander
US Army Corps of Engineers
Fort Worth District
ATTN: CESWF-PM-J,
R. Timmermins
P.O. Box 17300
Forth Worth, TX 76102-0300

1 Commander
US Army Research Office
ATTN: SLCRO-D
PO Box 12211
Research Triangle Park, NC 27709-2211

3 Commander
US Army Nuclear & Chemical Agency
ATTN: ACTA-NAW
MONA-WE
Tech Lib
7500 Backlick Rd., Bldg. 2073
Springfield, VA 22150

1 Director
HQ, TRAC RPD
ATTN: ATRC-RPR, Mr. Radda
Fort Monroe, VA 23651-5143

1 Director
TRAC-WSMR
ATTN: ATRC-WC, Mr. Kirby
White Sands Missile Range, NM 88002-5502

1 Director
TRAC-FLVN
ATTN: ATRC
Fort Leavenworth, KS 66027-5200

No. of Copies | Organization

1 Commander
US Army Test & Evaluation Command
Nuclear Effects Laboratory
ATTN: STEWS-TE-NO,
Dr. J. L. Meason
PO Box 477
White Sands Missile Range, NM 88002

2 Chief of Naval Operations
ATTN: OP-03EG
OP-985F
Department of the Navy
Washington, DC 20350

1 Director
Strategic Systems Projects Office
ATTN: NSP-43, Tech Library
Department of the Navy
Washington, DC 20360

1 Commander
Naval Electronic Systems Command
ATTN: PME 117-21A
Washington, DC 20360

1 Commander
Naval Facilities Engineering Command
ATTN: Technical Library
Washington, DC 20360

1 Commander
Naval Sea Systems Command
ATTN: Code SEA-62R
Department of the Navy
Washington, DC 20362-5101

2 Office of Naval Research
ATTN: Dr. A. Faulstick, Code 23
800 N. Quincy Street
Arlington, VA 22217

1 Officer-in-Charge
Naval Construction Battalion Center
Civil Engineering Laboratory
ATTN: Tech Lib, Code L06C/L08A
Port Hueneme, CA 93041

No. of Copies | Organization

1 Commanding Officer
Naval Civil Engineering Laboratory
ATTN: Code L51, J. Tancreto
Port Hueneme, CA 93043-5003

1 Commander
Naval Surface Warfare Center
ATTN: Code DX-21, Library
Dahlgren, VA 22448-5000

1 Commander (Code 533)
Naval Weapons Center
Tech Library
China Lake, CA 93555-6001

1 Commander
Naval Weapons Evaluation Fac
ATTN: Document Control
Kirtland AFB, NM 87117

1 Commander
Naval Research Laboratory
ATTN: Code 2027, Tech Library
Washington, DC 20375

2 Air Force Armament Laboratory
ATTN: AFATL/DOIL
AFATL/DLYV
Eglin AFB, FL 32542-5000

1 AFESC/RDCS
ATTN: Paul Rosengren
Tyndall AFB, FL 32403

1 RADC (EMTLD/Docu Library)
Griffiss AFB, NY 13441

3 Air Force Weapons Laboratory
ATTN: NTE
NTED
NTES
Kirtland AFB, NM 87117-6008

1 AFIT
ATTN: Tech Lib, Bldg. 640/B
Wright-Patterson AFB, OH 45433

1 AL/LSCF
ATTN: J. Levine
Edwards AFB, CA 93523-5000

No. of Copies	Organization
1	AL/TSTL (Tech. Lib) ATTN: J. Lamb Edwards AFB, CA 93523-5000
1	FTD/NIIS Wright-Patterson AFB, OH 45433
1	US Department of Energy Idaho Operations Office ATTN: Spec Programs, J. Patton 785 DOE Place Idaho Falls, ID 83402
2	Director Idaho National Engineering Laboratory EG&G Idaho Inc. ATTN: Mr. R. Guenzler, MS-3505 Mr. R. Holman, MS-3510 PO Box 1625 Idaho Falls, ID 83415
1	Commander David Taylor Research Center ATTN: Code 522, Tech Info Ctr Bethesda, MD 20084-5000
1	Officer in Charge White Oak Warfare Center Detachment ATTN: Code E232, Tech Library 10901 New Hampshire Avenue Silver Spring, MD 20903-5000
1	Commanding Officer White Oak Warfare Center ATTN: Code WA501, NNPO Silver Spring, MD 20902-5000
1	Director Lawrence Livermore National Laboratory ATTN: Tech Info Dept L-3 PO Box 808 Livermore, CA 94550
1	Director NASA-Langley Research Center ATTN: Tech Lib Hampton, VA 23665
2	Director Los Alamos National Laboratory ATTN: Mr. Th. Dowler, MS-F602 Doc Control for Reports Library PO Box 1663 Los Alamos, NM 87545
3	Director Sandia National Laboratories ATTN: Doc Control 3141 Mr. C. Cameron, Div 6215 Mr. A. Chabai, Div 7112 PO Box 5800 Albuquerque, NM 87185-5800
1	Director Sandia National Laboratories Livermore Laboratory ATTN: Doc Control for Tech Library PO Box 969 Livermore, CA 94550
1	Director National Aeronautics and Space Administration ATTN: Scientific & Tech Info Fac PO Box 8757, BWI Airport Baltimore, MD 21240
1	Director NASA-Ames Research Center Applied Computational Aerodynamics Branch ATTN: Dr. T. Holtz, MS 202-14 Moffett Field, CA 94035
2	Applied Research Associates, Inc. ATTN: N. H. Ethridge J. Keefer PO Box 548 Aberdeen, MD 21001
1	Aerospace Corporation ATTN: Tech Info Services PO Box 92957 Los Angeles, CA 90009

No. of Copies	Organization
1	Agbabian Associates ATTN: M. Agbabian 250 North Nash Street El Segundo, CA 90245
1	Applied Research Associates, Inc. ATTN: R. L. Guice 7114 West Jefferson Ave., Suite 305 Lakewood, CO 80235
1	Black & Veatch, Engineers-Architects ATTN: H. D. Laverentz 1500 Meadow Lake Parkway Kansas City, MO 64114
1	The Boeing Company ATTN: Aerospace Library PO Box 3707 Seattle, WA 98124
1	California Research & Technology, Inc. ATTN: M. Rosenblatt 20943 Devonshire Street Chatsworth, CA 91311
1	Carpenter Research Corporation ATTN: H. Jerry Carpenter 27520 Hawthorne Blvd., Suite 263 PO Box 2490 Rolling Hills Estates, CA 90274
1	Dynamics Technology, Inc. ATTN: D. T. Hove 21311 Hawthorne Blvd., Suite 300 Torrance, CA 90503
1	EATON Corporation Defense Valve & Actuator Div. ATTN: Mr. J. Wada 2338 Alaska Ave. El Segundo, CA 90245-4896
1	Goodyear Aerospace Corporation ATTN: R. M. Brown, Bldg. 1 Shelter Engineering Litchfield Park, AZ 85340

No. of Copies	Organization
1	Alliant Techsystems, Inc. ATTN: Roger A. Rausch (MN48-3700) 7225 Northland Drive Brooklyn Park, MN 55428
4	Kaman AviDyne ATTN: Dr. R. Ruetenik (2 cys) Mr. S. Criscione Mr. R. Milligan 83 Second Avenue Northwest Industrial Park Burlington, MA 01803
3	Kaman Sciences Corporation ATTN: Library P. A. Ellis F. H. Shelton PO Box 7463 Colorado Springs, CO 80933-7463
1	Kaman Sciences Corporation ATTN: Mr. F. W. Balicki 6400 Uptown Boulevard N.E., Suite 300 Albuquerque, NM 87110
2	Kaman-TEMPO ATTN: DASIAC Don Sachs PO Drawer 1479 816 State Street Santa Barbara, CA 93102-1479
1	Lockheed Missiles & Space Co. ATTN: J. J. Murphy Dept. 81-11, Bldg. 154 PO Box 504 Sunnyvale, CA 94086
2	McDonnell Douglas Astronautics Corporation ATTN: Robert W. Halprin K.A. Heinly 5301 Bolsa Avenue Huntington Beach, CA 92647
2	The Ralph M. Parsons Company ATTN: Tyler M. Jackson, LB/TS Project Manager 100 West Walnut Street Pasadena, CA 91124

No. of Copies	Organization
2	R&D Associates ATTN: Technical Library Dr. Allan Kuhl PO Box 9695 Marina Del Rey, CA 90291
1	R&D Associates ATTN: G. P.Ganong PO Box 9377 Albuquerque, NM 87119
3	Science Applications, Inc. ATTN: Division 164, M ST-302 W. Layson John Cockayne PO Box 1303 1710 Goodridge Drive McLean, VA 22102
1	Science Applications International Corp. ATTN: Mr. J. Guest 2301 Yale Blvd. SE, Suite E Albuquerque, NM 87106
1	Science Applications International Corporation ATTN: Mr. N. Sinha 501 Office Center Drive, Apt. 420 Ft. Washington, PA 19034-3211
1	Sparta, Inc. Los Angeles Operations ATTN: I. B. Osofsky 3440 Carson Street Torrance, CA 90503
1	Sverdrup Technology, Inc. ATTN: R. F. Starr PO Box 884 Tullahoma, TN 37388
1	SRI International ATTN: Dr. G. R. Abrahamson 333 Ravenswood Avenue Menlo Park, CA 94025

No. of Copies	Organization
2	S-CUBED A Division of Maxwell Laboratories, Inc. ATTN: C. E. Needham Dr. Lynn Kennedy 2501 Yale Blvd., SE Albuquerque, NM 87106
3	S-CUBED A Division of Maxwell Laboratories, Inc. ATTN: Technical Library R. Duff K. Pyatt PO Box 1620 La Jolla, CA 92037-1620
1	Texas Engineering Experiment Station ATTN: Dr. D. Anderson 301 Engineering Research Center College Station, TX 77843
1	Thermal Science, Inc. ATTN: R. Feldman 2200 Cassens Dr. St. Louis, MO 63026
1	Battelle ATTN: TACTEC Library, J. N. Higgins 505 King Avenue Columbus, OH 43201-2693
1	California Institute of Technology ATTN: T. J. Ahrens 1201 E. California Blvd. Pasadena, Ca 91109
1	Massachusetts Institute of Technology ATTN: Technical Library Cambridge, MA 02139
1	Massachusetts Institute of Technology Aeroelastic and Structures Research Laboratory ATTN: Dr. E. A. Witmer Cambridge, MA 02139

No. of
Copies Organization

2 New Mexico Engineering Research Institute (CERF)
University of New Mexico
ATTN: Dr. J. Leigh
Dr. R. Newell
PO Box 25
Albuquerque, NM 87131

1 Northrop University
ATTN: Dr. F. B. Safford
5800 W. Arbor Vitae St.
Los Angeles, CA 90045

3 Southwest Research Institute
ATTN: C. Anderson
S. Mullin
A. B. Wenzel
PO Drawer 28255
San Antonio, TX 78228-0255

1 State University of New York
Mechanical & Aerospace Engineering
ATTN: Dr. Peyman Givi
Buffalo, NY 14260

2 Denver Research Institute
ATTN: Mr. J. Wisotski
Technical Library
P.O. Box 10758
Denver, CO 80210

1 Stanford University
ATTN: Dr. D. Bershader
Durand Laboratory
Stanford, CA 94305

1 AEDC
ATTN: R. McAmis, Mail Stop 980
Arnold AFB, TN 37389

No. of
Copies Organization

Aberdeen Proving Ground

1 Cdr, USATECOM
ATTN: AMSTE-TE-F, L. Teletski

1 Cdr, USATHMA
ATTN: AMXTH-TE

1 Cdr, USACSTA
ATTN: STECS-LI

No. of
Copies Organization

3 Director
Fraunhofer-Institut für Kurzzeitdynamik
Ernst-Mach-Institut
Eckerstrasse 4
D-7800 Freiburg (Br.)
Germany

(Intentionally left blank)

USER EVALUATION SHEET/CHANGE OF ADDRESS

This Laboratory undertakes a continuing effort to improve the quality of the reports it publishes. Your comments/answers to the items/questions below will aid us in our efforts.

1. BRL Report Number BRL-TR-3215 Date of Report March 1991

2. Date Report Received _____

3. Does this report satisfy a need? (Comment on purpose, related project, or other area of interest for which the report will be used.) _____

4. Specifically, how is the report being used? (Information source, design data, procedure, source of ideas, etc.) _____

5. Has the information in this report led to any quantitative savings as far as man-hours or dollars saved, operating costs avoided, or efficiencies achieved, etc? If so, please elaborate. _____

6. General Comments. What do you think should be changed to improve future reports? (Indicate changes to organization, technical content, format, etc.) _____

CURRENT ADDRESS

Name

Organization

Address

City, State, Zip Code

7. If indicating a Change of Address or Address Correction, please provide the New or Correct Address in Block 6 above and the Old or Incorrect address below.

OLD ADDRESS

Name

Organization

Address

City, State, Zip Code

(Remove this sheet, fold as indicated, staple or tape closed, and mail.)

---FOLD HERE---

DEPARTMENT OF THE ARMY
Director
U.S. Army Ballistic Research Laboratory
ATTN: SLCBR-DD-T
Aberdeen Proving Ground, MD 21005-5066
OFFICIAL BUSINESS

NO POSTAGE
NECESSARY
IF MAILED
IN THE
UNITED STATES

BUSINESS REPLY MAIL
FIRST CLASS PERMIT No 0001, APG, MD

POSTAGE WILL BE PAID BY ADDRESSEE

Director
U.S. Army Ballistic Research Laboratory
ATTN: SLCBR-DD-T
Aberdeen Proving Ground, MD 21005-9989

---FOLD HERE---